Adv. Space Res. Vol. 8, No. 5–6, pp (5)149–(5)213,1988
Printed in Great Britain. All rights reserved.

0273–1177/88 $0.00 + .50
Copyright © 1989 COSPAR

CHAPTER 5

OPTICAL MEASUREMENTS OF WINDS AND KINETIC TEMPERATURES IN THE UPPER ATMOSPHERE

G. Hernandez* and T. L. Killeen**

**Graduate Program in Geophysics AK-50, University of Washington, Seattle, WA 98195, U.S.A.*
***Space Physics Research Laboratory, Department of Atmospheric and Oceanic Science, The University of Michigan, Ann Arbor, MI 48109, U.S.A.*

INTRODUCTION

In the years since 1972, when the second COSPAR International Reference Atmosphere [1] was published, the contribution of direct optical observations of atmospheric parameters to the quantitative study of the upper atmosphere has become increasingly important. In addition to the more conventional photometric observations of atmospheric emissions, the development of instruments of high spectral resolving power, capable of determining gas-kinetic properties of the atmosphere, has provided an important complement to other techniques involving in-situ spacecraft sensors and incoherent scatter radars. A key factor has been the ability to monitor directly the dynamical and thermodynamical structure of the neutral species in the upper atmosphere. Optical measurements of neutral winds and temperatures from various ground-based and space-borne platforms have guided, and continue to guide, the theoretical modelling effort by providing quantitative constraints to the model parameterizations of the thermospheric energy and momentum budgets as well as direct tests for model predictions.

In this contribution, the historical development of the optical probing of the structure of the upper atmosphere is reviewed. The scientific progress made using observations from ground-based and spaceborne optical sensors, together with thermospheric theory, is also discussed. The significance of the optical technique to our current understanding of the upper atmosphere is reviewed in the context of the new COSPAR International Reference Atmosphere (CIRA-1986). Areas where questions still remain are underscored and the directions for future research are discussed.

HISTORICAL DEVELOPMENT OF OPTICAL REMOTE SENSING

The history of optical measurements of the dynamical and thermodynamical properties of the upper atmosphere can be traced to 1923 when Babcock [2,3] attempted to determine the Doppler width of the naturally-occurring [OI] (^1D - ^1S) radiation from the night sky with a Fabry-Perot spectrometer. Babcock's experiment was the inverse of one carried out in the laboratory 11 years earlier by Buisson and Fabry [4] that had been designed to test the kinetic theory of gases by measuring Doppler widths as a function of temperature. With the technology available to him, Babcock was able to infer only an upper limit to the temperature at the height of the emission, now known to be near 96 km, in the lower thermosphere [5].

During the 35 years or so following Babcock's measurement, other observations were attempted [6-10] using instruments with photographic plates as detectors, but only limited quantitative information on the upper atmosphere was derived [11-19]. Although the most obvious drawback to these measurements was the low quantum efficiency and non-linear behaviour of photographic emulsions, the Fabry-Perot silver mirror coatings employed were also significantly inferior to the multilayer dielectric coatings used today. Nevertheless, these measurements clearly illustrated the potential for optical measurements of the upper atmosphere.

The Fabry-Perot spectrometer came to be considered the instrument of choice for low-light-level, ground-based sensing of the upper atmosphere after Jacquinot and Dufour [20] pointed to its radial symmetry and, later, Jacquinot [21] proved that, for a given spectral resolution, it has the highest luminosity of those spectroscopic devices that depend on the interference of light for their operation and directly yield a spectrum as the final output. The theoretical arguments in favour of the Fabry-Perot spectrometer were reinforced by the demonstration of the feasibility of its use with sensitive photoelectric detectors.

Although the use of the photoelectric Fabry-Perot grew slowly at first [22-39], its ability to obtain quantitative information on upper atmospheric parameters soon led to a veritable flood of new measurements, particularly after Armstrong [40,41] applied the method of Fabry and Buisson [42] and Buisson et al. [43] to determine winds in the upper atmosphere, through observation of the Doppler shifts of emitting species. Following Armstrong's pioneering work, the use of Fabry-Perot spectrometers to determine temperatures and winds in the upper atmosphere became well-established, in part due to the simple and elegant physical principles upon which both the experimental technique and data analysis method are based; principles which require no a-priori assumptions to be made.

EXPERIMENTAL TECHNIQUE

At this point, it is useful to digress into a brief description of the Fabry-Perot technique and the nature of the upper atmospheric observable quantities obtained using this method. The natural emissions of the upper atmosphere are normally associated with forbidden electronic transitions of neutral and ionized species [44]. Because of the long lifetime of the upper states associated with these transitions, the excited species tend to reach statistical equilibrium with the surrounding media before radiation [44]. Therefore, the Doppler profile of the emitted radiation reflects not only the kinetic temperature of the region where the emission occurs (as a Doppler width), but also the bulk motion or wind in that region (as a Doppler shift).

Because Doppler effects associated with typical wind and temperature magnitudes in the upper atmosphere are very small, a spectroscopic device of very high spectral resolution is necessary for their determination. For example, to measure upper atmospheric winds with the so-called green line emission at 17924K (557.7 nm, 1K = 1 cm^{-1}) it is necessary to use an instrument capable of providing a spectral resolving power of greater than 470,000. Since the emissions from the upper atmosphere are also intrinsically very weak, the Doppler measurements are normally made at night to reduce contamination from the intense radiation due to Rayleigh-scattered light from the atmosphere illuminated by the Sun. Therefore, to operate at night, the instrument used must have a large luminosity, i.e., the ability to gather light, in addition to the high spectral resolution referred to above. There exist two optical devices satisfying these stringent requirements, namely the Fabry-Perot and Michelson spectrometers.

Because of fundamental and practical considerations, which are not discussed here, the Fabry-Perot has been the device more commonly used. For both instruments, however, the technique involves the coherent interference of light beams delayed with respect to one another (i.e. with given optical path differences). The properties of these instruments are described in detail elsewhere [45-49], and it suffices to say that the basic principle of both is to transform wavelength into an angular displacement, while adding an effect (line-profile broadening due to an instrumental transfer function) of their own.

Despite the high-luminosity of these devices, the actual determination of atmospheric parameters, of course, requires a finite integration time (usually of the order of minutes) to obtain a meaningful uncertainty or statistical precision. This time is dependent on both the emission rate of the species being measured and the luminosity of the instrument employed. Since the instrumental effects can be removed from the signal [46], the experimenter is able to test the degree of equilibrium reached by the excited species before radiation and, thus, determine whether or not a kinetic temperature can be derived from the measurement. This assumption of equilibrium is not required for wind determinations, since a Doppler shift of the centre of gravity of the line profile defines a motion.

It must be emphasized here that no other assumptions are required to derive physically meaningful quantities, since all the necessary information is already available in the measurement itself. This is in contrast with other methods to obtain temperatures and winds, wherein assumptions about neutral and charged species concentrations or the existence of atmospheric diffusive equilibrium must be made. The self-sufficiency of the spectroscopic measurement has the drawback that very little else is normally learned about the atmosphere surrounding the species other than its kinetic temperature and bulk motion.

The experimental technique used in ground-based measurements of Doppler widths and shifts makes use of the layered properties of the night sky radiations. As has been shown [5,50-64], the stronger emissions of the night sky appear as layers of finite thickness at discrete heights. The heights of the emissions are fixed by the chemical reactions giving rise to the radiating species, while the thicknesses of the layers are dictated not only by the production mechanism, but by the radiative lifetime of the species and by the radiation-less losses (quenching) of the emitting particles as well. For the purposes of the present discussion, it can be stated that the typical layer thickness for the [OI] (^1D - ^1S) emission is about 2/3 of the local neutral atmospheric scale height. Thus, the emission-rate-averaged radiation observed contains information representative of the

atmosphere at the mean height of emission.

The ground-based experimental technique is illustrated schematically in Figure 1. If the bulk motion (or wind) at the height of emission is directed parallel to the emission layer, line profile observations of the layer at a low sky elevation angle from the station will determine the Doppler shift corresponding to the line-of-sight motion, which is a sizeable fraction (0.85 to 0.95) of the horizontal motion, while observations directed at the zenith will provide a measure of the motion perpendicular to the flow. This latter measurement, with suitable precautions to remove or average data from periods when the vertical wind may not be negligible, can then become the zero reference from which the other (horizontal) motions are defined.

An example of Doppler measurements of this kind is given in Figure 2, where the solid curve spectrum is the zenith measurement. In practice, the idealized situation of mass flow parallel to the layer cannot be assumed and the reference (zero) wind is normally obtained by taking an average of many long term zenith measurements.

Unless specifically mentioned otherwise, the convention used throughout this text for the wind motions is the meteorological convention, that is, poleward and eastward winds are denoted as positive.

As would be expected, Fabry-Perot devices have been installed in satellite platforms to determine global dynamics on a relatively short time scale [65,66], to complement the long-term single station ground-based measurements. In the following sections, we first review the progress made using the ground-based optical observations at high, mid- and low-latitudes, ordering the work into upper thermospheric, lower thermospheric and mesospheric regions, employing the usual definitions for these regions [67]. We then describe the progress made using measurements from satellites.

GROUND-BASED OPTICAL MEASUREMENTS OF WINDS AND TEMPERATURES

UPPER THERMOSPHERE

Although the ground-based measurements of Doppler shifts and widths from the upper atmosphere provide a picture of the dynamical and thermodynamical behaviour of a given (local) region of the atmosphere, their value is considerably enhanced when they are interpreted in conjunction with a global circulation model. The interpretation of the observed phenomena, in terms of basic physical processes, within the constraints imposed by both the measurements and the model, makes it possible to reach an improved understanding of the processes and forces that drive and control the upper atmosphere. This interaction between theory and experiment has been particularly successful for studies of the region of the atmosphere above 200 km height, the upper thermosphere, where the emission of radiation by atomic oxygen at 15867 K (630.0 nm) is an excellent tracer of the ambient dynamic and thermodynamic properties. The emission layer of this oxygen radiation normally occurs at a height of about 250 km, where the atmospheric temperature is approaching asymptotically the exospheric temperature [68]. Therefore, the optically-determined temperatures are expected to be slightly smaller than the exospheric temperature.

Experimentally, it has been found [69] that the exospheric temperature (represented by the electron temperature at 400 km) is about 30 K higher than the optically measured temperatures. This measurement was made in the equatorial region during solar maximum. For the other reported determinations [70, 71], the temperature measured with the radar and the optical measurements was found to be, within the uncertainty of the measurements, the same.

Previous to the determination of Doppler shifts reported by Armstrong [41], the measurements from this region were Doppler widths from which kinetic temperatures could be deduced. Some of these early measurements, made with wide-band optical interference filters and at low emission rates, are suspect because of contamination by a nearby OH molecule emission line [72]. In general, measurements taken after 1973 have this contamination problem resolved, and the reported results can be taken on face value as good representations of the thermospheric temperature at the mean height of emission. At about this time, comprehensive ground-based optical studies of the thermosphere at sites ranging from the auroral zone [73] to the equatorial zone [69,71] were initiated.

HIGH-LATITUDES

The first reported measurements of auroral zone thermospheric temperatures using a Fabry-Perot spectrometer were made (photographically) in the 1930's [7] and in the 1950's [11,12,16]. The modern era for these measurements began in the early 1960's with the investigations lead by Shepherd and Vassy [28-30]. In 1972, a Fabry-Perot spectrometer

was used to determine the thermospheric neutral motions in the auroral zone. These measurements were compared with simultaneously measured ion drifts, obtained with the Chatanika incoherent backscatter radar [73], see Figure 3. This comparison showed that the neutral wind in the evening sector flowed in a generally sunward direction, in correspondence with the direction of ion convection, but opposite to that which would be expected from a consideration of solar heating alone. Further analysis of the 1972-73 data set [74] was presented, together with a modelling study of the auroral momentum equation, to suggest that ion drag was playing an important role in establishing the sunward neutral wind. This work was in accord with independent experimental results using rocket chemical release vapour trail analysis [75-77].

A more recent paper [78] has compared the optical meridional wind measurements made in Alaska during 1972 with determinations of the same parameter made using the Chatanika incoherent scatter radar. Reasonable agreement was found between the two (optical and radar) techniques, both for averaged wind patterns and for simultaneously observed winds from individual nights; this is illustrated in Figure 4. The experimental results from this study were also compared with the predictions of the NCAR-TGCM; the comparison indicated reasonable agreement and was suggestive of a possible heat source poleward of Chatanika.

Since the late 1970s, additional high-latitude Fabry-Perot observatories have been commissioned and have been operated at Fairbanks, Calgary, Kiruna, Svalbard, Sondre Stromfjord, Thule, Ny Alesund, Kilpisjarvi, and Mawson and Halley Bay in the Southern Hemisphere. The geographic coordinates of these and other ground-based Fabry-Perot observatories are shown in Table I. Most of the results from these stations published to date pertain to the solar maximum conditions of 1980-1983. Ongoing current work, however, will shortly enable an improved characterization of the high-latitude thermosphere for solar minimum conditions. The reported experimental results have often been compared with one or other of the two general circulation models (TGCMs) of the thermosphere, the University College London model, UCL-TGCM [79], and the National Center for Atmospheric Research model, NCAR-TGCM [80]. These comparisons have served to test and refine the ability of the models to simulate the high-latitude neutral circulation. We next present a brief review of the published results from high-latitude ground-based Fabry-Perot observatories.

A Fabry-Perot situated at Svalbard has been used to determine both the neutral and ion thermospheric dynamics during the polar (winter) night [81-85]. The location of this station is of particular interest since it enables the dayside cusp region to be investigated. For example, optical measurements were made of the cusp region ion drift velocity from Svalbard, using the Doppler shift of the OII(^{2}P - ^{2}D) emission [84], and neutral winds in the same region were measured and compared with the results of TGCM predictions [84,86,87]. The capability for measuring ion velocities optically is a relatively new development that opens up the possibility of performing useful studies in ion-neutral momentum coupling. Averaged data from Svalbard was presented [84] to show the existence of characteristic signatures in the upper thermospheric ion drift and neutral wind that are dependent on the sign and orientation of the B_y component of the interplanetary magnetic field (IMF). This is illustrated in Figure 5.

The dependence of the thermospheric neutral wind on the IMF is a consequence of the strong control of the ionospheric convection pattern by the detailed solar-wind/magnetosphere interaction process which, in turn, is governed by the orientation of the IMF and the velocity of the solar wind. This significant result, obtained by optical means, is a reflection, once again, of the importance of ion drag in the very high-latitude thermosphere. The results from Svalbard, related to the IMF-dependence [85] have been confirmed by other ground-based and satellite measurements [88,89], and an attempt has been made to model the B_y signatures with the UCL-TGCM using, as input, asymmetric, IMF-dependent, ion convection geometries [89]. The theoretical work [89] clearly indicated that the IMF-dependent signatures in the neutral circulation pattern could occur as a consequence of corresponding variations in ionospheric convection.

Additional high-latitude data from the Scandinavian sector has been obtained from Kiruna [89-97]. The thermospheric neutral wind determined at this location was compared with the predictions of the UCL-TGCM for sixteen nights of data taken in November, 1981 [96]. The behaviour of the winds showed a poleward daytime direction, evolving into an equatorward wind between 1600 UT and 0300 UT, with the times of the changes between poleward and equatorward winds being influenced by the nature and intensity of geomagnetic activity on any given night.

A detailed experimental and theoretical investigation of vertical winds at Svalbard and Kiruna was also undertaken [93,94], using the UCL-TGCM. Strong vertical winds with typical velocities of 30-50m/s were reported, shown in Figure 6, with large variability overlaying a basic diurnal variation. Vertical winds of similar magnitudes have also been reported in the Southern Hemisphere auroral region [98]. Results from the Kiruna station

have also been combined with Svalbard measurements [99] and with results from the Dynamics Explorer satellite [89,95,97], to generate more detailed, multi-station descriptions of the high-latitude circulation for comparison with the predictions of the UCL-TGCM.

Recent results have been presented from the Fabry-Perot spectrometer located at Thule at an invariant latitude of 86° N [100]. Neutral wind measurements from this location can be made on a 24-hour basis during the long polar night, and are valuable since they refer to the approximate centre of the geomagnetic polar cap and are, therefore, not as subject to large variations induced by small boundary motions in the ionospheric convection or auroral precipitation patterns. These new results, from the current solar minimum period, indicate a less strong anti-sunward flow within the polar-cap than reported from satellite measurements at solar maximum, with typical wind speeds of $\approx$ 300 m/sec. Comparisons between the Thule results from the winter of 1985-86 and the NCAR-TGCM predictions at 250 km altitude, for solar minimum, show good general agreement, with the polar cap flow rotating in solar local time to maintain its approximately anti-sunward orientation, as illustrated in Figure 7.

Sub-auroral nighttime wind measurements from Calgary have been presented [101] which show strong magnetospheric convection-driven winds, but with considerable variability probably due to the influence of particle precipitation and the expansion and contraction of the high-latitude convection pattern. Optical measurements from Sondre Stromfjord [102] have also been shown to illustrate the nighttime thermospheric neutral wind near the poleward boundary of the auroral zone. The wind signatures at Sondrestrom often indicated a relatively abrupt lessening in the equatorward neutral wind in the early morning hours, shown in Figure 8. This lessening was ascribed to the reduction in the ion drag force associated with the separatrix between the twin cells of the polar ionospheric convection pattern.

New results from Alaska, during and just after the last solar activity maximum, have been recently reported [103-105]. Averages of 44 nights of observations [103] have been collated and studied, as well as data from individual nights [104]. The results have been compared with predictions of the NCAR-TGCM. Systematic variations in the wind signatures were related to the expansion and contraction of the auroral oval as a function of geomagnetic activity. Local meridional accelerations in the neutral wind, evident by the differing line-of-sight wind values recorded to the north and to the south of the station (Fairbanks, AK), were not predicted by the NCAR-TGCM and this was ascribed to the limited spatial resolution afforded by the 5 degree model grid.

Results from Alaska were also used to investigate the effects of the varying altitude of emission for the determination of thermospheric temperatures in the aurora [105].

MID-LATITUDES

The present section, on the optical contributions to the study of the mid-latitude thermosphere, begins near 1970. Up to this time, reports on the dynamics and thermodynamics of this region included little more than a few isolated optical measurements [106-108], the description of complete studies on some unusual events [109-111], or reviews of the subject [112]. With a few exceptions [113-116], the information reported after this time includes simultaneous measurements of Doppler widths and shifts, which will be discussed together.

In 1976, a 16-month experimental study of the temperature and winds determined from the 15867K emission line at midlatitude was presented [117,118] and compared with a (zonally averaged) model of the thermosphere.

This model used, as input, values from the early MSIS semi-empirical model of neutral composition and temperature, derived from spacecraft and radar measurements [119]. The temperature and composition gradients inherent in this semi-empirical model provided the pressure gradient forces on the neutral gas, while the ion drag forces were obtained using a second semi-empirical model [120] for electron density. Since such a general circulation model only portrays the large-scale details of the global circulation, comparison between the measurements and the model was made only for the general behaviour of the winds, evident in the data.

During magnetically quiet times, defined as $A_p < 35$, the general trends [117] found in the measurements resemble those predicted by the model; that is, the calculated variations of the zonal wind are approximately related to the local time derivative of the neutral temperature, however altered by ion drag and Coriolis forces. For these quiet conditions, characteristic patterns for summer, equinox and winter are maintained for the atmosphere above the observing site (Fritz Peak Observatory, 39.9°N, 105.5°W). The observed patterns and the corresponding model calculations are shown in Figures 9 and 10. Figure 9 illustrates the zonal wind dependence mentioned earlier, in particular for the equinox example, while Figure 10 shows the temperature changes responsible for the observed zonal

winds. The agreement between the model and observations is rather good for the motions, while there appears to exist a temperature difference between measurements and the model which becomes more noticeable for the equinox and summer patterns. Note that this difference occurs between the semi-empirical model for temperature and composition [119] used in the global circulation model and not with the global circulation model proper. The general conclusion for this quiet time study was that, for low magnetic activity times, the global thermospheric circulation is controlled by insolation and could be quantitatively predicted. However, measurements made during magnetically disturbed times [118], such as the example given in Figure 11, show much larger winds than would be predicted by a simple insolation model and, in particular, for the zonal winds where the observed direction of flow is opposite to that required by the local temperature component of the pressure force, indicating the presence of another force influencing the gas motion.

Although the measurements and the model could be forced into a qualitative agreement for the general trend of larger winds, this could only be accomplished when the model's semi-empirical composition and temperature dependence on magnetic activity was pushed beyond its recommended value. Nevertheless, this experiment confirmed the need for a high-latitude energy source to explain some of the observed behaviour. In addition, some of the details of the measurements showed a strong suggestion of ion drag effects, similar to those observed in the auroral zone [73-75], but there existed no supporting data to test this contention. This is illustrated in Figure 12.

Further measurements for solar minimum, during geomagnetically quiet conditions, were examined in detail [121]. The monthly variations of the diurnal circulation pattern, previously observed and discussed [117], were compared with those generated by a comprehensive global circulation model [122], shown in Figures 13 and 14. Because of the rather good agreement between the nighttime observations and the model, it was then assumed that the model calculations were representative of the winds throughout the day and, thus, average diurnal values for the winds were deduced. These zonal mean values are given in Table II, where it can be seen that the average meridional wind flows equatorwards during the summer, at about 40 m/s, and poleward, at 25-35 m/s during the winter. The mean zonal wind is found to flow eastward in the winter months and westward in the summer months. The transition between the oppositely-directed flows is rather sharp and occurs near or at the equinoxes, thus separating the global circulation into winter and summer conditions. The observed and calculated temperatures show a difference of about 50-75 K in the winter and 100-150 K in the summer, with the measurements always being larger than the model deductions, as illustrated in Figures 13 and 14. This disparity between the (optical) observational and model temperatures is not yet clear, and it appears in other reported observations [123,124].

The zonal mean wind values obtained in this study [121], given in Table II, were used [122] to model the global mean circulation and latitudinal variation of temperature in the thermosphere. In the latter study, it was shown to be necessary to include a high-latitude heat source associated with auroral processes, in addition to the solar ultraviolet radiation, in order to obtain reasonable agreement between the observed zonal mean values and the theoretical calculations. Thus, ground-based observations are not only useful in the determination of the dynamic structure of the thermosphere, but can also be used to infer the overall magnitude and variation of the high-latitude heat source necessary to explain the physical processes causing the observed motions. The results obtained in the experimental study [121] have been confirmed by further measurements obtained at midlatitude in both the Southern [124,125] and Northern Hemisphere [126].

At about this time (1977), measurements were reported [127] which validated the longitudinal, or zonal, averaging assumption made in the two-dimensional thermospheric circulation models. The experimental results, shown in Figure 15, simply state that the pressure forces giving rise to the observed wind fields are governed chiefly by a local time phenomenon, namely the Earth's rotation and the subsequent differential heating of the atmosphere by solar radiation. Although this behaviour had been expected from prior satellite drag measurements, these were the first direct measurements of the actual motions.

The dramatic response of the upper thermosphere to geomagnetic storms was investigated [128] in terms of impulsive heating at high latitudes. By adjusting the magnitude and duration of this high latitude heat source, it was possible to deduce its size and properties by requiring good agreement between the observed and calculated response. This has also been done for ionospheric disturbances [129]. A typical case of the storms investigated is shown in Figure 16, where the large amplitude variations in the (meridional) wind are noticeable. The model calculations are given in Figure 17, where the expected wave nature of the disturbance is apparent. The results showed that approximately 7×10^{22} ergs need to be deposited in the high latitude atmosphere to generate a wave with a peak amplitude of approximately 300 m/s in the meridional direction. This admittedly crude estimate is, nevertheless, in good agreement for various

peak wind magnitude storm measurements, even though the source's shape and duration of the impulse are arbitrary [130]. A physical mechanism that would satisfy the requirements of this high latitude source appeared to be the rate of change of D_{st} [131], since the energy input derived from this rate of change, using the reported [132] expression for the ionospheric power dissipation associated with the storm, was consistent with the model calculations.

An example of the D_{st} correlation with the observations is shown in Figure 18, while Figure 19 illustrates this correlation for a number of storms, plotted as peak wind as a function of the peak rate of change of D_{st}.

The relationship between the rate of change of D_{st} and the peak meridional wind during a geomagnetic storm did not hold for all cases, as illustrated in Figure 20; however, the measured peak winds have a very strong correlation with the averaged auroral electrojet (AE) index to the second power, $(AE)^2$, [133], which is representative of Joule heating of the high-latitude thermosphere.

This correlation also applies to the measured temperature increase, but as the summation of the second power of AE, $\sum (AE)^2$. This is shown in Figure 21 for the storm of May 9, 1978. The relationship with AE was found to hold for all storms studied (22) for which there existed AE index values, including those storm-time measurements by other authors [110,134], and this is illustrated in Figures 22 and 23. The data presented in the figures show a nearly linear relationship, with correlation coefficients of 0.815 and 0.938 for Figures 22 and 23 respectively. The correlation coefficients just mentioned have been found to be significant to better than the 1% level for all cases. The apparent lower correlation coefficient found for the meridional wind may be caused by the uncertainty in extracting a peak meridional wind from the measurements where other effects, such as tidal, are present. The interpretation given to the findings [133] is that, since $(AE)^2$ is representative of the high-latitude Joule heating, the winds over the observing site respond directly to the heating input during the storm or substorm period, while the temperature increase is a measure of the total energy input, rather than the instantaneous input as is the case for the motions. Further, Akasofu [135] has presented a relationship between AE and the interplanetary quantity:

$$\epsilon\ (t) = V\ B\ \ l_o^2\ \sin^4\ (\ \theta\ /\ 2\ ).$$

In this expression, V is the solar wind speed, B is the magnitude of the IMF, l_o is a constant and θ is the polar angle of the IMF. The relationship between ϵ (t) and AE [135] indicates that a 1000 nT index corresponds to an energy input into the magnetosphere of about 10^{19} ergs/sec. The dynamic modelling of the storm of April 1, 1976, shown in Figure 16, requires [128] an energy input of near 10^{19} ergs/s to produce the 300 m/s meridional wind observed. According to Figure 22, a 300 m/s peak meridional wind is associated with a roughly 1000 nT AE index value, which is quite close to the 1050 nT experimentally determined for that particular storm. Although more study is required in this area [133], the correlations found in that investigation are indicative of the quantitative response of the upper atmosphere motions and temperature to the high-latitude energy input. Further studies should lead to a better understanding of not only the deposition of the energy in the atmosphere, but its eventual re-distribution as well. The general dependence of the winds on magnetic activity has been independently corroborated by optical measurements in the southern hemisphere [136].

The majority of the investigations thus far discussed have been made near solar minimum conditions, given by the 2.8 GHz solar radio noise index F with values less than 10^6 Jansky (1 J = 10^{-26} W m^{-2} Hz^{-1}). By November 10, 1977, solar activity had markedly increased (F value of 3.77 10^6 J, or a fourfold increase) and the atmosphere had noticeably responded to this change in solar activity. The observed kinetic temperature of the upper thermosphere [126,137,138] nearly doubled in value. The changes, both in solar activity and in upper thermosphere kinetic temperature for this period, are shown in Figure 24. This homogeneous data set was compared with the semi-empirical models [119,139-142], and the results are illustrated for a selection of these models in Figure 25.

Since the correlation coefficient for a linear fit of the experimental data with the models was no larger than 0.86 (OGO-6), i.e., the models could account for only 74% of the observed variations, a statistical test of the experimental data was performed to find whether or not the determined correlation was caused by inherent uncertainties in the data itself. This statistical test [138] showed that it should be possible to account for 92% of the variations observed in the data. Accordingly, the experimental data were examined for their dependence upon geophysical parameters known, from previous modelling investigations by others, to strongly affect the temperature.

The strongest dependence of the temperature is on the solar flux, and this is illustrated in Figure 26, for the data for the months of November and all the geomagnetically quiet

data as well. In this figure, the solar flux is represented by the 2.8 GHz radio flux, since the solar radio noise at 2.8 GHz has been found to be roughly proportional to the solar UV radiation, at least in the Schumann-Runge continuum area [143,144]. As indicated in the figure, the best fit was found for a non-linear expression of the form:

$$T_{exp} = a \; F_{-1}{}^{b},$$

where (a) and (b) are constants and F_{-1} denotes the solar flux for the day previous to the temperature observations. For both the selected data and the quiet data of Figure 26 the value of (b) is stable, within the uncertainties of fit. Note that such a power law has been found to be applicable for the modelling of satellite drag density measurements [141].

Although from earlier work [133] described previously, a rather simple relationship between observed temperature changes and geomagnetic activity (expressed as the AE index) had been found, there were no AE index values available, except for a few days of the experimental temperature measurements. A more generally-available index of magnetic activity, A_p, was used to describe the geomagnetic activity effects on the data [138]. The residuals of the temperature, after removal of the solar and geomagnetic activity effects, are illustrated in Figure 27.

The right panel is a superposed-epoch analysis of the residuals shown in the left panel. Harmonic analysis of these residuals shows strong annual and semi-annual variations, with the phase of the former indistinguishable from the solar declination angle during the year. The resultant expression for the fit of the temperature data is:

$$T_{exp} = 195\ (+/-\ 3)\ F_{-1}{}^{0.34\ (+/-\ 0.005)} + 3.3\ (+/-\ 0.15)\ A_p + 67(+/-\ 4)\ \delta_N$$

$$+ 30\ (+/-\ 4)\ \cos\ (\ 4\ \pi\ \ [d - 110\ (+/-\ 3)]\ /365.25)$$

$$\rho = 0.91\ .$$

In the above expression, δ_N is the normalized solar declination angle, i.e., $\delta_N = \delta_\Theta/23.44$, and d is the day number beginning with January 1. (ρ is correlation coefficient)

The correlation coefficient of the expression indicates that 83% of the observed variations can be accounted for with the 4-term expression, against 72% with any of the models then tested. It is interesting to note that the above expression also gives a better fit than the functional relations used for the empirical models, but fits for the experimental data. The fit of the experimental data and the expression above is shown in Figure 28.

Although the temperature variations associated with the solar flux and geomagnetic activity, as well as an annual variation were expected, a semi-annual variation was a surprise. A semi-annual variation is usually ascribed to density variations in the semi-empirical models [145-147]. Other measurements, from both the northern [126] and southern [124] hemisphere, show general agreement with the 7-year data used in the deductions, in particular the form of the solar activity expression [124]. Also, for the sake of completeness, Figure 29 illustrates the observed upper thermosphere temperature for over one solar cycle. In this figure, some of the features discussed earlier can be easily discerned.

The behaviour of the atmospheric motions was also noticed to vary as solar activity changed [148]. Since the wind data requires a vectorial representation, the data were reduced to manageable proportions by the following method. The quiet time winds, i.e., $A_p < 20$, were averaged into monthly groups as a function of local time and direction of observation (N, E, S, and W). Then, the average winds in each direction were fitted to lowest order harmonic analysis. An example of the data and their fit is given in Figure 30, for the month of July 1978. The fitted winds were then sampled at every one-half hour interval and plotted as (smooth) contours. These contours are shown for solar minimum conditions in Figure 31 and solar maximum in Figure 32. The similarity in the zonal winds for both the east and west direction contours, as well as the north and south winds for solar minimum conditions, made it possible to further coalesce the data into zonal and meridional components.

The final results are then a simple zonal and meridional wind set for solar minimum and two sets of wind components for solar maximum conditions, one for observations north of the station and one for observations south of it.

The resultant winds are better displayed in a vector fashion, shown in Figures 33 and 34, where South is at the bottom of the graphs. The solar minimum wind pattern, of Figure 33,

shows that the winter winds are eastward except in the early morning. The transition from eastward to westward is fairly sharp and occurs near the equinox (both spring and autumn), such that the winter circulation is characterized by an eastward flow and the summer circulation by a westward flow. The meridional component is southwards, except in the early evening in winter, and its magnitude maximizes in the summer. The patterns of the thermospheric motion during solar maximum of Figure 34, show an eastward to westward transition occurring earlier as summer approaches, while the meridional wind shows a strong southward behaviour, except in the early evening. Solar maximum wind patterns are more ordered than the solar minimum patterns, as a cursory inspection of Figures 33 and 34 will indicate.

The NCAR-TGCM was used to calculate the seasonal variation of the wind and this was compared with the observations [148]. In general, the model calculations show a wind pattern similar to that observed, but with a maximum wind amplitude at summer solstice for both minimum and maximum solar activity, illustrated in Figure 35. The observations at solar minimum in Figure 31 show maximum wind amplitude during August, just before the fall equinox. Apart from this difference, not yet resolved, the modelled patterns match the observed values reasonably well. With the help of the model calculations, the thermospheric motions observed during solar minimum and maximum have been interpreted [148] in terms of the forces that drive the global thermospheric circulation. For solar minimum, the circulation is primarily driven by global pressure gradients established by solar heating and a high-latitude heat and momentum source, with the latter at a large distance from the observing site.

This large distance between the observing site and the high-latitude source gives no sharp latitudinal gradients of high latitude forcing in the vicinity of the observatory. During solar maximum, the expanded and more intense magnetospheric convection is closer to the observing site. The winds to the north of the station are, therefore, under the influence of this forcing, whereas the winds to the south are not. Also, the electron densities during solar maximum are larger both in the ionosphere and the model [120], and this should give rise to a greater magnetospheric convection ion drag momentum source than for solar minimum. As expected, large day-to-day variations have been found in the motions during magnetically quiet days [149], and appear to be local effects.

The behaviour of the midlatitude thermosphere during magnetic storms also changed considerably as solar activity increased. During solar minimum, the thermospheric response to magnetic storms exhibits an impulsive character in the meridional direction, yet the motions observed both north and south of the station are quite similar, as illustrated in Figures 11 and 16. As solar activity increased, the effects of the storm in the meridional wind direction become direction-sensitive, as shown in Figure 20. Finally, at near solar maximum, the meridional motions are decoupled and move in different directions, as illustrated in Figure 36 [150]. As shown in the last figure, the observing site appears to be near a boundary between opposite flowing regimes. Because of the unusual character of the observations, a careful check was made on the measurements to assess the effects of atmospheric aerosol scattering [151], and the results indicated that such effects were of minimal concern [150]. A scenario, using the NCAR-TGCM, was constructed to attempt to understand the physical processes behind the observations.

Beside the Fabry-Perot measurements, shown in Figure 36, a DMSP photograph was also available. This showed that there was strong auroral activity at the Canadian-US border, indicating an expansion of the magnetospheric convection pattern during the course of the storm. This would, in turn, provide the momentum source to drag the neutral atmosphere in the direction of ion drift. As had been shown earlier [152], the circulation patterns associated with magnetospheric convection show abrupt boundaries, such that, in certain regions, the neutral winds follow the convection pattern driven ion flow, while equatorwards of the boundary the winds have the typical mid-latitude circulation pattern, which is normally from the southwest during the evening hours [80]. As can be seen in Figure 36, the observed winds qualitatively agree in their behaviour with the above picture, if the north and east directions of observation are considered to be under the influence of magnetospheric convection. This behaviour is schematically shown in Figure 37.

Quantitatively, the midlatitude-like behaviour of the south and west portions of the figure is considerably enhanced from the typical quiet time midlatitude circulation. Three possible mechanisms were invoked to attempt to explain this enhanced circulation [150] on the equatorward side of the observing site. They were:

a) hemispheric differences in the thermosphere energy input rate;
b) equatorial heating by neutral or particle precipitation [153] and
c) an enhanced midnight equatorial temperature bulge.

In the absence of corroborating evidence, any (or a combination) of the above mechanisms would satisfy the observed circulation. Also, it is quite possible that, during such

storm events, the emission height of the species used to determine the Doppler shifts is quite different in the separate observing directions [118,150], and the measurements indicate somewhat different atmospheric responses at different heights. In spite of the uncertainties in the interpretation, the observed behaviour of the thermosphere during solar maximum conditions resembles more the patterns observed in the polar regions, described in the earlier section.

A further study of solar maximum storms was made [154] for the storm of March 2, 1983. The thermospheric response to this storm, shown in Figure 38, showed thermospheric motions usually observed in the auroral zone, namely a southward surge near midnight and strong westward motion in the direction of magnetospheric convection. For comparison, Figure 39 shows the geomagnetically quiet circulation observed near the time of the storm.

Model simulations for this quiet period were made with the NCAR-TGCM, and the results are also shown in Figure 39. To simulate the storm time behaviour, the model's convection pattern was assumed to expand 10^{o} equatorward from its geomagnetic quiet position, while the cross-tail potential of the magnetospheric convection model was increased to 60 kV from its 30 kV quiet time value. As described earlier, the ion drag associated with magnetospheric convection dominates the neutral winds at high latitudes, although the neutral's motion lags that of the ions by about 1 to 2 hours, an effect also observed in the simulation. The results of the above described simulation are shown as the solid and dashed lines in Figure 38. A more detailed picture of the model's circulation is illustrated in Figure 40 for the 0300 UT and 0700 UT periods. In the latter time simulation, the 'midnight surge' is seen to affect the region near Fritz Peak, as was found in the observations. A detailed discussion of the high-latitude circulation has been given earlier and need not be repeated here. This extreme example, of a geomagnetic storm during solar maximum, has illustrated the changes occurring in the global circulation as solar and geomagnetic activity change, with the ensuing changes in the position and degree of deposition of solar derived energy and, thus, showing the close coupling of the terrestrial atmosphere and solar activity.

Although the optical measurements of the upper thermosphere discussed thus far have been made at night, there are a few reports of ground-based daytime thermospheric temperatures [36,155-156] and one of the winds [156]. These preliminary experiments, which have used the OI 15867K dayglow emission as a tracer, show the feasibility of 24-hour ground-based coverage of the dynamics and thermodynamics of the upper thermosphere by optical means.

LOW-LATITUDES

Whereas most of the ground-based observations and theoretical studies of the dynamics of the upper thermosphere have concentrated on the mid- and high-latitude regime, there have been a significant number of low-latitude and equatorial ground-based studies using optical techniques. Theoretical comparisons with the upper thermosphere mid- and high-latitude wind data sets have generally shown good agreement, and iterative model runs have elucidated characteristics of the high latitude heat and momentum source. The situation at low latitudes, however, is complicated by the presence of the equatorial midnight temperature maximum, which is thought to produce a pressure bulge that modifies the neutral wind circulation.

The TGCMs do not as yet contain a full physical description of the equatorial night-time pressure bulge, a feature which is probably related to the upward propagation of tides generated within the lower atmosphere. It has therefore been impractical to examine many of the phenomena observed at equatorial latitudes with the intensive scrutiny permitted by the theoretical model simulations, as has been the case for the mid- and high-latitude measurements reviewed earlier.

Equatorial thermospheric temperatures, obtained from Doppler width determinations of the oxygen red line, have been compared with incoherent scatter radar measurements of ion and electron temperatures at the Jicamarca Radio Observatory [69] and at Arecibo Observatory [71]. The neutral temperatures from the optical techniques were found to be within a few tens of degrees of the electron and ion temperatures determined by the radar, indicating very close thermal coupling between the charged and neutral constituents of the equatorial thermosphere, and providing confidence in the cross-calibration of the two techniques. In the case of the Jicamarca observations, the simultaneous radar and optical data gave a measure of the altitude profile of thermospheric temperature for solar maximum, in good general agreement with the Jacchia 1971 empirical model [1,157].

Direct measurements made at Kwajalein [158,159] (9^{o} N) and at Natal in Brazil [160] (5.9^{o} S) have also been reported. The comparison of the Kwajalein results with NCAR-TGCM model predictions [158] has indicated that the equatorial F-region winds are strongly influenced by variations in the ion drag caused by E x B drifts in the equatorial ionosphere, upward propagating tides from the lower atmosphere and high-latitude magnetospheric convection.

The Fabry-Perot spectrometer at the Arecibo optical facility has provided seasonal upper thermosphere neutral wind averages [161]. These measurements have been investigated in the light of the detailed measurements of the local ionospheric morphology as determined by the incoherent scatter radar at Arecibo. The wind measurements have also enabled a detailed study of the F-region electrodynamics [162], including the effects of polarization electric fields originating in the F-region of the conjugate hemisphere.

A relatively new equatorial station at Arequipa, Peru has provided measured emission rates [163], temperatures [123], and winds [164] from the oxygen red line emission in the equatorial upper thermosphere. Airglow depletions of factors as large as 3-4 were noted at Arequipa during periods of equatorward meridional wind [163]. Comparisons with modelling calculations suggested that the depletions resulted from an upward movement of the ionosphere along the inclined magnetic field lines, driven by the prevailing equatorward neutral wind that, in turn, was ascribed to the passage of the midnight pressure bulge. Further measurements of neutral temperature excursions as a function of solar flux and geomagnetic activity [123] indicated that the average temperature over Arequipa was approximately 180 K greater than that predicted by the MSIS-83 model. Also evident were rapid increases in temperature (by several hundred Kelvin) associated with periods of strongly increasing geomagnetic activity such as sudden commencements. These changes were ascribed to possible energetic neutral particle precipitation from the ring current or to the equatorward transport of high-latitude energy and momentum by gravity waves and neutral winds. 62 nights of upper thermosphere neutral wind data have been used [164] to investigate the seasonal variation of the equatorial thermospheric wind. The comparisons made with the NCAR-TGCM for equinoctial and solstice conditions showed good agreement.

LOWER THERMOSPHERE AND MESOSPHERE.

It is ironic that the lower thermosphere has been studied optically the longest of all the regions of the night sky [2], yet it is still the region about which our present knowledge is the poorest. The more intense emission from that region proceeds from the OI (^1D - ^1S) transition at 17924K (557.7 nm), where the excitation is achieved by chemical reactions at equatorial and mid-latitude regions and by a combination of chemical processes and collisional excitation by energetic particles at higher latitudes.

The end result of these excitation processes is that the height of emission of the main chemical process is near 96 km [5,50-58,61-64,165], yet there also exists some production of this species at F-region heights due to the dissociative recombination of O_2^+ [166-168] which is of concern mostly at the equatorial regions [168]. At higher latitudes, the production of this line by collisional excitation is dependent on the energy of the incoming particles and, thus, the height of emission is quite variable and structured. In general, it can be said that ground-based measurements of this emission line from equatorial and midlatitude regions refer to approx 96 km height (with a few exceptions), while high-latitude measurements refer to the combined emissions arising from several height regions.

Just below the height of the OI emission line, there exist other atomic emissions (discussed later) and molecular emissions. These latter emissions occur in the mesosphere, and have primarily been used to determine rotational temperatures, which require very low resolving power for their determination [see 169 for details and references]. In this section the investigations of other than kinetic temperatures will not be considered in any detail.

Returning to the OI emission, the earlier measurements refer to temperature determinations [2,3,11,16,18,22-29,33,38-40,48,165,168, 170-172], while there are fewer reports in the literature on the motions at this region of emission [40,173-177]. In the equatorial and mid-latitude regions, the temperature of the lower thermosphere derived from the Doppler widths of OI is about 200K, with a typical range of 150K to 250K. In the auroral zone, temperatures ranging from 150K to 1140K have been reported [28-30,170]. Most of the determinations mentioned above encompass a few measurements, or a few nights at different places and epochs, except for a report covering nearly one solar cycle at midlatitudes [165].

The daily behaviour of the kinetic temperatures at midlatitudes is quite variable [165], as illustrated in Figure 41. This variability seems to extend over the observable sky, as shown in Figure 42. In order to discuss the long-term variations in the observed temperature, the data were averaged by observing periods (+/- 7 days about new moon) for the 1964-1975 time period [165], illustrated in Figure 43. The measurements presented in the figure show an apparent anti-correlation with solar activity (which maximized late 1968) and this was quantitatively tested as shown in Figure 44.

This low temperature effect in the lower thermosphere has also been observed using artificial sodium clouds at higher latitudes [178]. Further investigations showed a

dependence of the kinetic temperature on the averaged solar flux, and on its daily changes, on magnetic activity as well as annual and semi-annual variations, as shown in Figure 45. This figure shows the step-wise least squares fitting process used to determine the dependencies of the data on the geophysical quantities previously mentioned. The residuals, after the removal of the above dependencies, showed statistically significant power still present with variations with near 5 yr and 2.5 yr periodicities, as indicated in Figure 46. The final fit to the temperature, including these 2.5 yr and 5 yr periodicities is given in Figure 47 for the examples where solar activity is expressed as the 2.8 GHz solar radio noise and sunspot number. The expression for the best fit (using the 2.8 GHz radio noise) is:

$$T_{exp} = 231 \ (+/- 3) - 0.46 \ (+/- 0.03) \ \overline{F_{216}} + 0.16 \ (+/- 0.03) \ F_{-2}$$
$$+ 0.34 \ (+/- 0.05) \ A_{p-4}$$
$$+ 7.1 \ (+/- 0.8) \cos \{ 2\pi [y - 1963.3 \ (+/- 0.07)] / 5 \}$$
$$+ 6.0 \ (+/- 0.7) \cos \{ 2\pi [y - 1965.8 \ (+/- 0.04)] /2.5 \}$$
$$+ 7.3 \ (+/- 0.7) \cos \{ 2\pi [d + 2 \ (+/- 5)]/ 365.25 \}$$
$$+ 2.4 \ (+/- 0.6) \cos \{ 4\pi [d - 9 \ (+/- 30)]/ 365.25 \}$$

In the above expression, y is the date, expressed as year and fraction, and d is the day number beginning with January 1. The other quantities are the 2.8 GHz solar flux averaged over 216 days previous to the day of observation ($\overline{F_{216}}$), the solar flux for two days earlier than the observation (F_{-2}) and the geomagnetic activity parameter four days previous to the measurement (A_{p-4}).

Note that the net effect of the long term averaging over the solar flux effectively provides a delay to the solar activity matching the observed response in the temperature, which minimizes after the peak of solar activity. The other findings, such as the annual and semi-annual variations, were expected [179] and are associated with transport from the equatorial to the polar regions and vice versa [180-181], while the 2.5 yr oscillation can be interpreted in terms of the quasi-biennial oscillation of the atmosphere [179,182] since the temperature maximum coincides with the quasi-biennial oscillation maximum eastward flow at 60 km and 35°N latitude (i.e., the highest and northernmost values reported [179]).

There is no readily available explanation for the 5-year periodicity oscillation. The combination of the annual and semi-annual variations found in that investigation [165] was compared with other published results [179], with the latter weighted by an airglow emission profile [57], arbitrarily shifted in altitude. The results of this comparison are given in Figure 48. To obtain the results shown in this figure, the mean height of the optical measurements was adjusted to show the least error in height variation, and this level is found at a mean (invariant) height of 95.5 km with a standard deviation of 3 km [165], which is in good agreement with satellite determinations of the height of emission [5].

The region of the atmosphere sampled by the OI 17924K line is strongly influenced by perturbations from both above and below it. As has been mentioned above, the more obvious influences are those associated with solar and geomagnetic activity proceeding from above the region, while one of the influences from below the region (stratospheric warmings) has been identified experimentally [172]. As part of the attempt to describe the experimental temperature behaviour, it was found that there existed some measurable departures from the best fit during (northern hemisphere) winter. These departures are associated with the presence of stratospheric warmings [172], as illustrated in Figure 49. The cooling shown in the figure is 9.1K, which is significant to the 95% level and with a confidence interval from 4.0K to 14.2K. As can be seen from the figure, the timing of the optical measurements with respect to the stratospheric warming is quite critical. Stratospheric warmings are caused by the interaction of planetary scale waves with the zonal wind flow at stratospheric heights [e.g., 183,184]. It is normally found that stratospheric warmings are associated with cooling trends at mesospheric altitudes, and far more measurements are necessary to resolve the complex, multi-level, behaviour of the atmosphere during such disturbances.

The winds determined from Doppler shifts [40,173-176] show a strong tidal effect, which varies with season [173]. This is illustrated in Figure 50 for autumn and spring, during solar minimum and geomagnetically quiet conditions. Contour maps of the winds, extracted from figures such as the one previously shown, are illustrated in Figure 51 for the 1971-1972 period. In this figure, the hashed areas indicate westward and northward motions.

These geomagnetically-quiet measurements indicate that the largest wind variations observed during the night have a nearly 12-hour periodicity, attributed to a semi-diurnal tide. Although there may be other influences, such as gravity waves, present in the measurements, the smoothing procedure used in preparing the figure will tend to minimize such a-periodic influences.

Further wind measurements have been reported [175] in a comparison of the motions of the lower thermosphere as measured by optical and meteor radar techniques. Again, the main wind component during solar minimum was found to be associated with semi-diurnal tidal components, in agreement with the earlier report, since both sets of measurements refer to solar minimum conditions. The comparison between the two techniques of wind measurement gave rather good agreement, illustrated in Figure 52, considering the large geographical separation between the two stations. The summary of the comparisons is given in Figure 53, where the 'amplitude' is arbitrarily defined as one-half of the maximum excursion observed in the data for overlapping measurement times and the 'phase' is given as the time of maximum excursion(s) for the convention of positive southward and eastward motions.

As the figure shows, the agreement is reasonably good for the large scale behaviour of the motions, in particular for the zonal wind of late 1974 where the motion was easterly for both stations and which normally is westerly, as found in the 1975 series. The zonal 'phase' difference of about two hours is about the time difference associated with the longitude difference between the two stations, as if both stations were observing at a 'standing wave' phenomenon, or an event of much larger scale than the separation between the two stations.

Observations of motions of the atmosphere, using the OI 17924K emission at a sub-auroral station, have been reported [177]. The behaviour of the observed horizontal motions was very much like those reported for the upper thermosphere at those latitudes, using the 15867K emission line. As described earlier, the 17924K emission at auroral latitudes has a variable height, depending on the energy of the precipitating particles. A significant, but variable contribution to the emission appears to come from the upper thermosphere, which contaminates the lower altitude emissions, and produces the tendency for the Doppler shift to mimic that observed with the oxygen red line.

In this report, no temperature determinations were given, which would have helped to define the height range of the emission, since the atmospheric temperature gradient in that region of the atmosphere is large. Vertical winds, associated with auroral arcs, have also been determined with the 17924K emission [185]. In both instances, it is not clear whether or not such measurements should be included as upper thermospheric, or lower-thermosphere/mesosphere determinations.

As mentioned at the beginning of this section, there are other atomic emissions present near the height of emission of the 17924K oxygen line. Among these other atomic emissions, that proceeding from sodium is the brightest, and has been examined with high-resolution techniques [186- 188]. Temperatures were only measurable during twilight, when the emission is enhanced by the resonant scattering of solar radiation. Later in the evening, the observed sodium line profiles are quite broad and non-thermal, and thus not useful to derive kinetic temperatures. This is illustrated in Figure 54.

Although, in principle, winds could be derived from Doppler shifts, the extremely large line breadth makes it impractical, since the errors of determination are quite large when a small shift of a wide profile is to be measured. Nevertheless, such measurements are capable of providing information on the history of the atom previous to radiation, as is also the case for the 17924K line in the equatorial zone [168].

The use of molecular emissions, naturally occurring in the atmosphere, to directly determine kinetic temperatures and motions has been a recent advance [189,190]. The molecule used for this preliminary measurement was the OH molecule occurring in the mesosphere at near 85 km. Motions resembling the tidal behaviour observed with the 17924K line were obtained, as illustrated in Figure 55. No simultaneous measurements with the higher altitude emissions are available yet. The use of molecular emissions makes it possible to determine the dynamical and thermodynamical behaviour of regions of the atmosphere hitherto not accessible with optical techniques.

SPACEBORNE OPTICAL MEASUREMENTS OF WINDS AND TEMPERATURES

The placement of optical remote sensing devices on spacecraft in order to monitor naturally-occurring atmospheric emissions has continued over many years.

While indirect information on temperatures and winds have been derived from volume emission rate measurements for specific emissions, only two remote-sensing instruments have been flown to date with the capability of making direct measurements of temperatures

and winds, using very high spectral selectivity to determine the detailed Doppler characteristics of the emissions.

The first optical remote sensing device designed to measure the upper atmospheric temperature from a spaceborne platform was a spherical Fabry-Perot spectrometer (FPS) [65] that was flown on the OGO-6 spacecraft. This instrument measured the line profile of the 15867K (630.0 nm) oxygen line in the airglow, at varying altitudes between 200 and 320 km, by performing a limb scan of the horizon from orbit. The analysis of these line profiles yielded exospheric temperatures along the track of the satellite. Observations were obtained from launch on 5 June 1969 to 16 August 1970. This period corresponded to near-solar maximum conditions.

Figure 56 illustrates the viewing geometry from the satellite platform, which is to be compared with the ground-based geometry shown in Figure 1.

The FPS instrument operated flawlessly during the mission and no change in the pre-launch values of the critical instrument parameters occurred during flight. The systematic errors of measurement of temperature (due to imperfect knowledge of instrument parameters) were estimated [65] to be +/- 15 K, while the statistical error of a typical measurement was estimated to be +/- 50 K for dayglow conditions.

The instrument sensitivity was such that measurements of temperature were only obtained for daytime and dusk hours, with some extended local time coverage at high-latitudes due to enhanced auroral emissions. A total of 238,000 individual measurements were recorded during the mission and these results have been used primarily for the generation and improvement of empirical models of the thermospheric temperature structure.

The large variability of the exospheric temperatures in the summer and winter polar regions during the magnetic storm of September 1969, in contrast to the smoother variation observed at lower latitudes, was pointed out in the first report [65]. It was also noted that a rapid transition in polar temperatures from a summer to a winter condition occurred close to the equinox. Figure 57 illustrates this rapid change-over from summer to winter temperatures, with the variation of the difference between the (daily averaged) temperatures in the northern and southern regions at a latitude of +/- 75^{o}, plotted as a function of season. The change-over from positive to negative values occurs at the equinox and is very rapid, with a slope of about 7 degrees per day [191].

A significant discrepancy between the exospheric temperatures, measured optically on OGO-6, and those inferred from incoherent scatter data was also reported [65]. This discrepancy appears to have a maximum in the middle of the day, when the airglow temperatures were about 100 K lower than incoherent scatter temperatures.

The data from OGO-6 were later used to synthesize global, empirical, exospheric temperature maps from the FPS measurements [191], illustrating the seasonal and latitudinal dependencies. Figure 58, taken from this report, illustrates the basic latitudinal structure observed in the dawn-dusk plane at Spring Equinox (top), June Solstice (middle) and Fall Equinox (bottom). Several obvious features, including the relatively larger diurnal variation observed at the lower latitudes, and the lack of significant diurnal variation at high latitudes, were also reported [191]. It was also noted that the maximum (minimum) average temperature did not occur close to the sub-solar (anti-solar) point but at higher latitudes. The solstice curves show the basic winter-to-summer temperature gradient, while the situation is more symmetric at equinox.

A selected set of the OGO-6 FPS observations were used to synthesize a global exospheric temperature model M1 [139], using a spherical harmonic expansion scheme [192], also used in other semi-empirical models [119,140]. This model (M1) was later improved with the addition of complementary temperature measurements at three incoherent scatter radar sites and called version M2 [193]. The M1 model was re-formulated using magnetic coordinates [194] in order to provide an improved description of the high-latitude magnetic activity effects on the exospheric temperature.

Finally, further improvements were made upon the model [195] by incorporating information derived from satellite drag measurements (model DTM). The details of these various models as well as relevant comparisons with other models and data-sets have been discussed in the papers referenced, as well as by others [196-199]. It is noteworthy that this sequence of global thermospheric temperature models is the only one in existence that is derived from the direct measurements of kinetic temperatures, rather than inferences based on constituent density measurements.

A second optical remote-sensing Fabry-Perot spectrometer, this time using a plane etalon, was placed on the Dynamics Explorer 2 spacecraft. The two Dynamics Explorer satellites were designed to perform detailed studies of the coupling between the solar

wind/magnetosphere and the ionosphere and upper atmosphere of the Earth. To this end, the two spacecraft were placed in co-planar, polar orbits, DE-1 in a high (4.5 R_e) apogee orbit and DE-2 in a low altitude (300 by 1000 km) orbit [200].

The studies performed by these spacecraft (DE-1 is still operating at the time of writing) were the logical successors to studies of atmospheric photochemistry by the Atmosphere Explorer (AE) series and of magnetospheric processes by the International Sun-Earth Explorer (ISEE) series. The DE-1 spacecraft was instrumented to measure parameters of the magnetosphere, including fields, waves, and particle distributions. It also had on board a Spin-Scan Auroral Imager [201] which has provided images of the global-scale aurorae in both Northern and Southern Hemispheres. DE-2 was instrumented in a similar fashion to the earlier AE spacecraft, with the addition of instrumentation capable of directly measuring the kinetic temperature and vector neutral wind velocity in the thermosphere. We review here the contributions made by the Dynamics Explorer data analysis, concentrating on optical measurements of dynamics and thermodynamics.

The Fabry-Perot Interferometer (FPI) [66] and the Wind and Temperature Spectrometer (WATS) [202] on DE-2 were both capable of measuring the kinetic temperature of the thermosphere and, in combination, of determining the vector neutral wind. The FPI was similar to the FPS flown on OGO-6, except that it had the stability to be able to measure the line-of-sight wind velocity by determining the Doppler shift of the OI emission at 15867K. The instrument scanned the limb of the Earth ahead of and below the polar-orbiting satellite in a similar fashion to the FPS on OGO-6, shown in Figure 56.

The resulting line-of-sight wind component (along the geographic meridian) could be appropriately averaged and phase-shifted [203] to match the in-situ, zonal component of the wind measured using the WATS baffled mass spectrometer technique [202]. The vector addition of the two components allowed the vector neutral wind field to be monitored on a global-scale for appropriate orbital configurations (altitude below approx 700 km, daytime, dusk or auroral conditions [203]).

Figure 59 illustrates results from the combination of these two instruments [203]. Horizontal vector winds (the WATS also measured the in-situ vertical wind component), are displayed along the track of the DE-2 satellite as it crossed the Northern (winter) and Southern (summer) Hemisphere polar regions. The data, taken from orbital crossings separated in time, are plotted in a quasi-inertial geomagnetic reference frame to illustrate the twin-cell motion observed in the upper thermosphere at high-latitudes. There are two contra-rotating vortex systems, one on the dusk- and the other on the dawn-side of the polar cap, which are driven by ion drag forces.

The neutral wind speed in the polar regions during the period of the DE-2 mission (solar maximum conditions) often reached magnitudes of 600-800 m/sec. Data from several thousands of such orbital passes taken between August 1981, and February 1983, have been collated and this information has provided the first truly global-scale view of the high-latitude upper thermosphere dynamics. The neutral wind measurements have been compared with predictions by the numerical general circulation models of the thermosphere [79,80] and have enabled these models to be critically tested and refined.

DE-2 wind and temperature measurements from high-latitudes have been analyzed in a number of studies and the importance of the ion drag momentum source of magnetospheric origin has been stressed in many of these. It has been shown [204], for example, that the average polar circulation system can be conveniently described by the superposition of the 'rotational' twin-vortex flow on a mean 'divergent' solar-driven flow of approx 120-150m/sec magnitude (flowing away from the mid-afternoon sector across the polar cap). Data from individual orbits of DE-2 have been compared with the predictions of the NCAR-TGCM and the UCL-TGCM and good general agreement was found for both winter and summer polar regions [205]. The same authors used averaged data from several hundreds of orbits to provide a global-scale description of the mean thermospheric wind and temperature structure in the winter and summer hemispheres. These averaged results were also compared with model predictions and indicated reasonable first-order agreement. Observed wind features, such as the anti-sunward polar cap flow and the dusk and dawn reversals to sunward flow, were in qualitative agreement with the model calculations for the neutral wind field driven by ionospheric convection. This comparison was critical in generating confidence that the physical description of the important thermospheric driving mechanisms contained within the models were valid.

Significant discrepancies between the detailed experimental data set and theoretical predictions, however, were also evident, indicating that further refinements of the model input parameterizations and boundary conditions were required. A later study included average neutral wind measurements from DE-2 and from the network of Northern hemisphere ground-based Fabry-Perot observatories [206]. This comprehensive data set enabled climatological 'weather' maps of the thermospheric circulation to be collated as a function of Universal Time during a 'mean day' in December 1981. These maps were also

compared with model predictions and excellent agreement between the major features of the observed mean circulation and the model calculations was obtained. Figure 60 shows an example of the comparison for three specific Universal Time.

Further detailed comparisons of the DE-2 results and theory have been carried out, using parametric studies of model inputs to improve the understanding of the interplay between the various thermospheric forcing mechanisms [89,95,97,207-209]. The DE-2 wind and temperature measurements have been used in a series of papers [89,95,97,207] to test the UCL general circulation model that forms the basis of the thermosphere dynamics section (Chapter 2) of the CIRA 1986 model atmosphere.

Seven polar passes of DE-2 were first studied and compared with the model [207]. Results from three of these orbits and model calculations are shown in Figure 61. The major features of the satellite thermospheric winds, such as the mean day-to-night circulation caused by solar EUV and UV heating, augmented by magnetospheric processes at high latitude and the sharp boundaries and flow reversals imposed on the neutral flow by ion drag were qualitatively similar to model predictions.

A second study focussed on the sunward flow region observed in the evening auroral oval [95] during geomagnetically disturbed periods, and compared DE-2 observations with model predictions and ground-based Fabry-Perot measurements from Kiruna, Sweden.

In a third, comprehensive study, averaged measurements of winds, temperatures and neutral constituent densities from DE-2 were compared with a selection of UCL-TGCM runs for both summer and winter polar regions [97]. The major objective of this study was to investigate the overall morphology of energy and momentum inputs to the thermosphere due to geomagnetic sources for the epoch covered by the segment of the mission under study. The combination of wind, temperature, and composition data allowed a critical evaluation of the geomagnetic inputs at all levels in the thermosphere. The final study in this series [89], was an investigation into the characteristic high-latitude wind signatures dependent on the magnitude and orientation of the interplanetary magnetic field (IMF). These signatures have been observed in the DE-2 wind measurements [88,210], and are caused by similar, IMF-dependent signatures in ionospheric convection.

It was found that a suitable modification of the input ionospheric convection patterns used in the model produced similar asymmetric wind patterns to those observed by DE-2. Figure 62 shows wind signatures from DE-2, illustrating the dependence on the sign of the IMF B_y component [88].

Similar experiment/theory comparison studies to those described above have been undertaken using the NCAR-TGCM [80,208]. As with the UCL model, a good general agreement between DE-2 wind, temperature and composition experimental data and NCAR-TGCM theoretical calculations was found, essentially validating the model and enabling a series of theoretical diagnostic studies to be undertaken to provide additional insight into the physics of the thermosphere [211-213].

In other studies, neutral wind data from DE-2 have also been compared with ground-based Fabry-Perot observations from Svalbard [214]; good agreement was found between the ground-based and spaceborne techniques for conditions of near-spatial-conjugacy and temporal simultaneity. Also, wind information from the DE Fabry-Perot has been used in studies of ion-neutral momentum coupling in the high-latitude F-region [210,215].

FUTURE DIRECTIONS

As has been illustrated by the above discussion, there has been a growing and significant reliance placed upon optical techniques to define the global dynamical and thermodynamical state of the Earth's upper atmosphere. Whereas much of the work performed to date has necessarily involved the analysis of information gained from single observatories, the ability to constrain effectively the theoretical models, using single station data, is becoming more and more limited as the models increase in sophistication. There is a need, therefore, to increase the coordinated aspect of upper atmospheric research by synthesizing information from many observatories to provide more truly global scale information. Such coordinated research is still in its infancy for optical aeronomy, but the scientific potential is certainly large for the future.

Although much progress has been made towards expressing in quantitative terms the state variables of the upper atmosphere, significant gaps in our knowledge persist, where completely untested theoretical model predictions hold sway. The lower thermosphere, for example, is poorly understood, owing to the paucity of optical emission measurements from this region of the atmosphere, and because of the difficulty of maintaining satellite orbits in the appropriate altitude region for in-situ sensing. Progress here will depend to a large extent on the development of the next generation of active and passive optical devices, designed to have increased sensitivity and altitude resolution. LIDAR (active)

systems with incoherent and coherent detection techniques will play a significant role here, together with high-sensitivity Fabry-Perot and Michelson interferometers.

Another example of an area that requires significant exploratory work is in the topic of mesosphere-thermosphere coupling. Recent theoretical work has indicated that wave and tidal forcing processes of mesospheric origin can have significant effects on the chemistry and dynamics of the thermosphere. Ground-based efforts to describe in quantitative terms both the spectrum and importance of upward propagating tides and waves represent a new frontier for optical aeronomy.

The lack of future planned spacecraft missions designed to study the upper atmosphere above the mesopause, at the time of writing, implies that there will be an important and continued role for networks of ground-based optical instruments using modern techniques, which will become increasingly important if further progress is to take place.

ACKNOWLEDGEMENTS.

We would like to thank many colleagues for their support, helpful comments, and inspiration while this text was prepared. This work was supported in part by AFOSR-ISSA-00046 and NSF (ATM-8412828) and NASA (NAG-5-465) grants to the University of Michigan.

REFERENCES

[1] CIRA 1972, Cospar International Reference Atmosphere 1972, Akademie-Verlag, Berlin, (1972).
[2] BABCOCK, H.D., Astrophys. J.,57, 209, (1923).
[3] ARMSTRONG, E.B., J. Atmos. Terr. Phys., 3, 274, (1953).
[4] BUISSON, H. and Ch. FABRY, J. Physique, 9, 442, (1912).
[5] DONAHUE, T.M., B. GUENTHER, and R.J. THOMAS, J. Geophys. Res., 78, 6662, (1973).
[6] VEGARD, L. and L. HARANG, Geophys. Pub., Oslo, 11, (1), (1934).
[7] VEGARD, L., Phil. Mag., 24, 588, (1937).
[8] DUFAY, J., J. CABANNES, and J. GAUZIT, L'Astronomie, 56, 149, (1942).
[9] CABANNES, J. and J. DUFAY, Compt. Rend., 240, 37, (1955).
[10] CABANNES, J. and J. DUFAY, J. Phys. Rad., 16, 1295, (1955).
[11] WARK, D.Q. and J.M. STONE, Nature, 175, 254, (1955).
[12] WARK, D.Q., Nature, 178, 689, (1956).
[13] CABANNES J. and J. DUFAY, Rev. d'Opt., 35, 103, (1956).
[14] CABANNES J. and J. DUFAY, in The Airglow and the Aurorae, E.B. Armstrong and A. Dalgarno, eds., Pergamon Press, Oxford, 73, (1956).
[15] PHILLIPS, J.G., in The Airglow and the Aurorae, E.B. Armstrong and A. Dalgarno, eds., Pergamon Press, Oxford, 67, (1956).
[16] KARANDIKAR, R.V., in The Airglow and the Aurorae, E.B. Armstrong and A. Dalgarno, eds., Pergamon Press, Oxford, 374, (1956).
[17] WARK, D.Q., Astrophys. J., 131, 491, (1960).
[18] MULYARCHICK, T.M., Bull. (Izv.) Acad. Sci. U.S.S.R., Geophys. Ser., 3, 297 (1960).
[19] MULYARCHICK, T.M., and P.V. SHCHEGLOV, Planet. Space Sci., 10, 215, (1963).
[20] JACQUINOT, P. and Ch. DUFOUR, J. Rech. Centre. Nat. Rech. Sci., 6, 91, (1948).
[21] JACQUINOT, P., J. Opt. Soc. Am., 44, 761, (1954).
[22] ARMSTRONG, E.B., in The Airglow and the Aurorae, E.B. Armstrong and A. Dalgarno, eds., Pergamon Press, Oxford, 366, (1956).
[23] BIONDI, M.A., Rev. Sci. Inst., 27, 36, (1956).
[24] ARMSTRONG, E.B., J. Phys. Rad., 19,358 (1958).
[25] ARMSTRONG, E.B., J. Atmos. Terr. Phys., 13, 205, (1959).
[26] PERRIN, M., Compt. Rend., 250, 2406, (1960).
[27] PERRIN, M. and A. VASSY, Compt. Rend., 250, 2740, (1960).
[28] JEANNET, J-C. and A. VASSY, Ann. Geophys., 19, 80, (1963).
[29] NILSON, J.A. and G.G. SHEPHERD, Planet. Space Sci., 5, 299, (1961).
[30] TURGEON, E.C. and G.G. SHEPHERD, Planet. Space Sci., 9, 295, (1962).
[31] NASYROV, G.A., Geomag. & Aeron., 9, 762, (1969).
[32] JARRETT, A.H., M.J. HOEY, and L. PAFFRATH, Planet. Space. Sci., 12, 591, (1964).
[33] HERNANDEZ, G. and J.P. TURTLE, Planet. Space Sci., 13, 301, (1965).
[34] JARRETT, A.H. and M.J. HOEY, Proc. Roy. Soc. (London), 288, 175, (1965).
[35] ARMSTRONG, E.B., Japan J. Appl. Phys., 4, Supp. 1, 535, (1965).
[36] BENS, A.R., L.L.COGGER , and G.G. SHEPHERD, Planet. Space Sci., 13, 551, (1965).
[37] JARRETT, A.H. and M.J. HOEY, J. Atmos. Terr. Phys., 28, 175, (1966).
[38] HERNANDEZ, G. and J.P. TURTLE, in Aurora and Airglow, B. M. McCormac, ed., Reinhold Publishing Corp., New York, 435, (1967).
[39] BIONDI, M.A. and W,A. FEIBELMAN, Planet. Space. Sci., 16, 431, (1968).
[40] ARMSTRONG, E.B., Planet. Space Sci., 16, 211, (1968).
[41] ARMSTRONG, E.B., Planet. Space Sci., 17, 957, (1969).
[42] FABRY, Ch. and H. BUISSON, Compt. Rend., 158, 1498, (1914).

[43] BUISSON, H., FABRY, Ch. and BOURGET, H., J. Physique, 4, 357, (1914).
[44] CHAMBERLAIN, J.W., Physics of the Aurora and Airglow, Academic Press, New York, (1961).
[45] BORN, M. and E. WOLF, Principles of Optics, Pergamon Press, Oxford, (1964).
[46] HERNANDEZ, G. Fabry-Perot Interferometers, Cambridge University Press, Cambridge, (1986).
[47] Aspen International Conference on Fourier Spectroscopy, G.A. Vanasse, A.T. Stair and D.J. Baker, eds., AFCRL-71-0019, Special Reports, No. 114, Air Force Cambridge Research Laboratories, Bedford, MA, (1971).
[48] HILLIARD, R.L. and G.G. SHEPHERD, Planet. Space. Sci., 14, 383, (1966).
[49] HILLIARD, R.L. and G.G. SHEPHERD, J. Opt. Soc. Am., 56, 362, (1966).
[50] BERG, D.E., M. KOOMEN, L. MEREDITH, and R. SCOLNICK, J. Geophys. Res., 61, 302, (1956).
[51] KOOMEN, M., R. SCOLNICK, and R. TOUSEY, J. Geophys. Res., 61, 304, (1956).
[52] HEPPNER, J.P. and L.H. MEREDITH, J. Geophys. Res., 63, 51, (1958).
[53] TOUSEY, R., Ann. Geophys., 14, 186, (1958).
[54] COOPER, H.W., I.S. GULLEDGE, M.J. KOOMEN and D.M. PACKER, J. Geophys. Res., 65, 2484, (1960).
[55] PACKER, D.M., Ann. Geophys., 17, 161, (1961).
[56] TARASOVA, T.M., Space Res., 3, 162, (1963).
[57] O'BRIEN, B.J., F.R. ALLUM and H.C. GOLDWIRE, J. Geophys. Res., 70, 161, (1965).
[58] GREER, R.G.H., and G.T. BEST, Planet. Space. Sci., 15, 1857, (1967).
[59] HURUHATA, M., T. NAKAMURA and W.R. STEIGER, Rep. Ionos. Res. Space Res. Japan, 21, 229, (1967).
[60] HURUHATA, M., T. NAKAMURA and H. TANABE, Rep. Ionos. Res. Space Res. Japan, 21, 223, (1967).
[61] BAKER, D.J. and R.O. WADDOUPS, J. Geophys. Res., 72, 4881 (1967); 73, 2546, (1968).
[62] GULLEDGE, I.S., D.M. PACKER, S.G. TILFORD and J.T. VANDERSLICE, J. Geophys. Res., 73, 5535, (1968).
[63] DANDEKAR, B.S., and J.P. TURTLE, Planet. Space Sci., 19, 949, (1971).
[64] THOMAS, R.J. and R.A. YOUNG, J. Geophys. Res., 86, 7389, (1981).
[65] BLAMONT, J.E., and J.M. LUTON, J. Geophys. Res., 77, 3534, (1972).
[66] HAYS, P.B., T.L KILLEEN and B.C. KENNEDY, Space Sci. Inst., 5, 395, (1981).
[67] BANKS, P.M., and G. KOCKARTS, Aeronomy, Academic Press, New York, (1973).
[68] ROBLE, R.G., P.B. HAYS and A.F. NAGY, Planet. Space Sci., 16, 1109, (1968).
[69] HERNANDEZ, G., T.E. VANZANDT, V.L. PETERSON and J.P. TURTLE, J. Geophys. Res., 80, 3271, (1975).
[70] HAYS, P.B., A.F. NAGY, K.D. MCWATTERS and J.V. EVANS, J. Geophys. Res., 75, 4881, (1970).
[71] COGGER, L.L., G.J. NELSON, M. A. BIONDI, R.D. HAKE and D.P. SIPLER, J. Geophys. Res., 75, 4887, (1970).
[72] HERNANDEZ, G., J. Geophys. Res., 79, 1119, (1974).
[73] NAGY, A.F, R.J. CICERONE, P.B. HAYS, K.D. MCWATTERS, J.W. MERIWETHER, A.E. BELON and C.L. RINO, Radio Science, 9, 315, (1974).
[74] HAYS, P.B., J.W. MERIWETHER, and R.G. ROBLE, J. Geophys. Res., 84, 1905, (1979).
[75] MERIWETHER, J.W., J.P. HEPPNER, J.D. STOLARIK, and E.M. WESCOTT, J. Geophys. Res., 78, 6643, (1973).
[76] STOFFREGEN, W., in Magnetosphere-ionosphere Interactions, K. Folkestad, ed., 83, Universitetforlaget, Oslo, Norway, (1972).
[77] REES, D., J. Br. Interplanet. Soc., 24, 233, (1971).
[78] WICKWAR, V.B., J.W. MERIWETHER, P.B. HAYS, and A.F. NAGY, J. Geophys. Res., 89, 10987, (1984).
[79] FULLER-ROWELL, T.J., and D. REES, J. Atmos. Terr. Phys., 37, 701, (1981).
[80] DICKINSON, R.E., E.C. RIDLEY, and R.G. ROBLE, J. Geophys. Res., 86, 1499, (1981).
[81] SMITH, R.W., in Exploration of the polar upper atmosphere, C.S. Deehr and J.A. Holtet, eds., 189, D. Reidel, Hingham, Mass., (1980).
[82] SMITH, R.W. and P.J. SWEENEY, Nature, 284, 437, (1980).
[83] SMITH, R.W., G.G. SIVJEE, R.D. STEWART, F.G. MCCORMAC, and C.S. DEEHR, J. Geophys. Res., 87, 4455, (1982).
[84] SMITH, R.W., K. HENRIKSEN, C.S. DEEHR, D. REES, F.G. MCCORMAC, and G.G. SIVJEE, Planet. Space Sci., 33, 305, (1985).
[85] MCCORMAC, F.G., and R.W. SMITH, Geophys. Res. Lett., 11, 935, (1984).
[86] DEEHR, C.S., G.G. SIVJEE, A. EGELAND, K. HENRIKSEN, P.E. SANDHOLT, R.W. SMITH, P. SWEENEY, C. DUNCAN, and J. GILMER, J. Geophys. Res., 85, 2185, (1980).
[87] REES, D., T.J. FULLER-ROWELL, and R.W. SMITH, Planet. Space Sci., 28, 919, (1980).
[88] MCCORMAC, F.G., T.L. KILLEEN, E. GOMBOSI, P.B. HAYS, and N.W. SPENCER, Geophys. Res. Lett., 12, 155, (1985).
[89] REES, D., T.J. FULLER-ROWELL, R. GORDON, M.F. SMITH, N.C. MAYNARD, J.P. HEPPNER, N.W. SPENCER, L. WHARTON, P.B. HAYS, and T.L. KILLEEN, Planet. Space Sci., 34, 1, (1986).

[90] REES, D., P.A. ROUNCE, P. CHARLETON, T.J. FULLER-ROWELL, I. MCWHIRTER, and K. SMITH, J. Geophys., 50, 202, (1982).
[91] REES, D., C.R. PHILBRICK, M. CARLSON, T.J. FULLER-ROWELL and P.CHARLETON, Adv. Space Res., 2, 129, (1983).
[92] REES, D., P. CHARLETON, N. LLOYD, A. STEEN, and G. WITT, Proc. VIth ESA Symposium on rocket and balloon studies, (ESA SP-183), 53, (1983).
[93] REES, D., R.W. SMITH, P.J. CHARLETON, F.G. MCCORMAC, N. LLOYD, and A. STEEN, Planet. Space Sci., 32, 667, (1984).
[94] REES, D., M.F. SMITH, and R. GORDON, Planet. Space Sci., 32, 685, (1984).
[95] REES, D., T.J. FULLER-ROWELL, M. SMITH, R. GORDON, T.L. KILLEEN, P.B. HAYS, N.W. SPENCER, L. WHARTON, and N.C. MAYNARD, Planet. Space Sci., 33, 425, (1985).
[96] REES, D., P. CHARLETON, M. CARLSON, and P. ROUNCE, J. Atmos. Terr. Phys. 47, 195, (1985).
[97] REES, D., R. GORDON, T.J. FULLER-ROWELL, M. SMITH, G.R. CARIGNAN, T.L. KILLEEN, P.B. HAYS, and N.W. SPENCER, Planet. Space Sci., 33, 617, (1985).
[98] WARDHILL, P., and F. JACKA, J. Atmos. Terr. Phys., 48, 289, (1986).
[99] SMITH, R.W., D. REES, F.G. MCCORMAC, and P. CHARLETON, J. Atmos. Terr. Phys., 48, 97, (1986).
[100] KILLEEN, T.L., J.W. MERIWETHER, and R.G. ROBLE, EOS, Transactions, Amer. Geophys. Union, 67, 320, (1986).
[101] MERIWETHER, J.W., C.A. TEPLEY, S.A. PRICE, P.B. HAYS and L.L. COGGER, Opt. Eng., 22, 128, (1983).
[102] MERIWETHER, J.W., P. SHIH, T.L. KILLEEN, V.B. WICKWAR, and R.G. ROBLE, Geophys. Res. Lett., 11, 931, (1984).
[103] SICA, R.J., M.H. REES, G.J. ROMICK, G. HERNANDEZ, and R.G. ROBLE, J. Geophys. Res., 91, 3231, (1986).
[104] SICA, R.J., G. HERNANDEZ, G.J. ROMICK, M.H. REES, and R.G. ROBLE, J. Geophys. Res., 91, in press (1986).
[105] SICA, R.J., M.H. REES, R.G. ROBLE, G. HERNANDEZ, and G.J. ROMICK, Planet. Space Sci., 34, 483, (1986).
[106] NAGY, A.F., P.B. HAYS and K.D. MCWATTERS, Space Res., 11, 919, (1971).
[107] FEIBELMAN, W.A., R.D. HAKE, D.P. SIPLER and M.A. BIONDI, J. Geophys. Res., 77, 1869, (1972).
[108] STEWART, R.D., R.W. SMITH, D. REES, J.R. DUDENEY, and A.S. ROGERS, Nature, 317, 45, (1985).
[109] HAYS, P.B., A.F. NAGY and R.G. ROBLE, J. Geophys. Res., 69, 4162, (1969).
[110] HAYS, P.B. and R.G. ROBLE, J. Geophys. Res., 76, 5316, (1971).
[111] HERNANDEZ, G., Planet. Space Sci., 20, 1309, (1972).
[112] SHEPHERD, G.G., in Temperature; its measurement and control in science and industry, Vol. 4, H. H. Plumb, ed., 2313, Instrum. Soc. Am., Pittsburgh, (1971).
[113] ARMSTRONG, E.B. and J.A. BELL, Planet. Space. Sci., 18, 784, (1970).
[114] KAMIYAMA, H., S. OKANO and T. ONUMA, Rep. Ionos. Space Res. Japan, 29, 195, (1975).
[115] OKANO, S. and J.S. KIM, J. Geophys. Res., 84, 4441, (1979).
[116] OKANO, S., J.S. KIM and T. ICHIKAWA, Planet. Space Sci., 33, 841, (1985).
[117] HERNANDEZ, G. and R.G. ROBLE, J. Geophys. Res., 81, 2065, (1976).
[118] HERNANDEZ, G. and R.G. ROBLE, J. Geophys. Res., 81, 5173, (1976).
[119] HEDIN, A.E., H.G. MAYR, C.A. REBER, N.W. SPENCER and G.R. CARIGNAN, J. Geophys. Res., 79, 215, (1974).
[120] CHING, B.K. and CHIU, Y.T., J. Atmos. Terr. Phys., 35, 1615, (1973).
[121] HERNANDEZ, G. and R.G. ROBLE, J. Geophys. Res., 82, 5505, (1977).
[122] ROBLE, R.G., R.E. DICKINSON and E.C. RIDLEY, J. Geophys.Res., 82, 5493, (1977).
[123] BIONDI, M.A. and J.W. MERIWETHER, Geophys. Res. Lett., 12, 267, (1985).
[124] YAGI, T. and P.L. DYSON, Planet. Space Sci., 33, 203, (1985).
[125] JACKA, F., A.R.D. BOWER and P.A. WILKSCH, J. Atmos. Terr. Phys., 41, 397, (1979).
[126] SIPLER, D.P., B.B. LUOKKALA and M.A. BIONDI, Planet. Space Sci., 20, 1025, (1982).
[127] HERNANDEZ, G., D.P. SIPLER and M.A. BIONDI, Geophys. Res. Lett., 5, 935, (1977).
[128] HERNANDEZ, G. and R.G. ROBLE, J. Geophys. Res., 83, 5531, (1978).
[129] ROBLE, R.G., A.D. RICHMOND, W.L. OLIVER and R.M. HARPER, J. Geophys. Res., 83, 999, (1978).
[130] ROBLE, R.G., R.E. DICKINSON, E.C. RIDLEY and Y. KAMIDE, J. Geophys. Res., 83, 5531, (1978).
[131] HERNANDEZ, G. and R.G. ROBLE, Geophys. Res. Lett., 8, 835, (1978).
[132] CUMMINGS, W.D. and A.J. DESSLER, J. Geophys. Res., 72, 257, (1967).
[133] HERNANDEZ, G., R.G. ROBLE and J.H. ALLEN, Geophys. Res. Lett., 7, 677, (1980).
[134] SIPLER, D.P. and M.A. BIONDI, J. Geophys. Res., 84, 37, (1979).
[135] AKASOFU, S-I, Planet. Space Sci., 27, 425, (1979).
[136] YAGI, T. and P.L. DYSON, Planet. Space Sci., 33, 465, (1985).
[137] SIPLER, D.P., M.A. BIONDI and R.G. ROBLE, Planet. Space Sci., 29, 1367, (1981).
[138] HERNANDEZ, G., J. Geophys. Res., 87, 1623, (1982).
[139] THUILLIER, G., J.L. FALIN and C. WACHTEL, J. Atmos. Terr. Phys., 39, 399, (1977).

[140] HEDIN, A.E., J.E. SALAH, J.V. EVANS, C.A. REBER, G.P. NEWTON, N.W. SPENCER, D.C. KAYSER, D. ALCAYDE, P. BAUER, L. COGGER and J.P. MCCLURE, J. Geophys. Res., 82, 2139, (1977).
[141] JACCHIA, L.G., Spec. Rep. 335, Smithson. Astrophys. Obs., Cambridge, MA, (1977).
[142] VON VAHN, U., W. KOHNLEIN, K.H. FRICKE, U. LAUX, H. TRINKS and H. VOLLAND, Geophys. Res. Lett., 4, 33, (1977).
[143] TORR, M.R., D.G. TORR and H.E. HINTEREGGER, J. Geophys. Res., 85, 6063, (1981).
[144] HEDIN, A.E., J. Geophys. Res., 89, 9828, (1984).
[145] JACCHIA, L.G., in CIRA 1965, p.293, North-Holland, Amsterdam, (1965).
[146] JACCHIA, L.G., Smithson. Contrib. Astrophys., 8, 215, (1965).
[147] ROEMER, M., in CIRA 1972, 340, Akademie-Verlag, Berlin, (1972).
[148] HERNANDEZ, G. and R.G. ROBLE, J. Geophys. Res., 89, 327, (1984).
[149] HERNANDEZ, G. and R.G. ROBLE, Geophys. Res. Lett., 6, 294, (1979).
[150] HERNANDEZ, G., R.G. ROBLE, E.C. RIDLEY and J.A. ALLEN, J. Geophys. Res., 87, 9181, (1982).
[151] ABREU, V.J., G.A. SCHMITT, P.B. HAYS, J.W. MERIWETHER, C.A. TEPLEY and L.L. COGGER, Planet. Space. Sci., 31, 303, (1983).
[152] ROBLE, R.G., R.E. DICKINSON and E.C. RIDLEY, J. Geophys. Res., 87, 1599, (1982).
[153] TINSLEY, B.A., J. Atmos. Terrest. Phys.,43, 617, (1981).
[154] HERNANDEZ, G. and R.G. ROBLE, J. Geophys. Res., 89, 9049, (1984).
[155] BARMORE, F.E., Planet. Space Sci., 25, 185, (1977).
[156] COCKS, T.D. and F. JACKA, J. Atmos. Terr. Phys., 41, 409, (1979).
[157] JACCHIA, L., Spec. Rep. 332, Smithson. Astrophys. Obs., Cambridge, MA, (1971).
[158] SIPLER, D.P., and M.A. BIONDI, Geophys. Res. Lett., 5, 373, (1978).
[159] SIPLER, D.P., M.A. BIONDI, and R.G. Roble, Planet. Space Sci., 31, 53, (1983).
[160] BIONDI, M.A., and D.P. SIPLER, Planet. Space Sci., 33, 817, (1985).
[161] BURNSIDE, R.G., F.A. HERRERO, J.W. MERIWETHER, and J.C.G. WALKER, J. Geophys. Res., 86, 5532, (1981).
[162] BURNSIDE, R.G., J.C.G. WALKER, R.A. BEHNKE, and C.A. GONZALES, J. Geophys. Res., 88, 6259, (1983).
[163] MERIWETHER, J.W., M.A. BIONDI, and D.N. ANDERSON, Geophys. Res. Lett, 12, 487, (1985).
[164] MERIWETHER, J.W., J.W. MOODY, M.A. BIONDI, and R.G. ROBLE, J. Geophys. Res., 91, 5557, (1986).
[165] HERNANDEZ, G., J. Geophys. Res., 81, 5165, (1976).
[166] THOMAS, R.J. and T.M. DONAHUE, J. Geophys. Res., 77, 3357, (1972).
[167] COGGER, L.L. and C.D. ANGER, J. Atmos. Terr. Phys., 35, 2081, (1973).
[168] HERNANDEZ, G., Planet. Space. Sci., 19, 467, (1971).
[169] MERIWETHER, J.W., in Handbook for MAP, Vol. 13, R.A. Vincent, ed., 1, SCOSTEP, (1984).
[170] KARANDIKAR, R.V., Planet. Space. Sci., 16, 211, (1968).
[171] KAMIYAMA, H., S. OKANO, T. ONUMA and T. ICHIKAWA, Rep. Ionos. Space. Res. Japan, 29, 171, (1975).
[172] HERNANDEZ, G., J. Geophys. Res., 82, 2127, (1977).
[173] HERNANDEZ, G. and S. MATSUSHITA, in Proceedings of the International Conference on Recent Advances in the Physics and Chemistry of the E-region, 158, National Center for Atmospheric Research, Boulder, (1974).
[174] SMITH, J.L., G. HERNANDEZ, V.B. WICKWAR and R.T. TSUNODA, EOS, Transactions, Amer. Geophys. Union, 64, 274, (1983).
[175] HERNANDEZ, G., and R.G. ROPER, J. Geomag. Geoelect., 31, 419, (1979).
[176] HERNANDEZ, G., Opt. Eng., 19, 518, (1980).
[177] COGGER, L.L., J.S. MURPHREE, C.A. TEPLEY and J.W. MERIWETHER, Planet. Space Sci., 19, 518, (1985).
[178] CHANIN, M.L. and G.F. TULINOV, J. Geophys. Res., 84, 406, (1979).
[179] GROVES, G.V., in CIRA 1972, 33, Akademie-Verlag, Berlin, (1972).
[180] JOHNSON, F.S. and B. GOTTLIEB, Planet. Space. Sci., 21, 1001, (1973).
[181] REBER, C.A. and P.B. HAYS, J. Geophys. Res., 78, 2977, (1973).
[182] WALLACE, J.M., Rev. Geophys. Space Phys., 11, 191, (1973).
[183] MATSUNO, T., J. Atmos. Sci., 28, 1479, (1971).
[184] GEISLER, J.E., J. Geophys. Res., 79, 4989, (1974).
[185] PETEHERYCH, S., G.G. SHEPHERD and J.K. WALKER, Planet. Space Sci., 33, 869, (1985).
[186] HERNANDEZ, G., Geophys. Res. Lett., 2, 103, (1975).
[187] SIPLER, D.P. and M.A. BIONDI, Geophys. Res. Lett., 2, 106, (1975).
[188] SIPLER, D.P. and M.A. BIONDI, Planet. Space. Sci., 26, 65, (1978).
[189] HERNANDEZ, G. and J.L. SMITH, Geophys. Res. Lett., 11, 534, (1984).
[190] SMITH, R.W., G.J. ROMICK R. VIERECK and G. HERNANDEZ, EOS, Transactions, Amer. Geophys. Union, 67, 319, (1986).
[191] BLAMONT, J., J.M. LUTON and J.S. NISBET, Radio Sci., 9, 47, (1974).
[192] MAYR, H.G., and H. VOLLAND, J. Geophys. Res., 77, 6774, (1972).
[193] THUILLIER, G., J.L. FALIN, and F. BARLIER, J. Atmos. Terr. Phys., 39, 1195, (1977).
[194] THUILLIER, G., J.L. FALIN and F. BARLIER, J. Atmos. Terr. Phys., 42, 653, (1980).

[195] BARLIER, F., C. BERGER, J.L. FALIN, G. KOCKARTS, and G. THUILLIER, Ann. Geophys., 34, 9, (1978).
[196] BARLIER, F., C. BERGER, J.L. FALIN, G. KOCKARTS and G. THUILLIER, J. Atmos. Terr. Phys., 41, 527, (1979).
[197] KOCKARTS, G., Adv. Space Res., 1, 197, (1981).
[198] HICKMAN, D.R., B.K. CHING, C.J. RICE, L.R. SHARP and J.M. STRAUS, Rep. SAMSO-TR-79 57, Aerospace Corporation, Los Angeles, CA. (1979).
[199] BARLIER, F., and C. BERGER, Planet. Space Sci., 31, 945, (1983).
[200] HOFFMAN, R.A., G.D. HOGAN, and R.C. MAEHL, Space Sci. Instrum., 5, 349, (1981).
[201] FRANK, L.A., J.D. CRAVEN, K.L. ACKERSON, M.R. ENGLISH, R.H. EATHER, and R. CAROVILLANO, Space Sci. Instrum., 5, 369, (1981).
[202] SPENCER, N.W., L.E. WHARTON, H.B. NIEMANN, A.E. HEDIN, G.R. CARIGNAN, and J.C. MAURER, Space Sci. Instrum., 5, 417, (1981).
[203] KILLEEN, T.L., P.B. HAYS, N.W. SPENCER, and L.E. WHARTON, Geophys. Res. Lett., 9, 957, (1982).
[204] KILLEEN, T.L., P.B. HAYS, N.W. SPENCER, and L.E. WHARTON, Adv. Space Res., 2, 133, (1983).
[205] HAYS, P.B., T.L. KILLEEN, N.W. SPENCER, L.E. WHARTON, R.G. ROBLE, B.A. Emery, T.J. FULLER-ROWELL, D. REES, L.A. FRANK, and J.D. CRAVEN, J.Geophys Res., 89,5597, (1984).
[206] KILLEEN, T.L., R.G. ROBLE, R.W. SMITH, N.W. SPENCER, J.W. MERIWETHER, D. REES, G. HERNANDEZ, P.B. HAYS, L.L. COGGER, D.P. SIPLER, M.A. BIONDI, and C.A. TEPLEY, J. Geophys. Res., 91, 1633, (1986).
[207] REES, D., T.J. FULLER-ROWELL, R. GORDON, T.L. KILLEEN, P.B. HAYS, L.E. WHARTON, and N.W. SPENCER, Planet. Space Sci., 31, 1299, (1983).
[208] ROBLE, R.G., R.E. DICKINSON, E.C. RIDLEY, B.A. EMERY, P.B. HAYS, T.L. KILLEEN, and N.W. SPENCER, Planet. Space Sci., 31, 1479, (1983).
[209] ROBLE, R.G., B.A. EMERY, R.E. DICKINSON, E.C. RIDLEY, T.L. KILLEEN, P.B. HAYS, G.R. CARIGNAN, and N.W. SPENCER, J. Geophys. Res., 89, 9057, (1984).
[210] KILLEEN, T.L., R.A. HEELIS, P.B. HAYS, N.W. SPENCER, and W.B. HANSON, Geophys. Res. Lett., 12, 159, (1985).
[211] EMERY, B.A., R.G. ROBLE, E.C. RIDLEY, T.L. KILLEEN, M.H. REES, J. D. WINNINGHAM, G.R. CARIGNAN, P.B. HAYS, R.A. HEELIS, W.B. HANSON, N.W. SPENCER, L.H. BRACE, and M. SUGIURA, J. Geophys. Res., 90, 6553, (1984).
[212] KILLEEN, T.L., and R.G. ROBLE, J. Geophys. Res., 89, 7509, (1984).
[213] KILLEEN, T.L., and R.G. ROBLE, in The Polar Cusp, J. A. Holtet and A. Egeland, eds., 261, D. Reidel, 1985.
[214] KILLEEN, T.L., R.W. SMITH, P.B. HAYS, N.W. SPENCER, L.E. WHARTON, and F.G. MCCORMAC, Geophys. Res. Lett., 11, 311, (1984).
[215] KILLEEN, T.L., P.B. HAYS, G.R. CARIGNAN, R.A. HEELIS, W.B. HANSON, and L.H. BRACE, Geophys. Res., 89, 7495, (1984).

TABLE I

Ground-based Fabry-Perot Observatories

Observatory	Coordinates	Investigator	Comments
Svalbard	78.2N, 15.6E	R. W. Smith D. Rees	Cusp measurements of both neutral and ion velocities. 24-hour coverage during polar night.
Thule	76.0N, 70.0W	J. W. Meriwether T. L. Killeen	Centre of geomagnetic polar cap.
Sondrestrom	67.0N, 51.0W	J. W. Meriwether	Co-located with radar. Northern edge of auroral zone.
Fairbanks	64.8N, 147.8W	G. Hernandez R. W. Smith G. J. Romick M. H. Rees	Auroral station.
Kiruna	67.8N, 21.2E	D. Rees	Auroral station, also equipped with Doppler Imager.
Calgary	51.0N, 114.1W	L. L. Cogger J. W. Meriwether	Sub-auroral station.
Ann Arbor	42.3N, 83.7W	P. B. Hays J. W. Meriwether G. Hernandez	Mid-latitude station.
Fritz Peak	39.9N, 105.5W	G. Hernandez	Mid-latitude station. 1969-1985
Laurel Ridge	40.1N, 79.2W	M. A. Biondi	Mid-latitude station.
Mawson	66.6S, 67.9E	F. Jacka	Southern auroral station.
Halley Bay	75.5S, 26.9W	R. W. Stewart	Mid-latitude station.
Arecibo	18.3N, 67.5W	C. A. Tepley R. G. Burnside	Mid- to low-latitude. Co-located with radar.
Arequipa	16.2S, 71.4W	J. W. Meriwether M. A Biondi	Equatorial, near to radar
Camden	34.1S, 209.5E	E. B. Armstrong	Mid-latitude station
Mt. Torrens	34.9S, 138.9E	F. Jacka	Mid-latitude station.
Beveridge	37.5S, 145.1E	P. L. Dyson	Mid-latitude station.
Albany	42.7N, 73.8W	J. S. Kim	Mid-latitude station
Ny Alesund	78.9N, 11.9E	D. Rees	Polar cap station.
Saskatoon	52.0N, 107.0W	D. R. McEwen	Sub-auroral station.
Kilpisjarvi	69.4N, 20.3E	D. Rees	Auroral oval station
Madison	43.1N, 80.4W	F. L. Roesler	Mid-latitude station.

TABLE II

Zonal mean values of temperature and wind predicted at 250 km over Fritz Peak Observatory (39.9° N, 105.5° W) for 1975-1976. From reference [121].

Month	Zonal m/s	Meridional m/s	Temperature K
April	-6.8	-20.9	785.
May	-25.1	-43.3	836.
June	-27.2	-43.3	811.
July	-29.1	-41.2	814.
August	-24.5	-37.7	841.
September	-8.9	-22.2	809.
October	1.5	-14.3	792.
November	11.8	3.1	811.
December	38.1	25.5	765.
January	52.7	37.0	746.
February	35.2	23.7	752.
March	10.7	1.2	772.

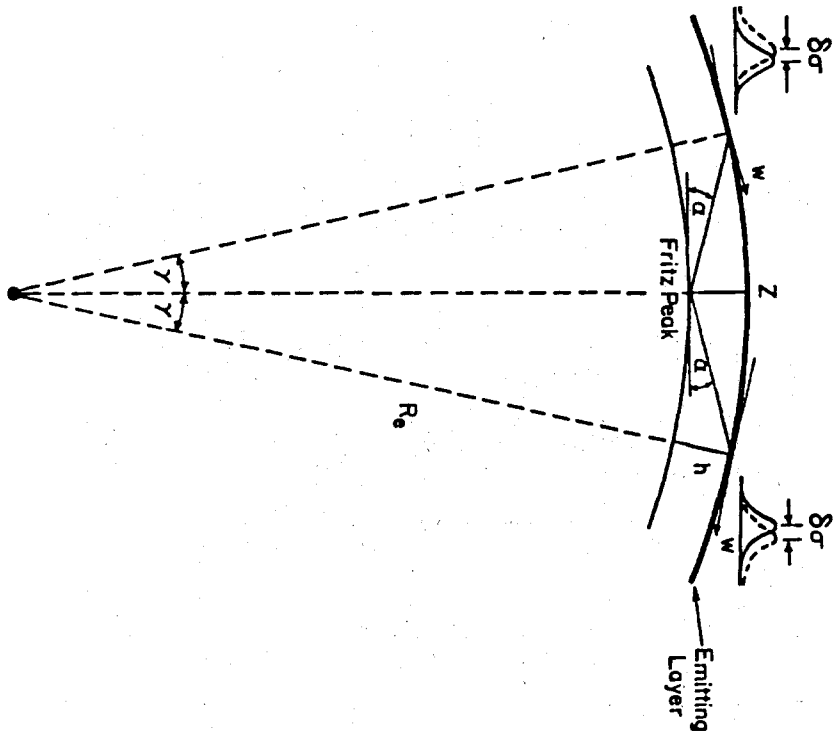

FIGURE 1. Schematic illustration of the ground-based technique used to determine Doppler shifts from atmospheric emissions. W is the horizontal wind, h is the height of emission, alpha is the sky elevation angle. Fritz Peak Observatory is located at 39.89° N and 105.5° W. From reference [117].

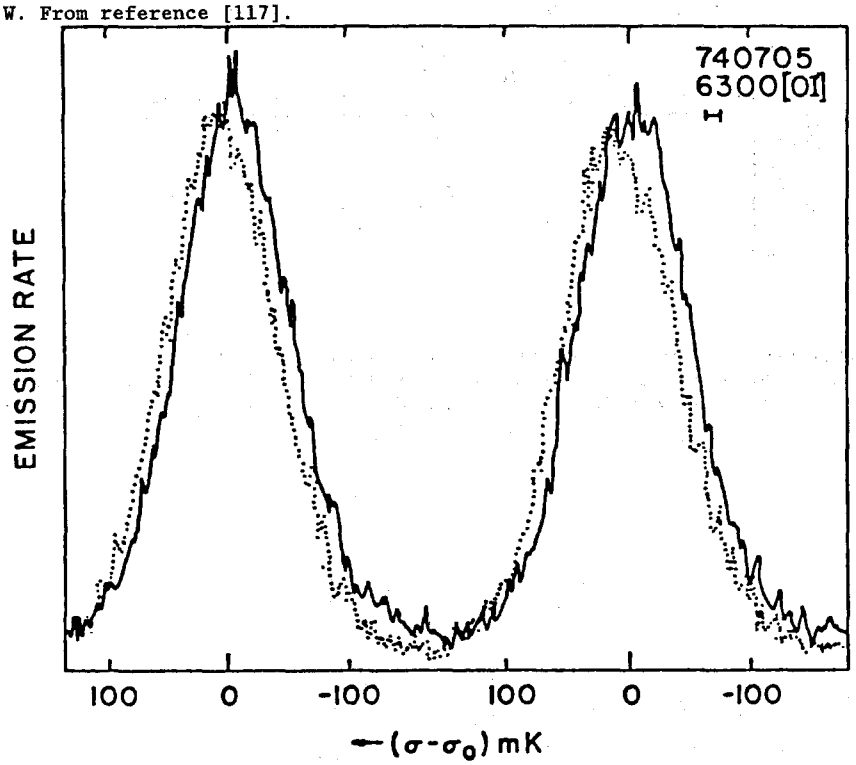

FIGURE 2. Spectral profiles of the 15867K emission measured in the nighttime. The solid curve is the reference zero wind obtained in the zenith, while the dotted curve was obtained at a 20° elevation angle looking northwards. The shift between the two profiles is equivalent to about 200 m/sec. From reference [117]

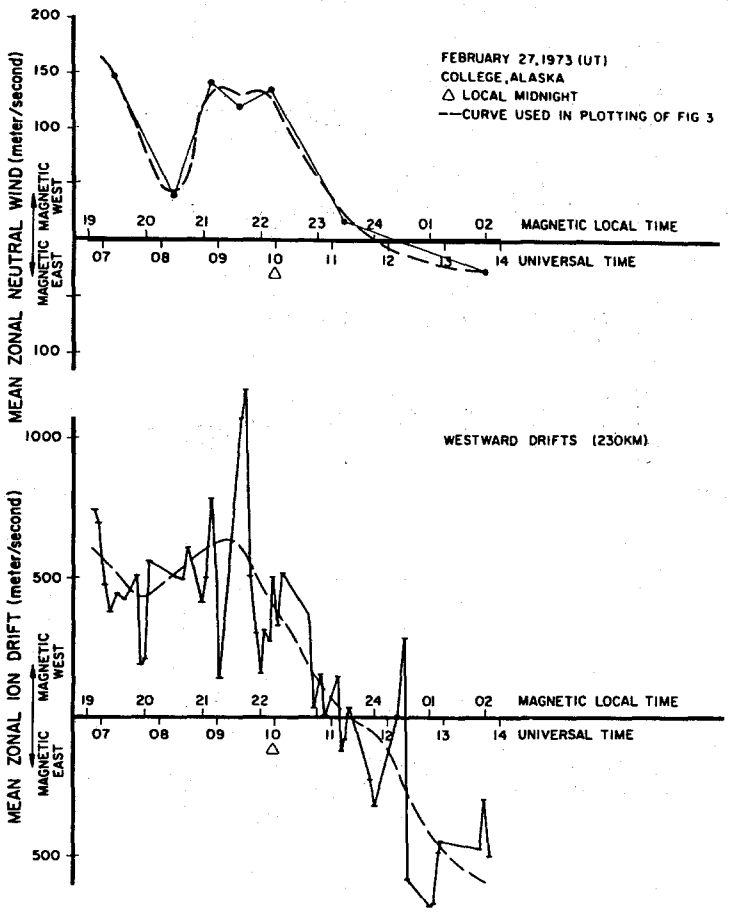

FIGURE 3. Zonal neutral wind measurements and zonal ion drift measurements from the Fabry-Perot interferometer at College, Alaska and the Chatanika radar, respectively, plotted versus UT for February 27, 1973. The dashed curves are smooth fits to the data. From reference [73]

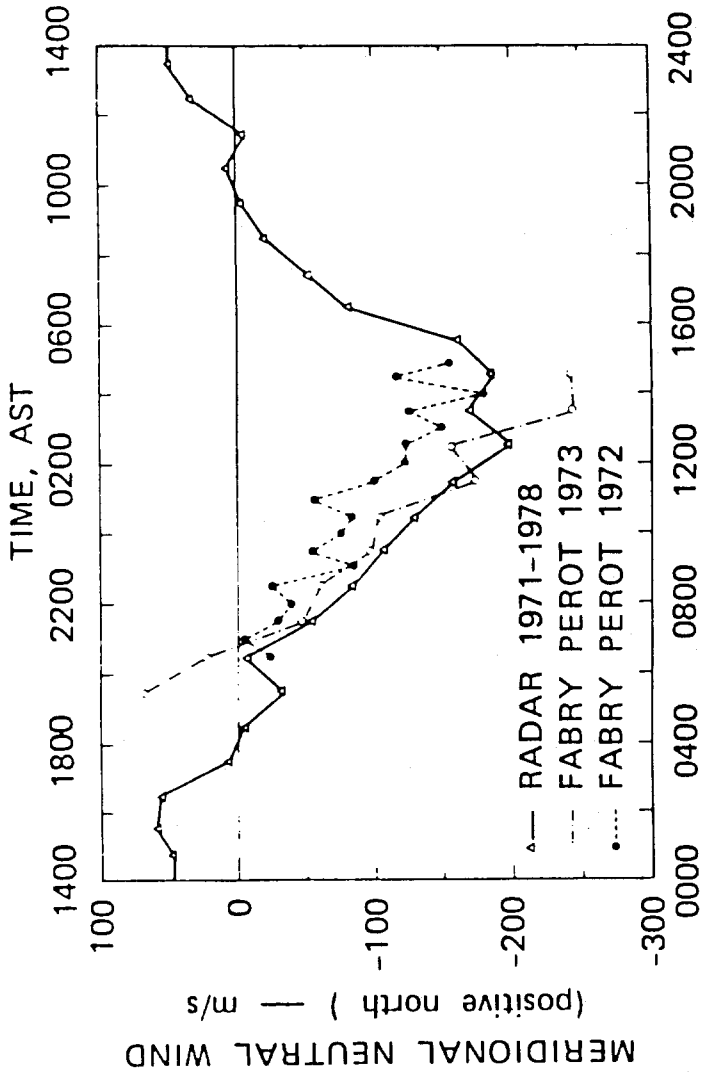

FIGURE 4. Comparison of mean meridional winds from the Chatanika radar data and from the Fabry-Perot interferometer situated at Fairbanks, Alaska. From reference [78].

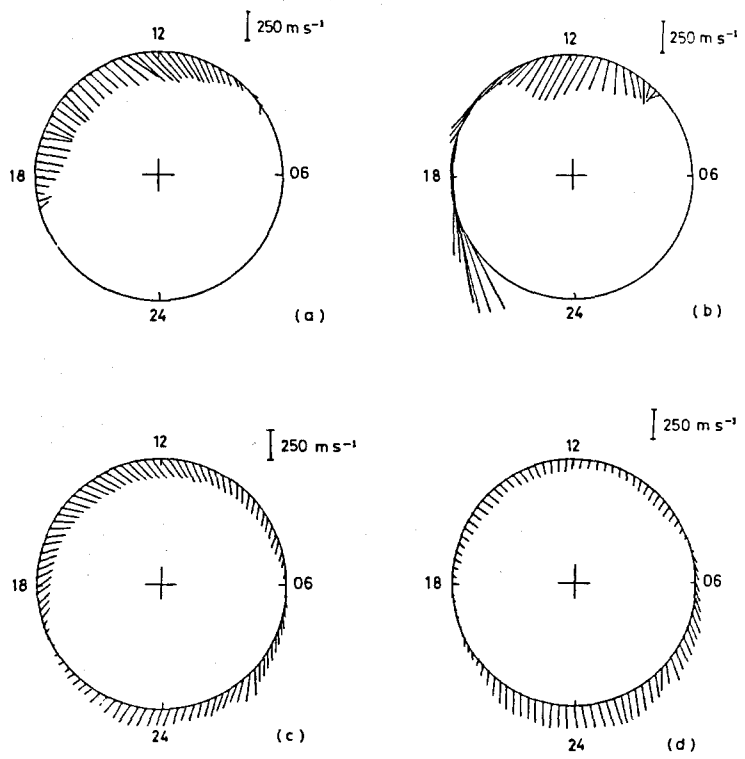

FIGURE 5. Averaged ion and neutral wind vectors measured at Svalbard, Norway. Magnetic north is marked by the cross at the centre of each circle. Magnetic local time is three hours ahead of Universal Time. (a) Ion vectors averaged over 14 days when the IMF B_y was positive and plotted at fifteen minute intervals on a circle at 75° which traces the diurnal locus of the observing site. (b) Ion vectors averaged over 3 days for IMF B_y negative. (c) Neutral wind vectors averaged over 43 days for IMF B_y positive. (d) Neutral winds averaged over 12 days for IMF B_y negative. From reference [85].

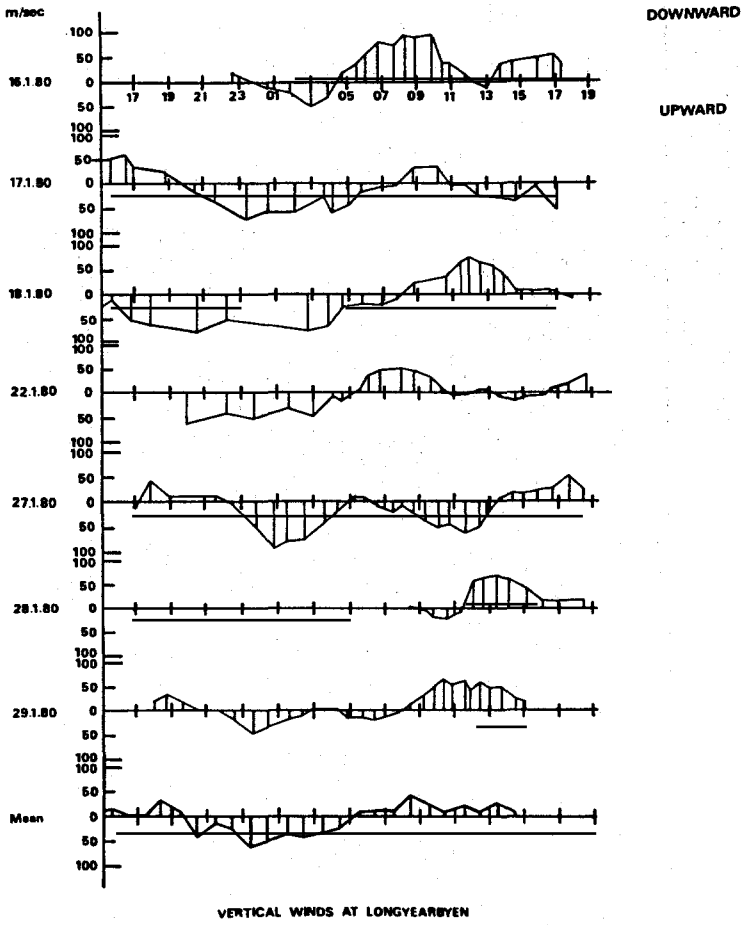

FIGURE 6. Vertical wind measurements from Svalbard in January 1981 as a function of UT for 7 nights and the mean. From reference [93].

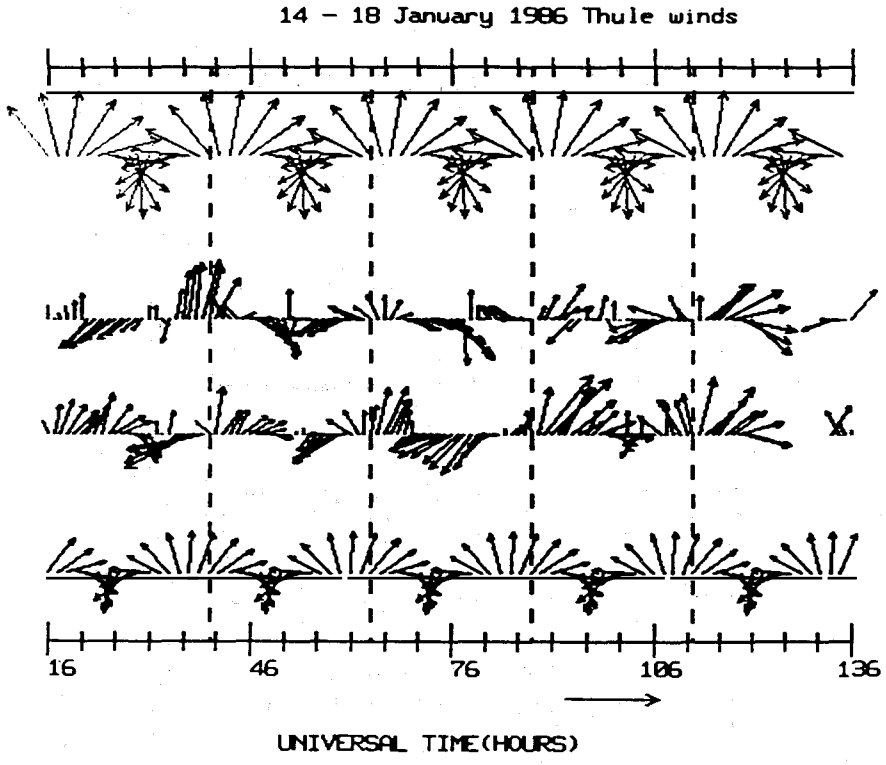

FIGURE 7. Vector neutral winds measured from Thule, Northern Greenland during January 14 - 18, 1986. Continuous measurements during the five consecutive clear days were obtained. The top and bottom vector traces show the predictions of the NCAR-TGCM for solar maximum and solar minimum conditions, respectively. The two inner traces show the measurements obtained by combining different pairs of line-of-sight observations. The basic diurnal rotation of the vector with UT is observed as the winds flow away from the sunward direction. From reference [100].

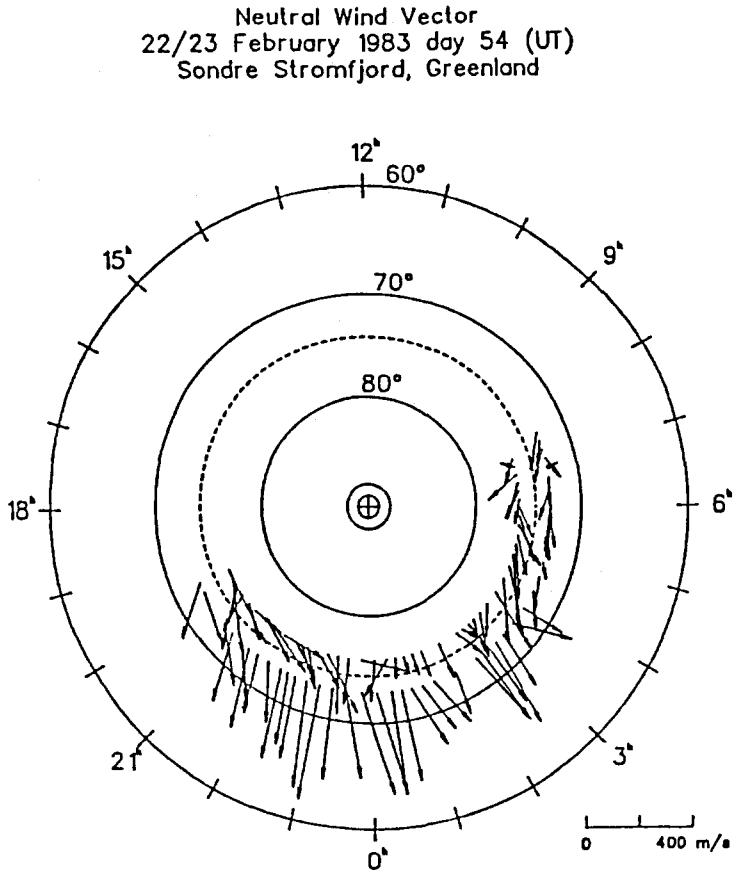

FIGURE 8. Neutral wind vectors observed from Sondre Stromfjord, Greenland. Two sets of vector winds are plotted from observations to the north and to the south of the observing site. The lessening in the neutral wind was observed near 1-2 hours Local Time. From reference [102].

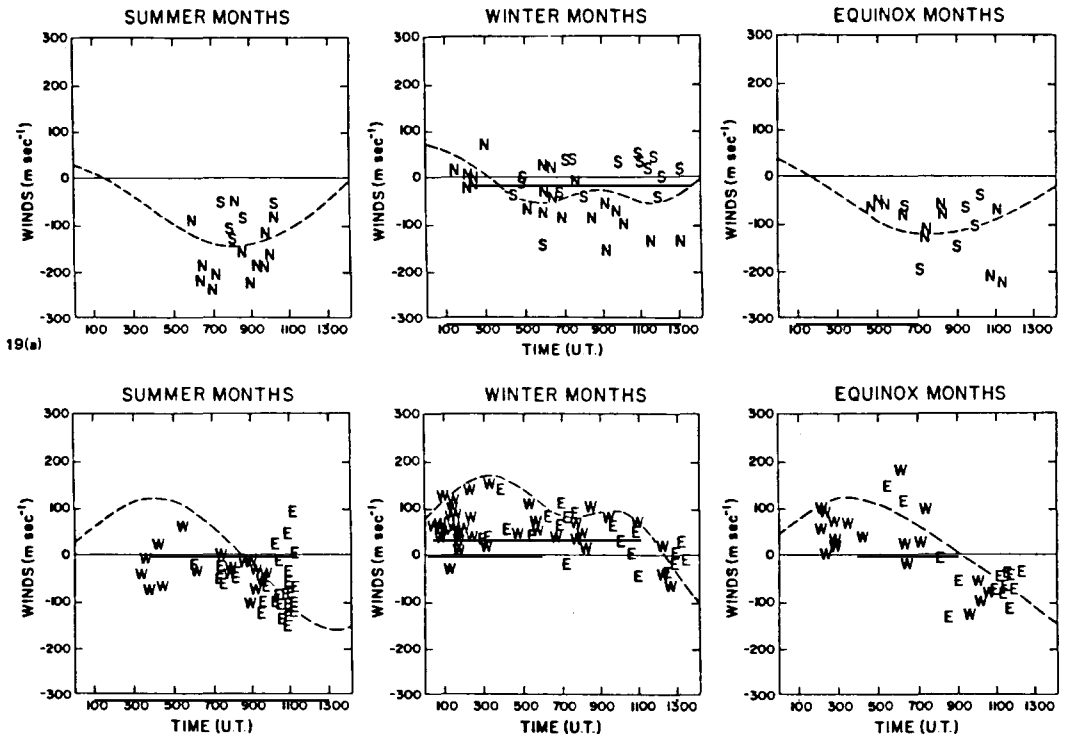

FIGURE 9. Experimental and model winds as a function of local time during summer, winter and equinox months for a mid-latitude station. The letter indicates the direction of observation, while the dashed curve is the calculated wind component from a thermospheric model. From reference [117].

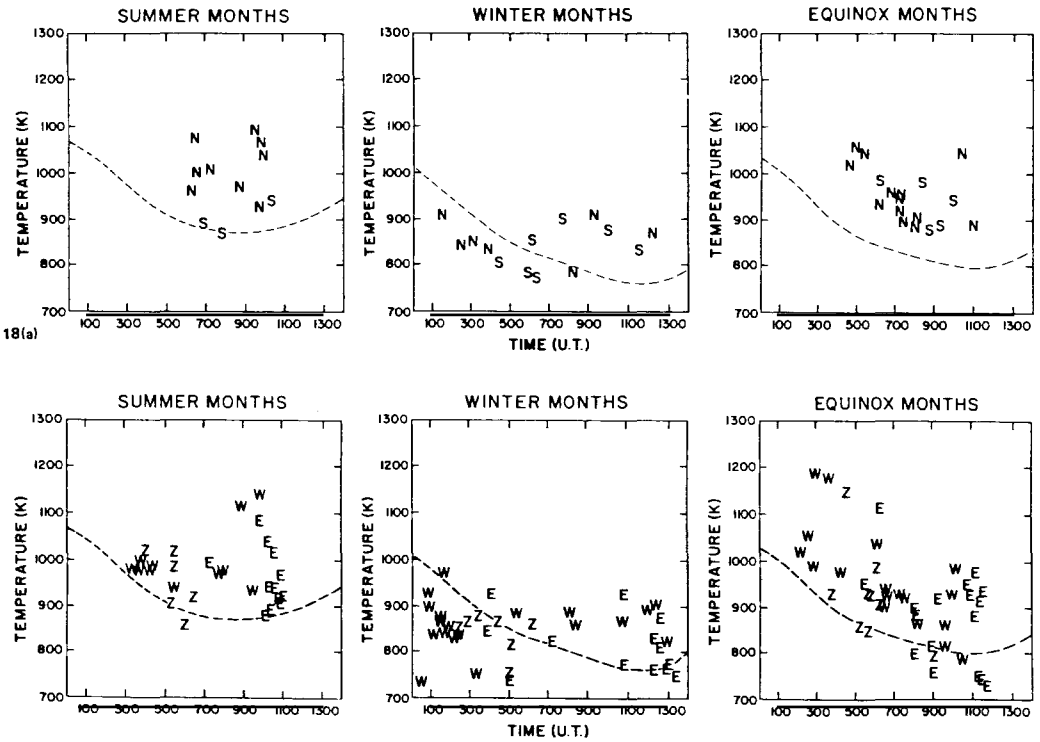

FIGURE 10. Experimental and model temperatures as a function of local time during summer, winter and equinox months. Same conditions as Figure 9. From reference [117].

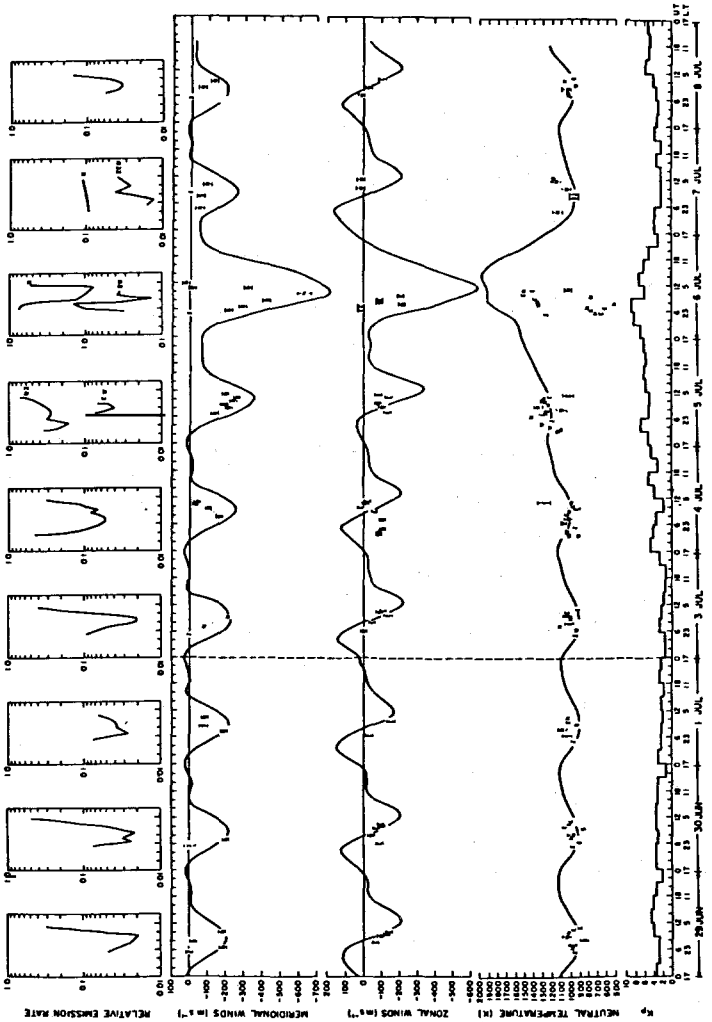

FIGURE 11. Measured and calculated values of the thermospheric neutral temperature and winds during the 29 June-8 July, 1974 geomagnetic storm. The relative emission rate of the 15867K line and the geomagnetic index K_p are shown in the top and bottom frames respectively. The letters indicate the direction of observation for the experimental measurements, while the solid lines are the modelled quantities. From reference [118]

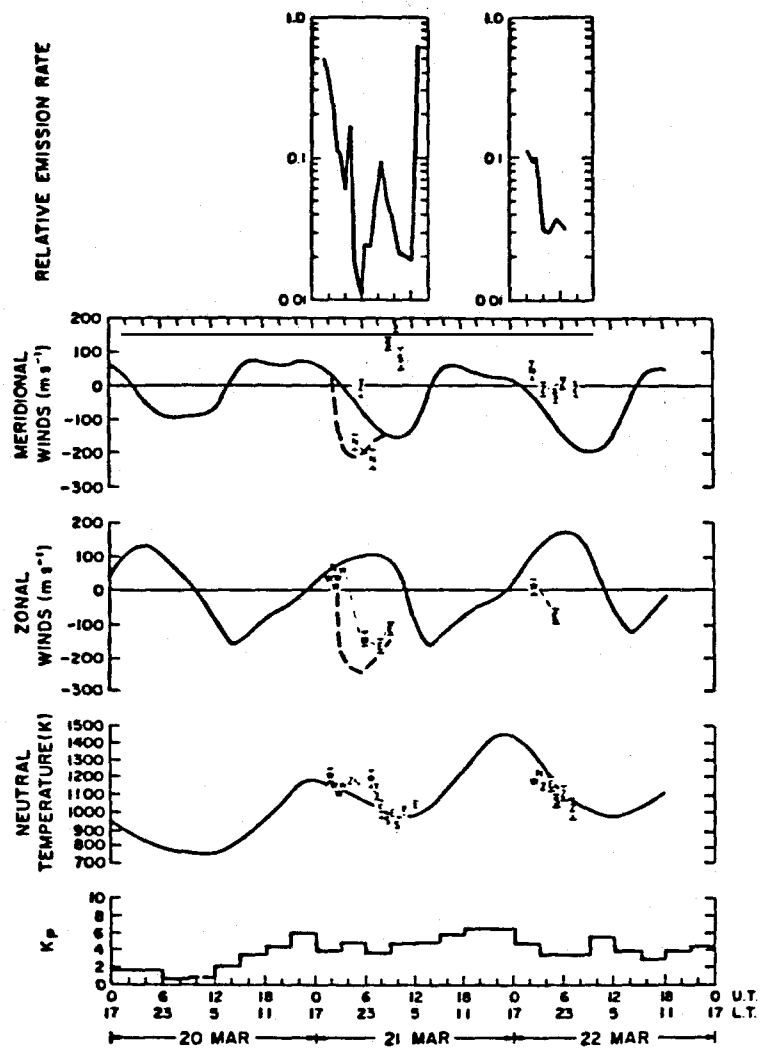

FIGURE 12. Same as Figure 11., except for the 21-22 March, 1974 storm. Note the departure of the zonal winds from the predictions. From reference [118].

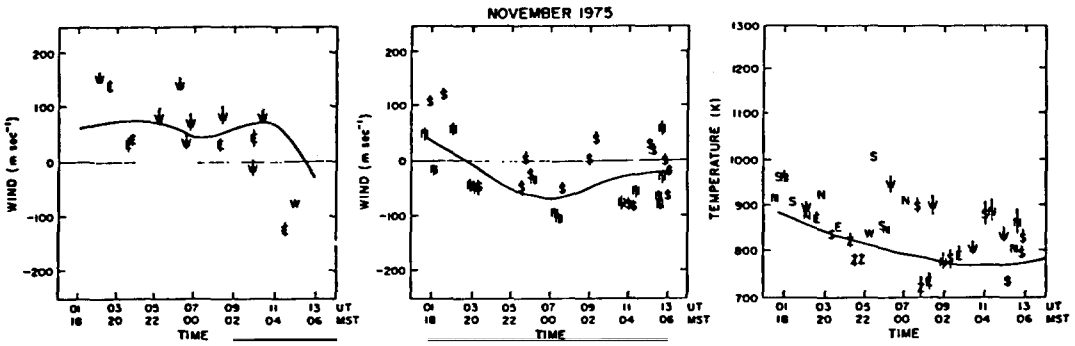

FIGURE 13. Measured and calculated nighttime winds at 40° N, 105.5° W during the November 1975 observing. Positive southward and eastward motion convention used. From reference [121].

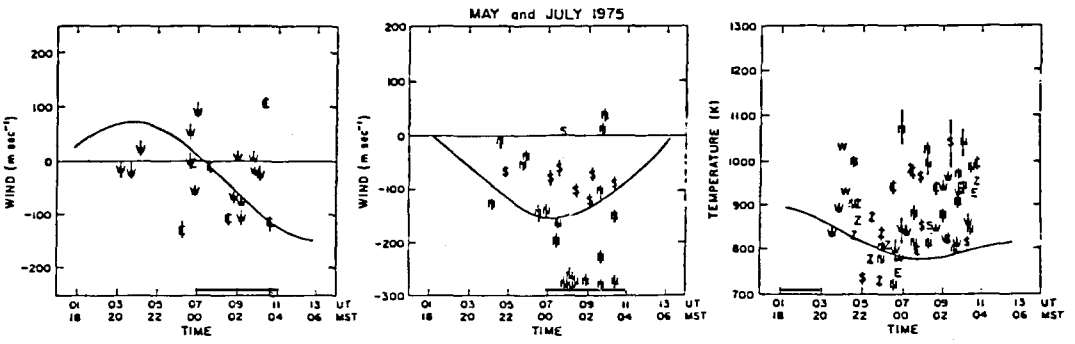

FIGURE 14. Same as Figure 13, except for the combined months of May and July, 1975. From reference [121].

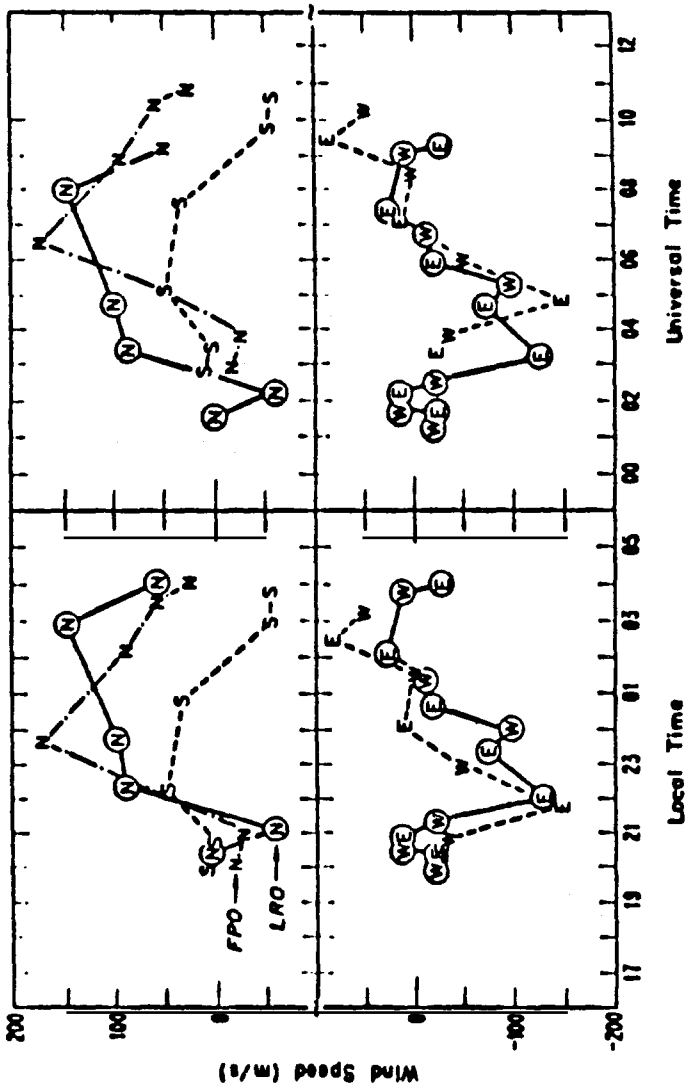

FIGURE 15. Simultaneous measurements of neutral winds at 40° N, 105° W and 40° N, 79° W. The measurements are given as a function of local time (left) and universal time (right). The convention of positive motion southward and eastward is used here. From reference [127].

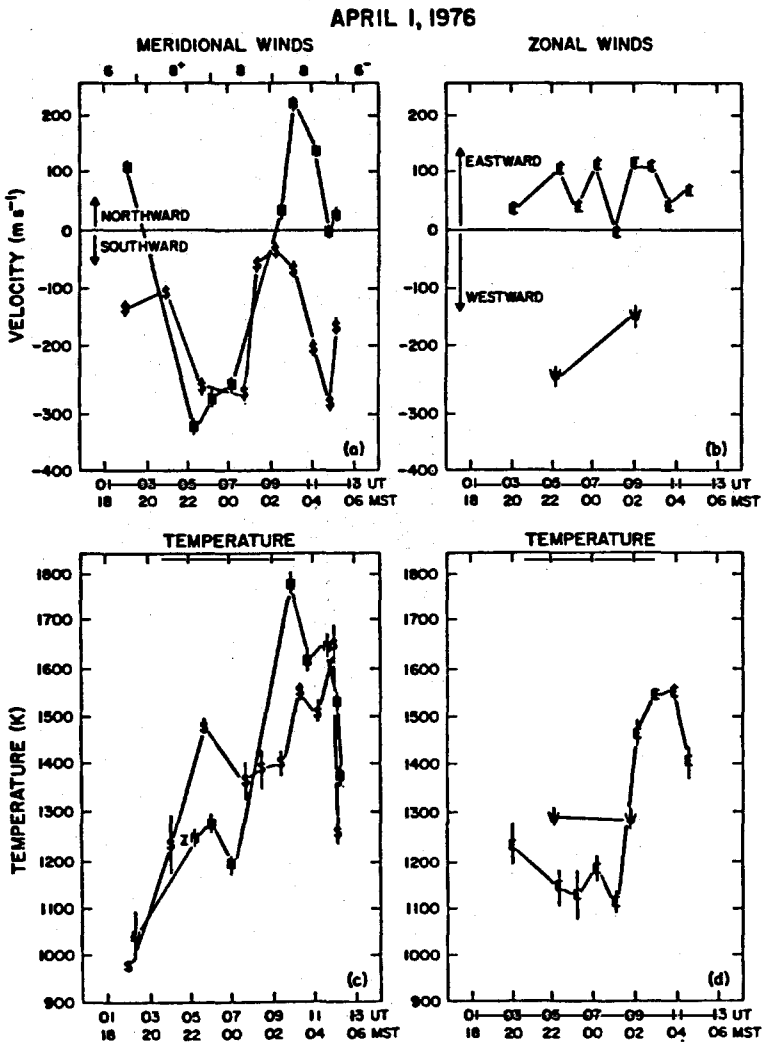

FIGURE 16. Wind and temperature behaviour of the upper thermosphere during the April 1, 1976 geomagnetic storm. This behaviour is typical of solar minimum conditions. From reference [128]

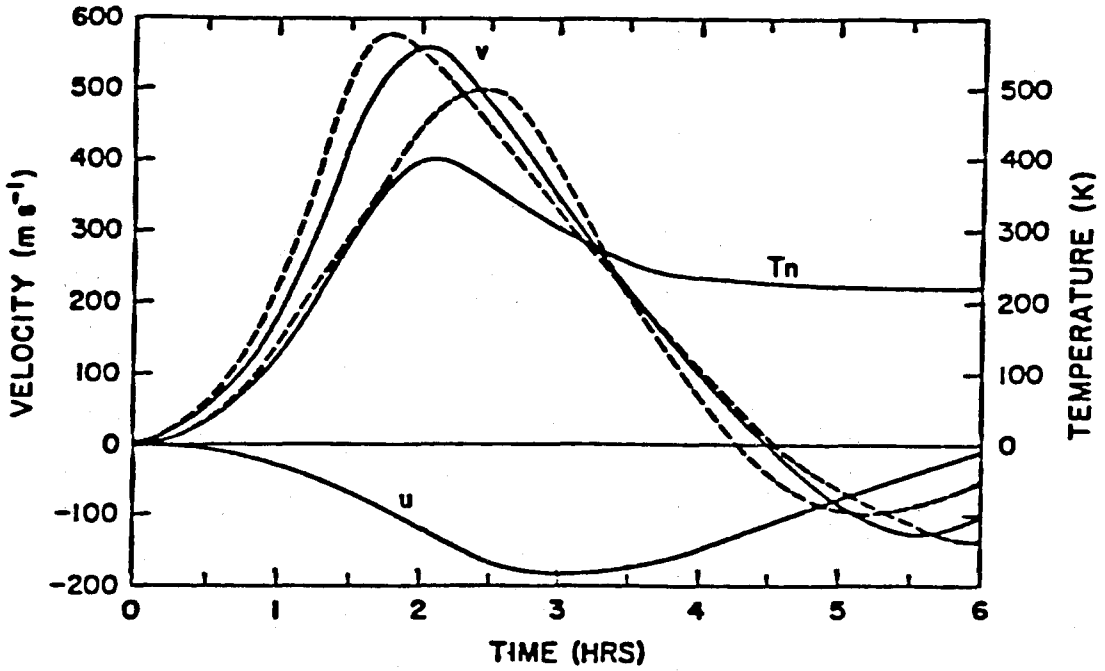

FIGURE 17. Calculated equatorward wind and temperature at a midlatitude station due to the passage of a thermospheric wave. The solid line indicates the wind and temperature at the station zenith, while the dashed line curves are the winds at 6° latitude north and south of the station. This simulation is comparable with the results given in Figure 10. Positive southward convention for the winds is used here. From reference [128].

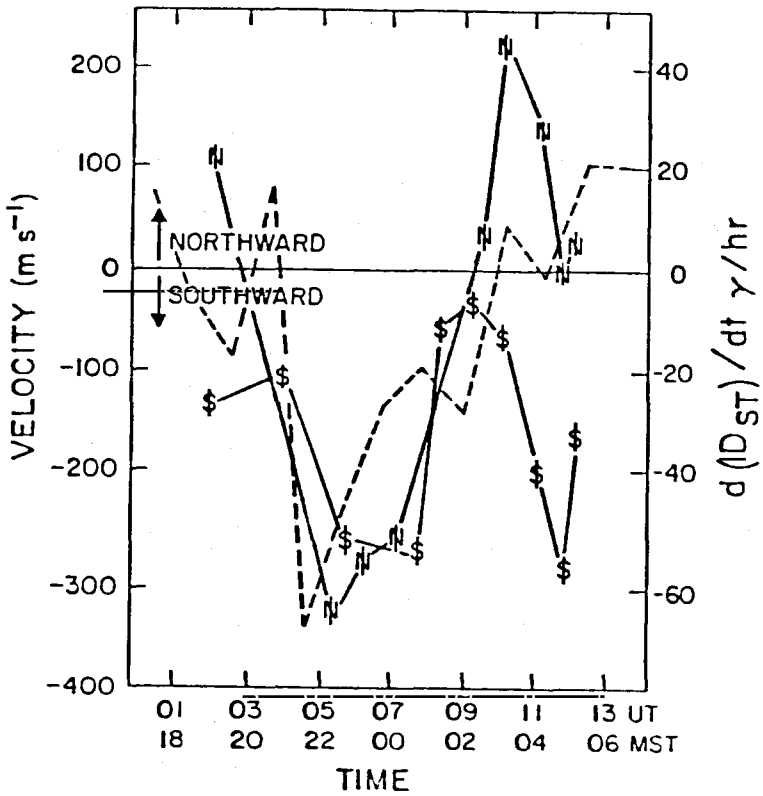

FIGURE 18. Same as Figure 16, except the rate of change of D_{st} is shown as a dashed line, illustrating the apparent correlation between the motions and D_{st}. From reference [131].

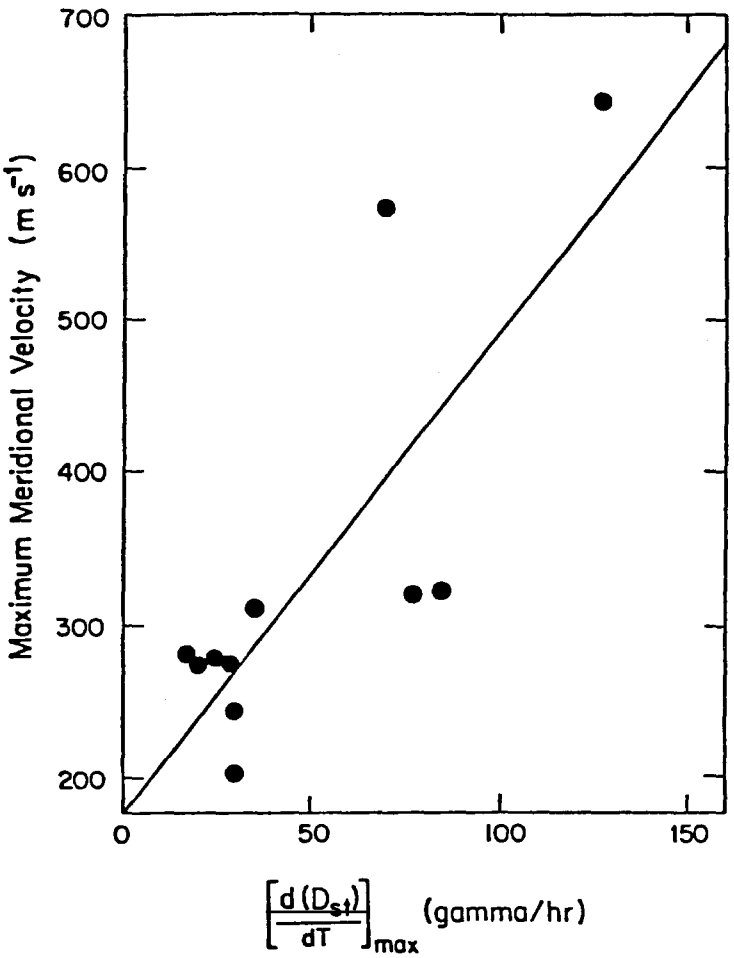

FIGURE 19. Relationship between the measured meridional wind for various geomagnetic storms and the maximum value of the time rate of change of D_{st}. Positive southward wind convention used here. From reference [131].

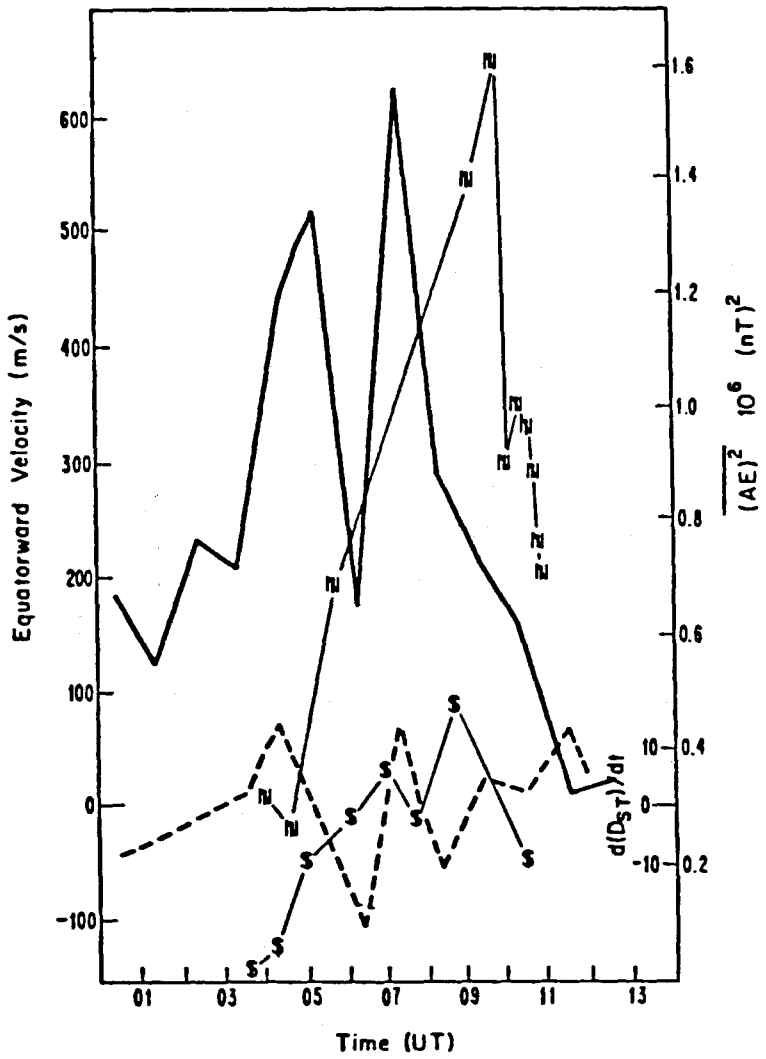

FIGURE 20. Meridional winds for the storm of July 5, 1978 (letters). The solid line is a plot of $(AE)^2$ index and the dashed line is the time rate of change of D_{st}. From reference [133].

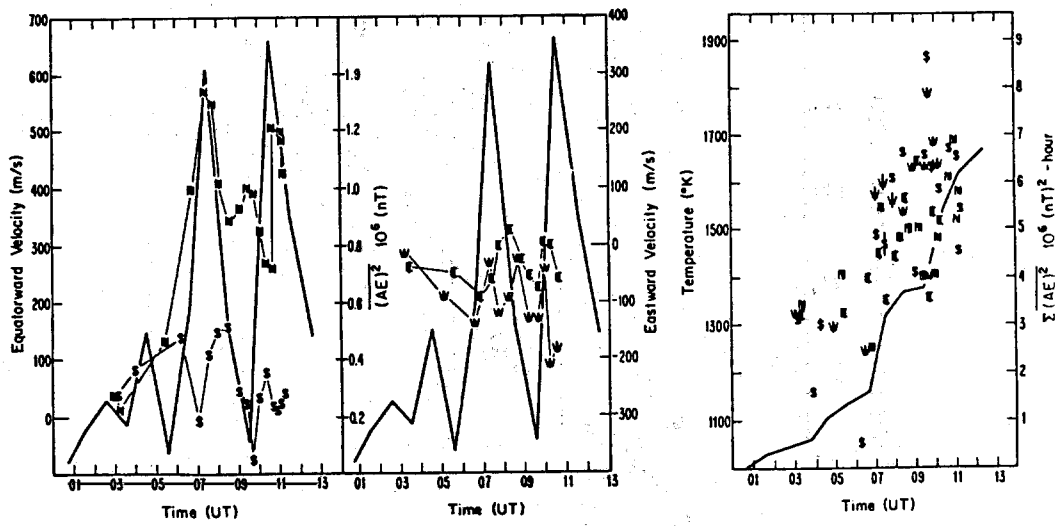

FIGURE 21. Nighttime measurements of the meridional and zonal winds as well as the kinetic temperature as a function of time for the geomagnetic storm of May 9, 1978. The solid heavy line is a graph of the $(AE)^2$ index (Σ $(AE)^2$ for the temperature). Positive southward convention for the meridional wind is used. From reference [133].

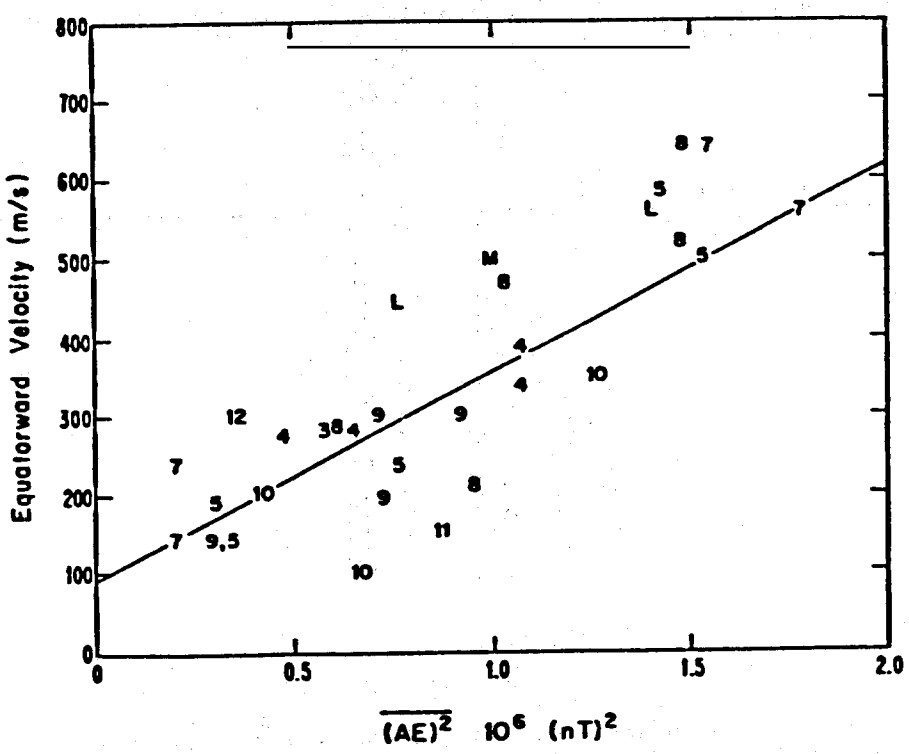

FIGURE 22. Peak equatorward meridional wind as a function of the peak value of the $(AE)^2$ index for the evening. The number symbols indicate the month when the observations were made, while the letters indicate other midlatitude stations measurements. From reference [133].

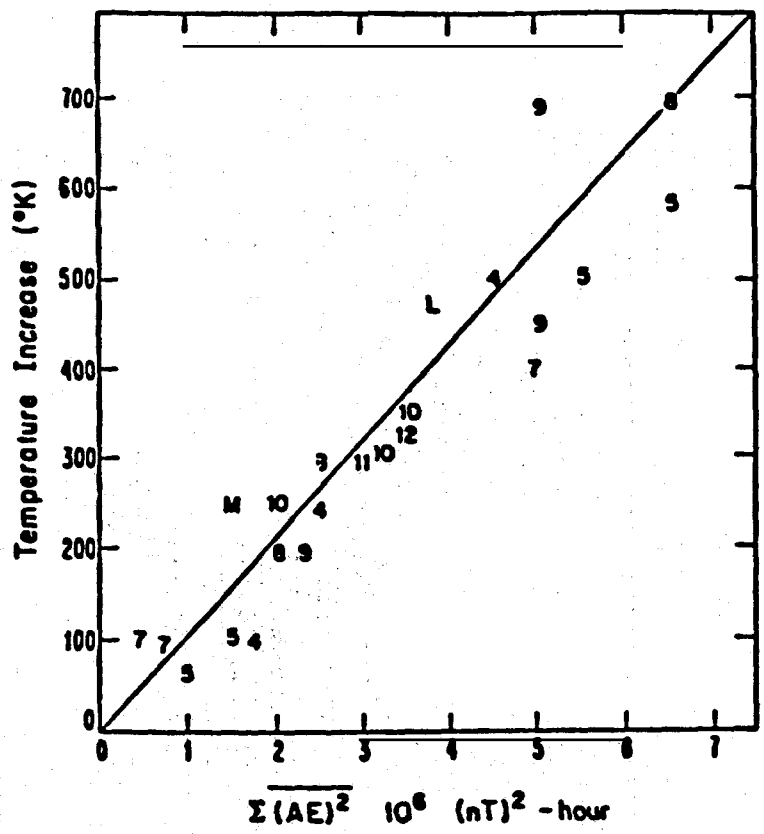

FIGURE 23. Neutral gas kinetic temperature increase as a function of the summation of $(AE)^2$. From reference [133].

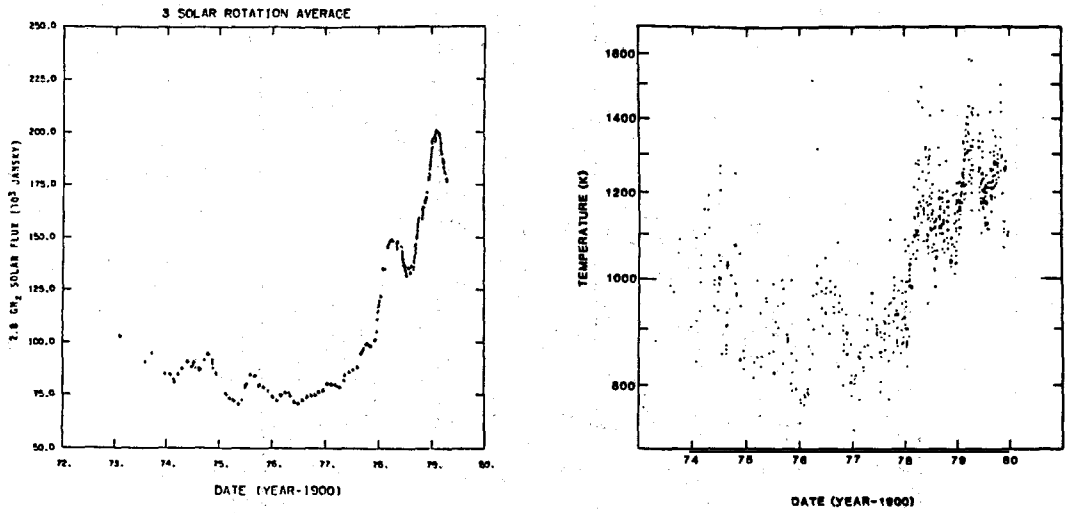

FIGURE 24. a) 2.8 GHz solar flux (three solar rotation averages) and b) daily neutral temperatures measured at Fritz Peak Observatory (39.9° N, 105.5° W), for the 1973 to 1980 period. From reference [138].

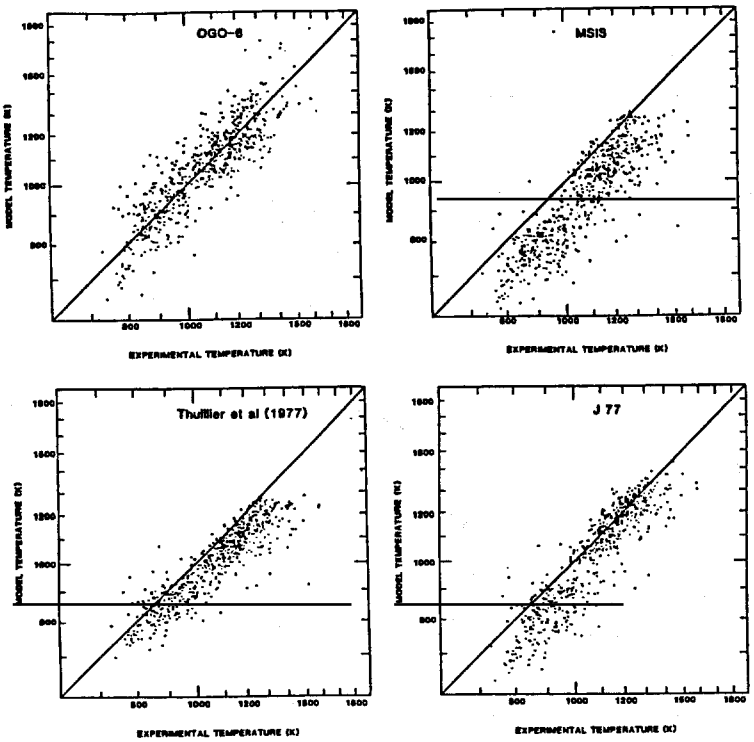

FIGURE 25. Comparison of the data of Figure 24 with semi-empirical temperature models, as indicated. From reference [138].

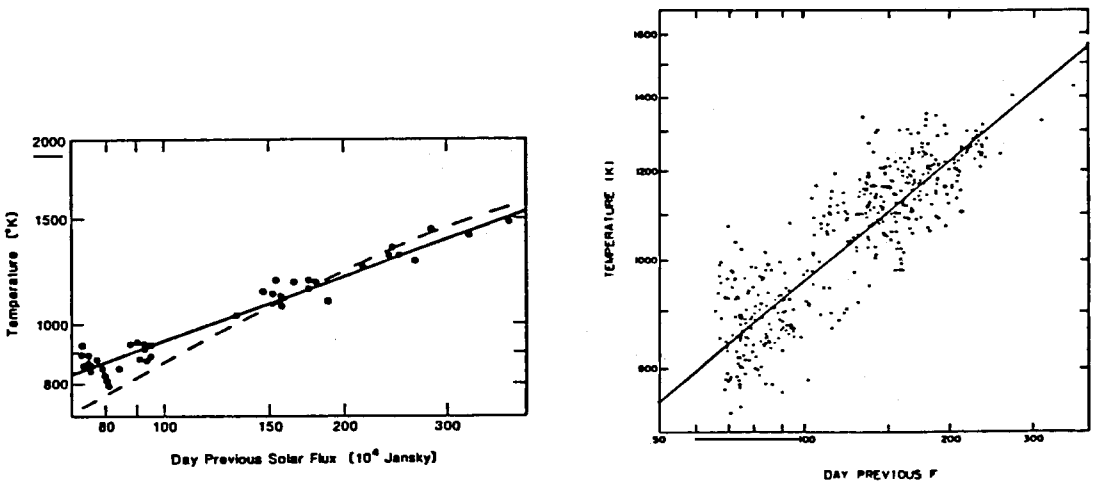

FIGURE 26. Dependence of the observed neutral temperature as a function of solar activity (expressed as the 2.8 GHz flux) for a) data from the months of November and b) quiet-time data. Both graphs refer to the 1973-1980 period. From reference [138].

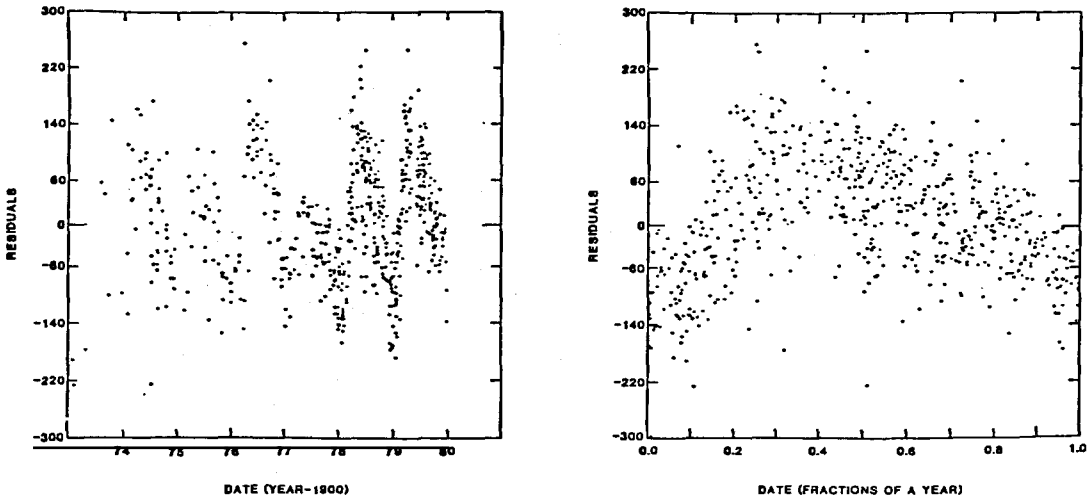

FIGURE 27. Residuals of the experimental temperature data of Figure 24, after the solar and geomagnetic activity dependence have been removed. The right panel is a superposed epoch plot of the left side. From reference [138].

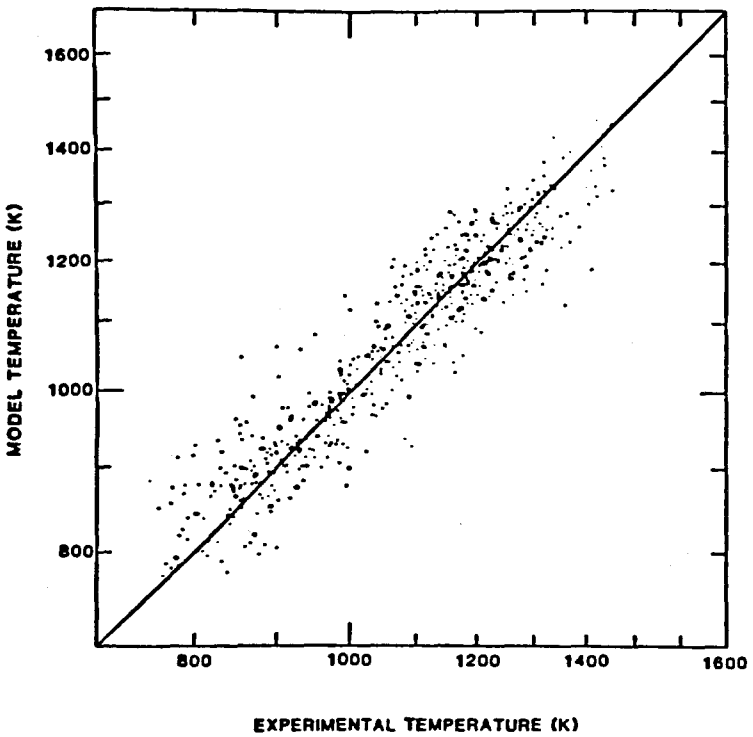

FIGURE 28. Fit of the experimental temperature data to a 4-parameter expression involving solar flux, magnetic activity, solar declination angle and a semi-annual variation. From reference [138].

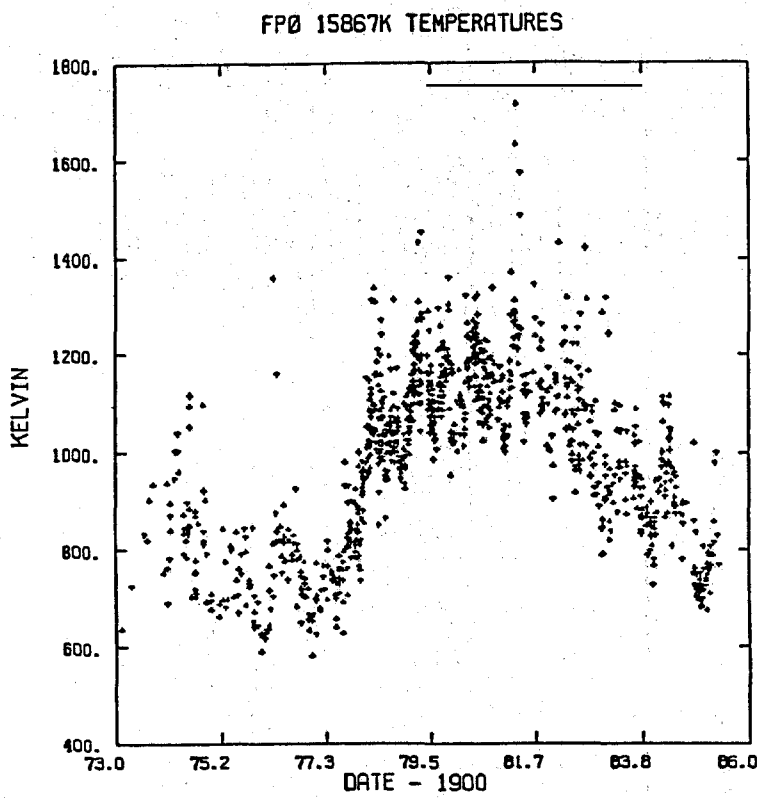

FIGURE 29. Neutral kinetic temperatures measured at Fritz Peak Observatory from 1973 to 1986.

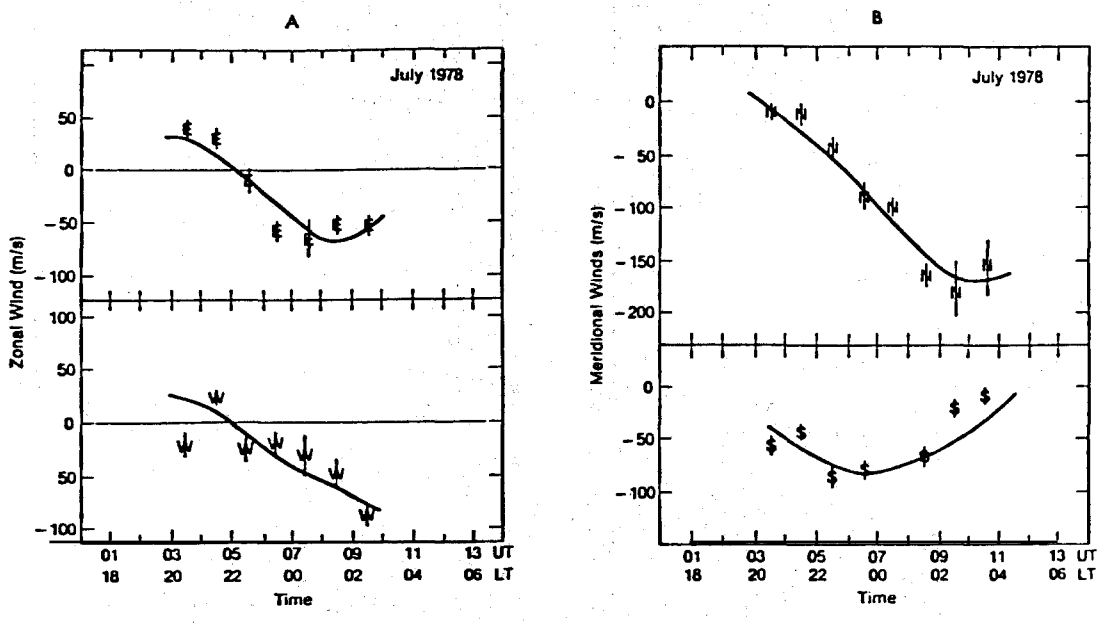

FIGURE 30. Monthly average thermospheric winds during July, 1978. The solid line is the smooth profile used to construct the contours of Figs. 31 and 32. From reference [148].

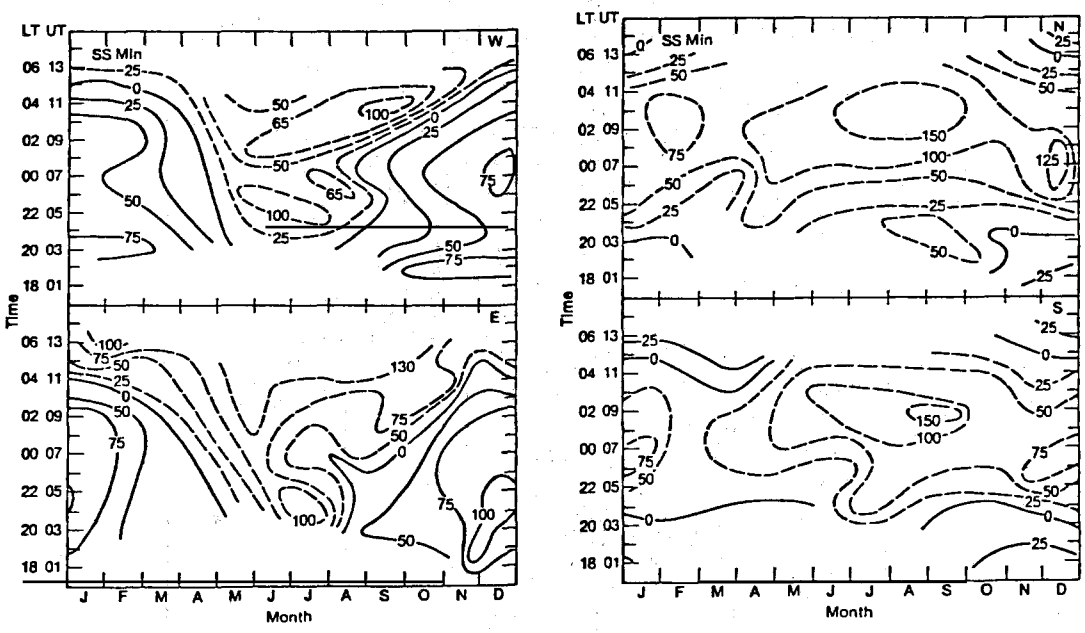

FIGURE 31. Contours showing the monthly variation of the average nighttime wind in the four cardinal directions. Solid line contours indicate northwards and eastwards winds. Solar minimum conditions. From reference [148].

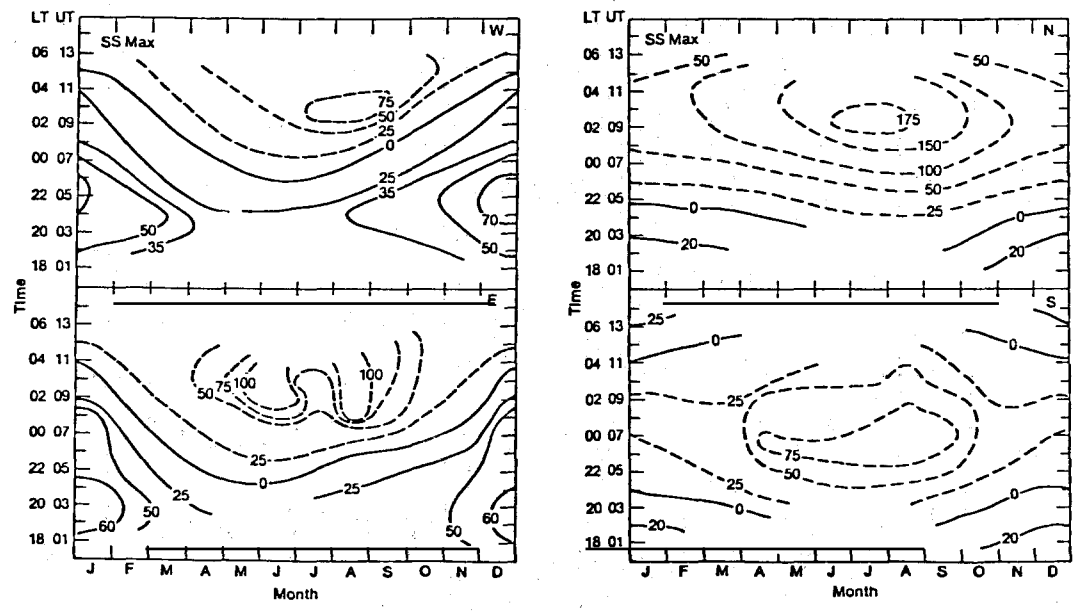

FIGURE 32. Contours showing the monthly variation of the average nighttime wind in the four cardinal directions. Solid line contours indicate northwards and eastwards winds. Solar maximum conditions. From reference [148].

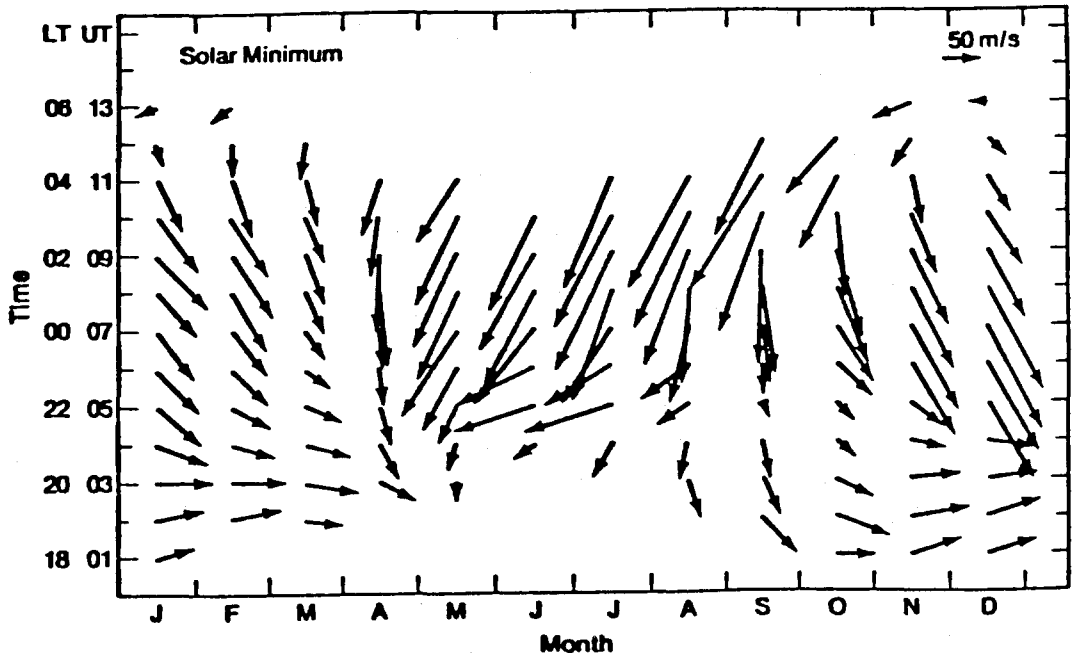

FIGURE 33. Vector winds for solar minimum conditions. North direction is upwards. From reference [148].

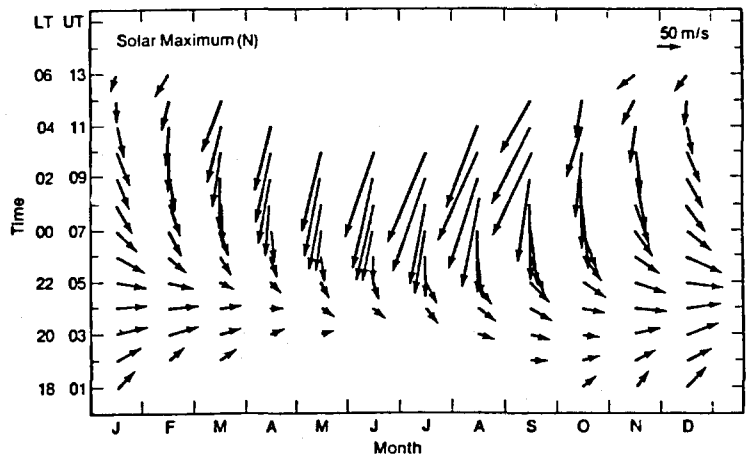

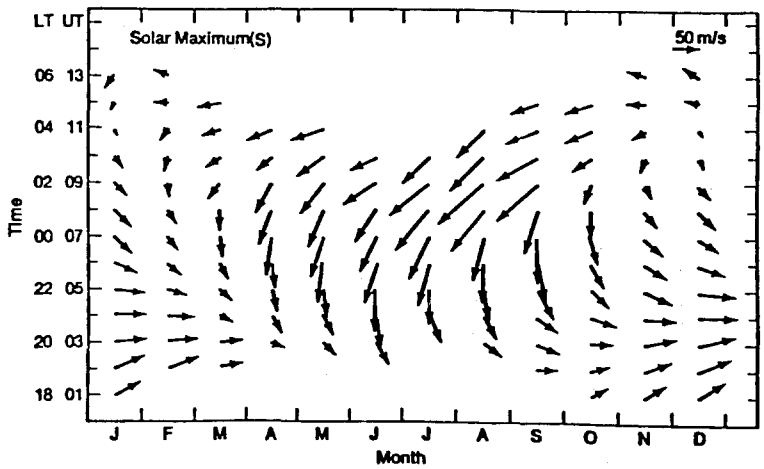

FIGURE 34. Vector winds for solar maximum conditions. North direction is upwards. From reference [148].

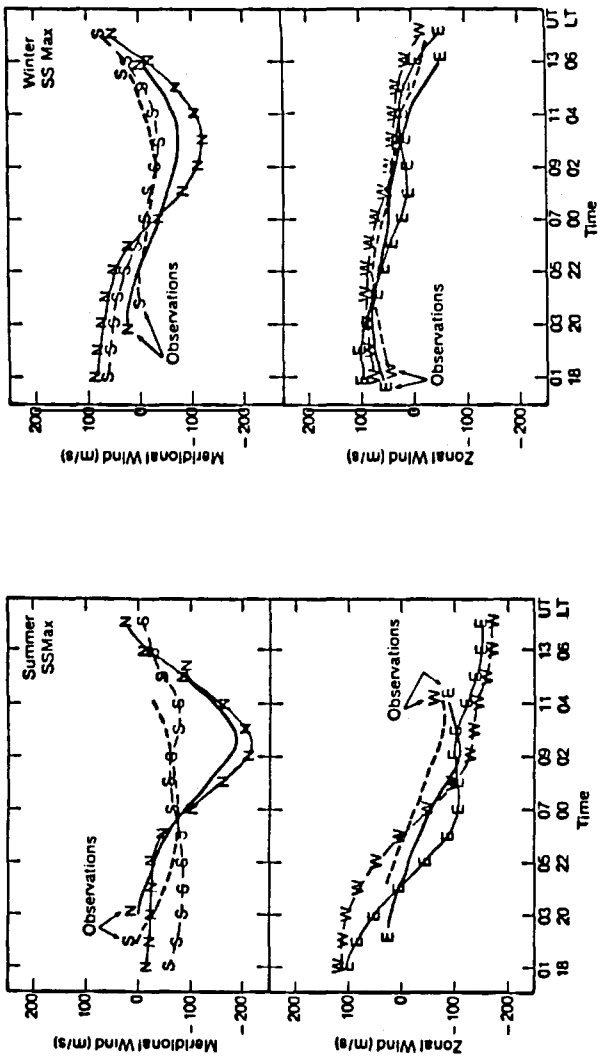

FIGURE 35. Observed and calculated thermospheric winds during solar maximum for summer and winter conditions. The observations are denoted by the unmarked solid and dashed lines. From reference [148].

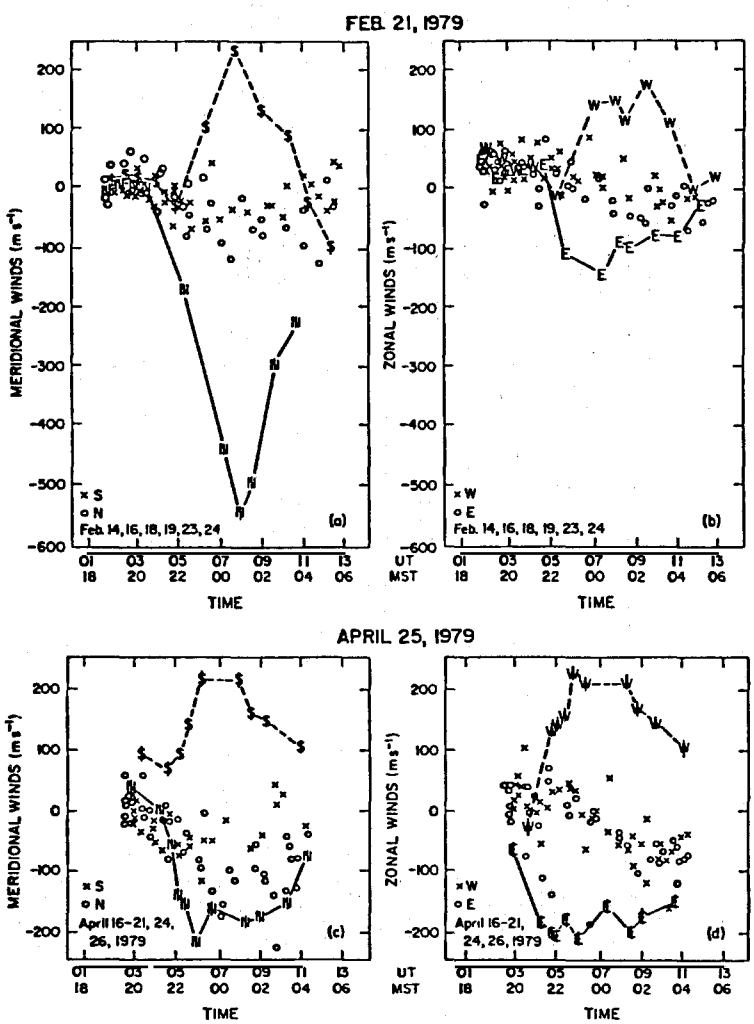

FIGURE 36. Thermospheric behaviour for two geomagnetic storms near solar maximum activity. The circles and crosses indicate geomagnetically quiet days measured near the date of the storms. These dates are indicated in the figure. From reference [148].

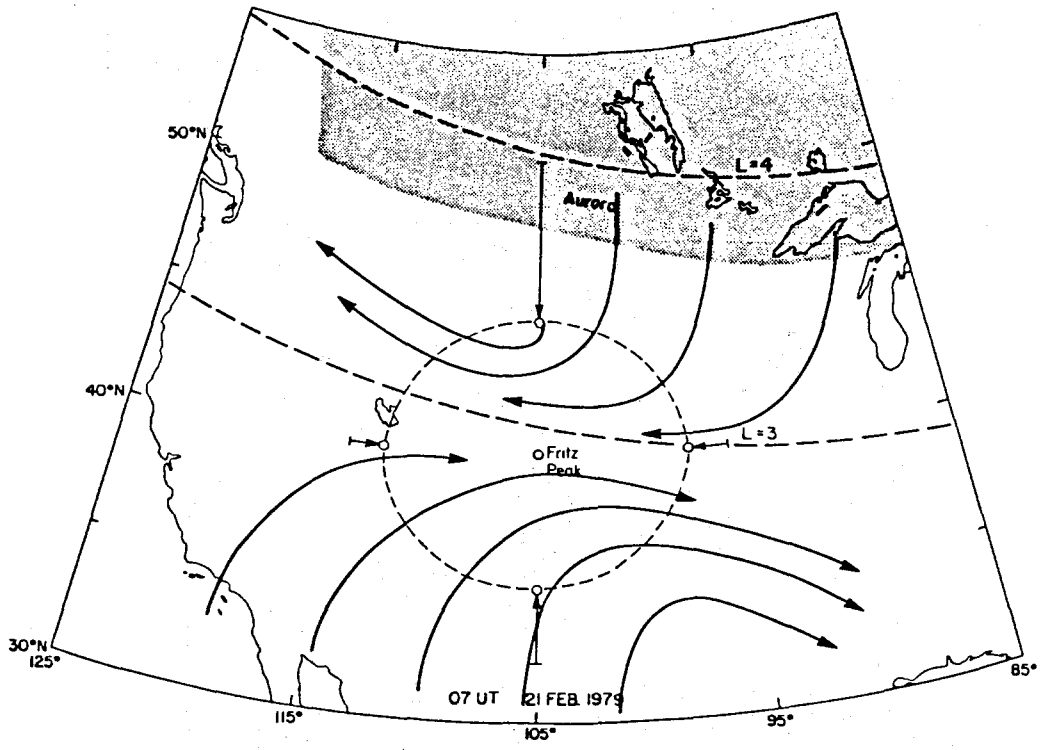

FIGURE 37. Schematic flow pattern for the February 21 and April 25, 1979 storms. From reference [150].

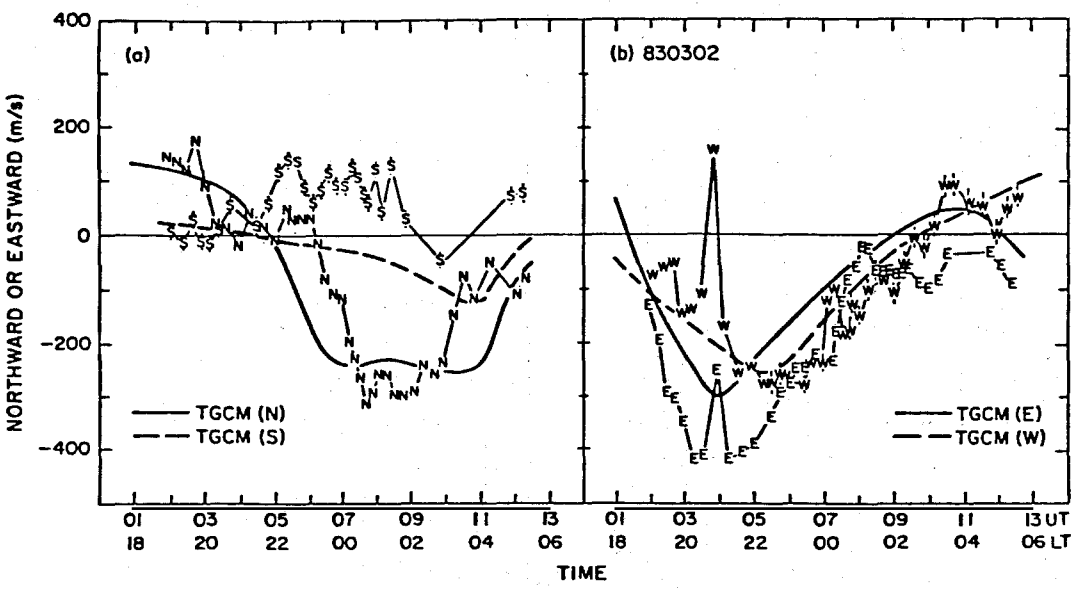

FIGURE 38. Thermospheric circulation behaviour measured during the March 2, 1983 geomagnetic storm. The solid and dashed lines indicate the model simulation. From reference [154].

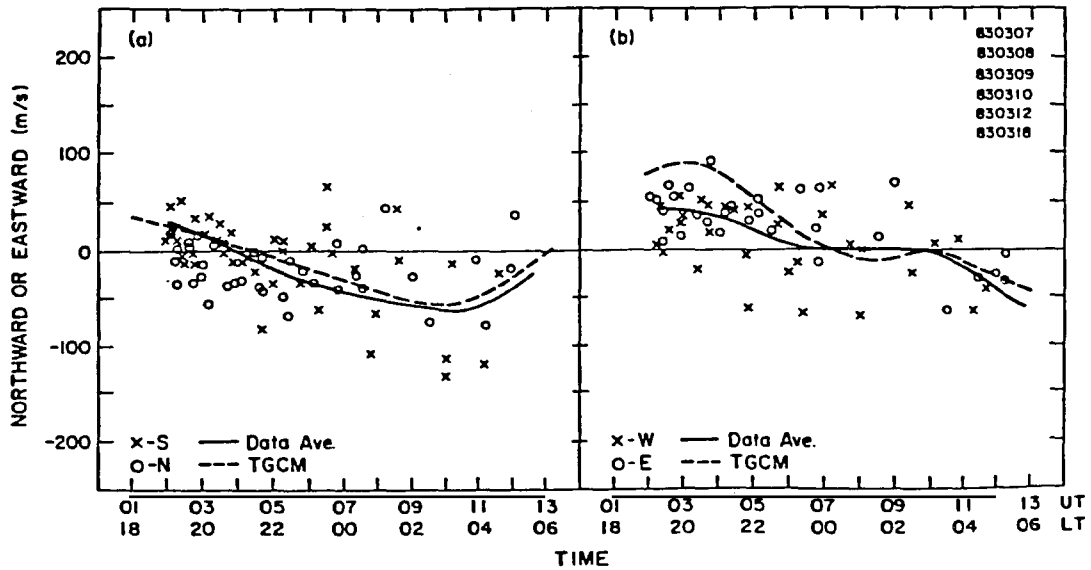

FIGURE 39. Observed thermospheric circulation during geomagnetically quiet times during the month of March, 1983. The dates of measurement are given in the right side corner of the figure. The solid lines are a smooth average of the data points, while the dashed lines are the model predictions. From reference [154].

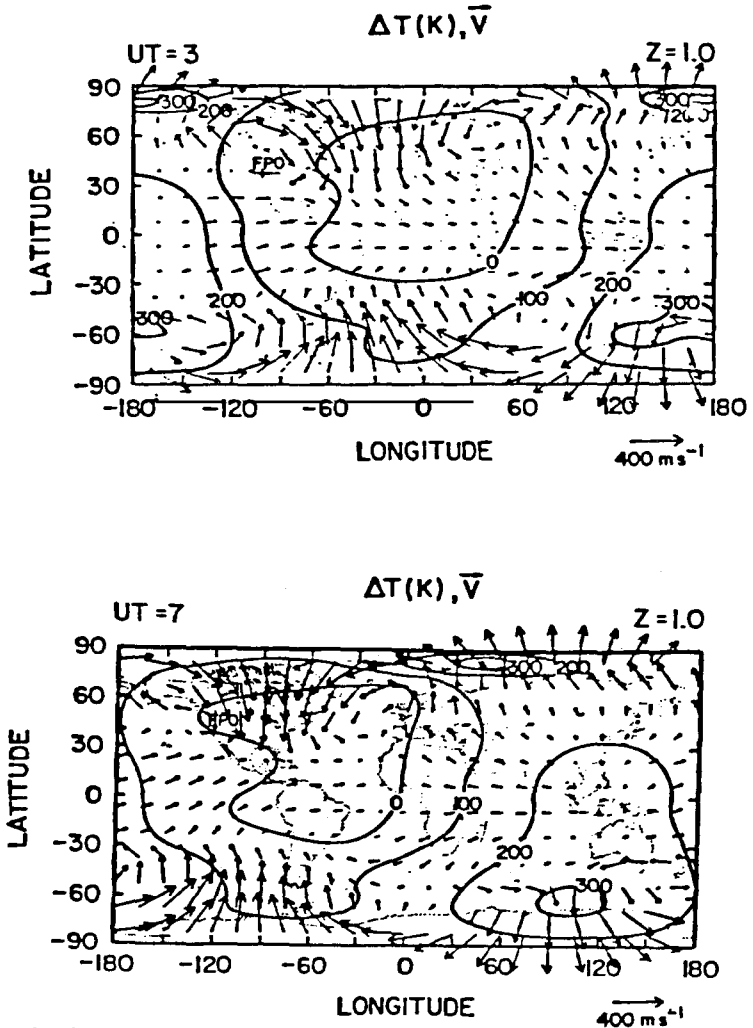

FIGURE 40. Detailed NCAR-TGCM simulations of the March 2, 1983 storms for the 0300 UT and 0700 UT time periods. From reference [154].

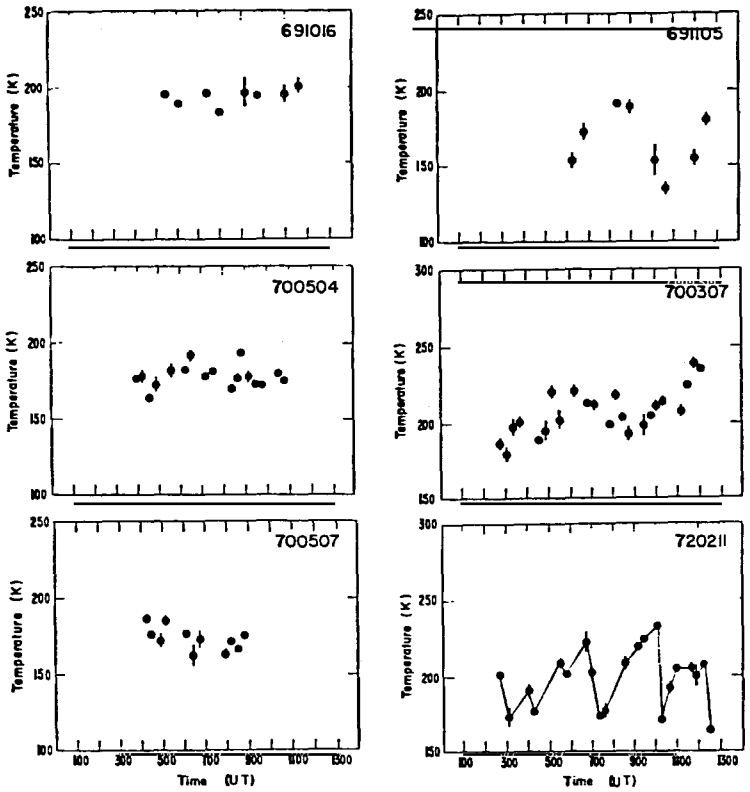

FIGURE 41. Diurnal variation of the kinetic temperature of the lower thermosphere, measured at the zenith from Fritz Peak Observatory for individual days. From reference [165].

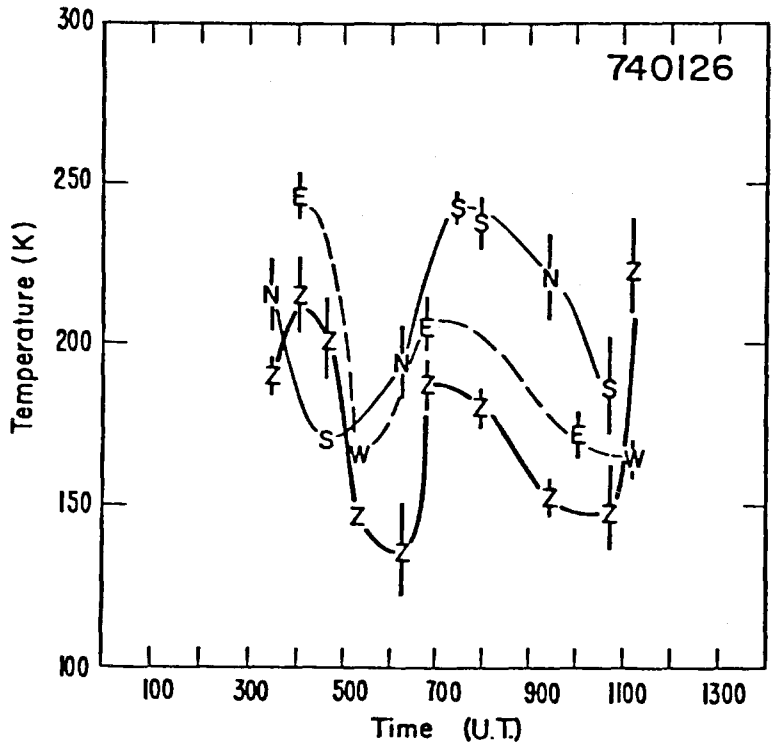

FIGURE 42. Diurnal variation of the kinetic temperature at the indicated directions (N, E, S, W, and Zenith) from Fritz Peak Observatory for individual days. From reference [165].

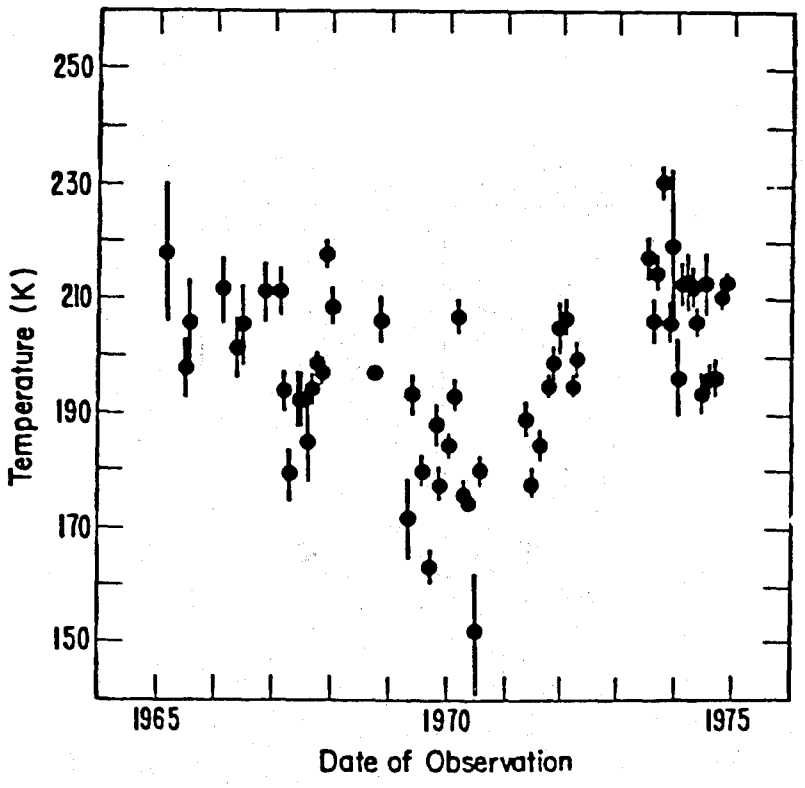

FIGURE 43. Summary of the temperature measurements expressed as observing period averages. The statistically estimated errors of the mean are indicated. From reference [165].

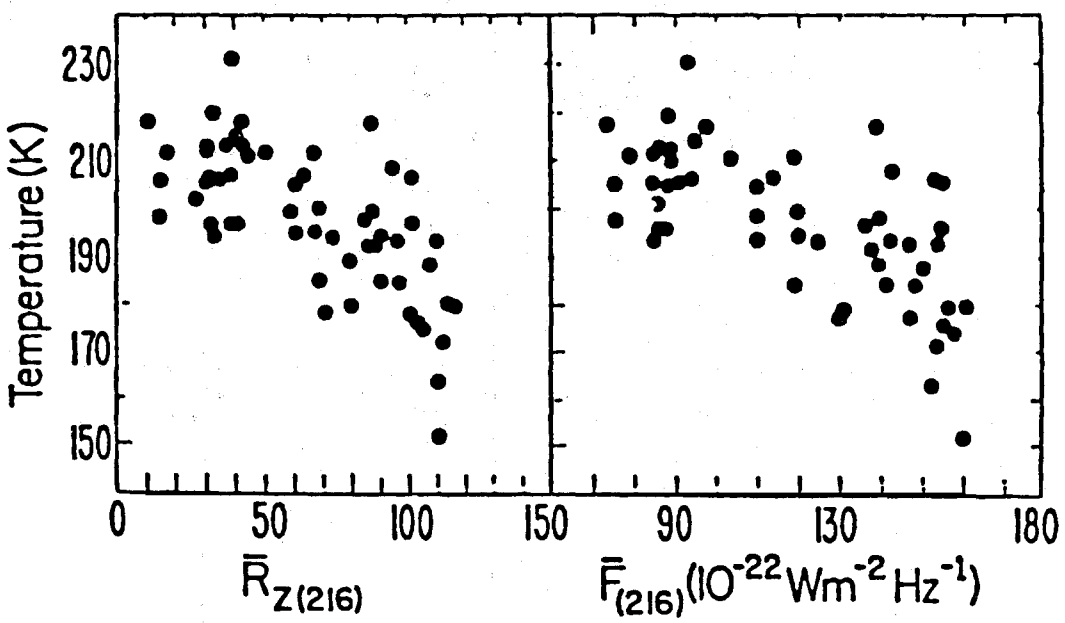

FIGURE 44. Relationship between the determined temperatures and solar activity, with the latter expressed as the sunspot number, R_z, and the 2.8 GHz radio flux, $F_{10.7}$. Both solar flux measures have been averaged for 216 days. From reference [165].

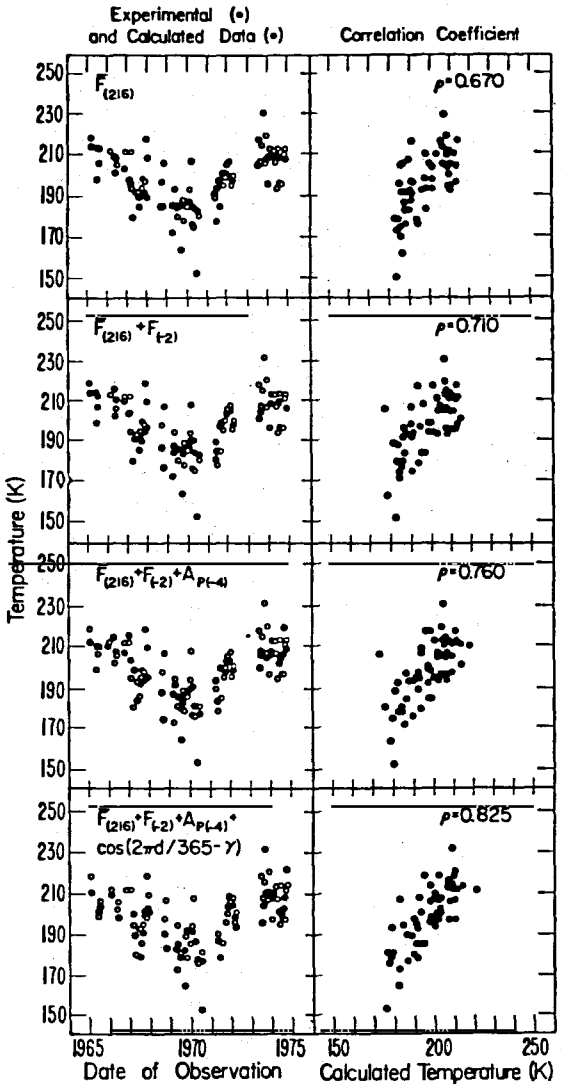

FIGURE 45. Least squares fit of the data with solar activity, magnetic activity and an annual oscillation. The open circles are the measurements and the filled circles are its fit. The right side panel illustrates the goodness of fit. From reference [165].

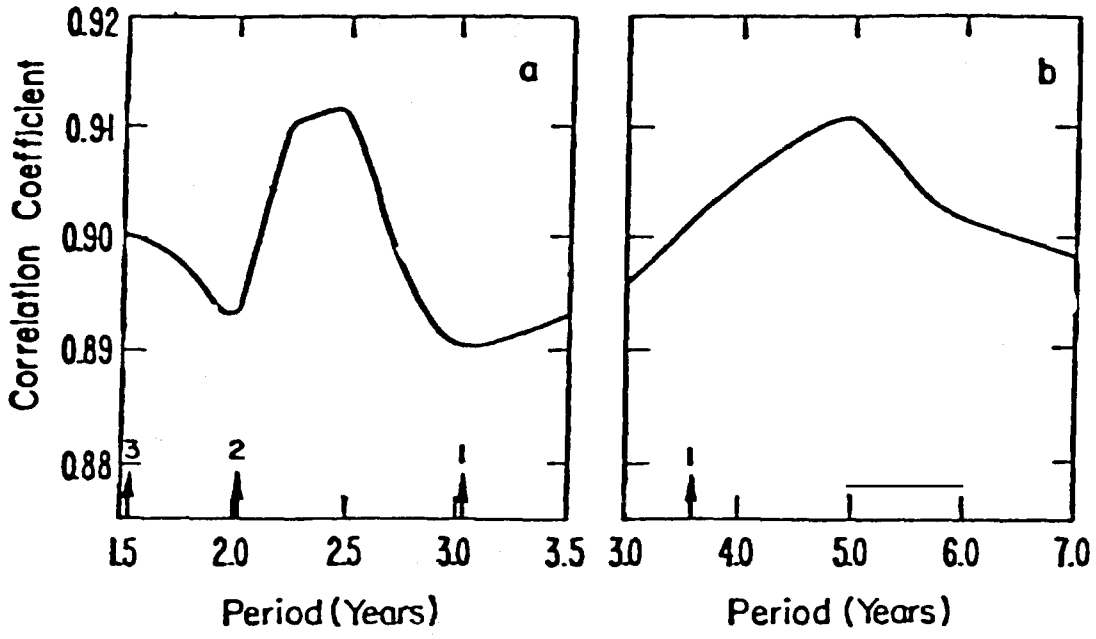

FIGURE 46. Correlation coefficients of the fit as a function of period used to test the validity of the 2.5- and 5-year periodicities. The arrows indicate the location of the harmonics for the (truncated) data employed to determine these periodicities. From reference [165].

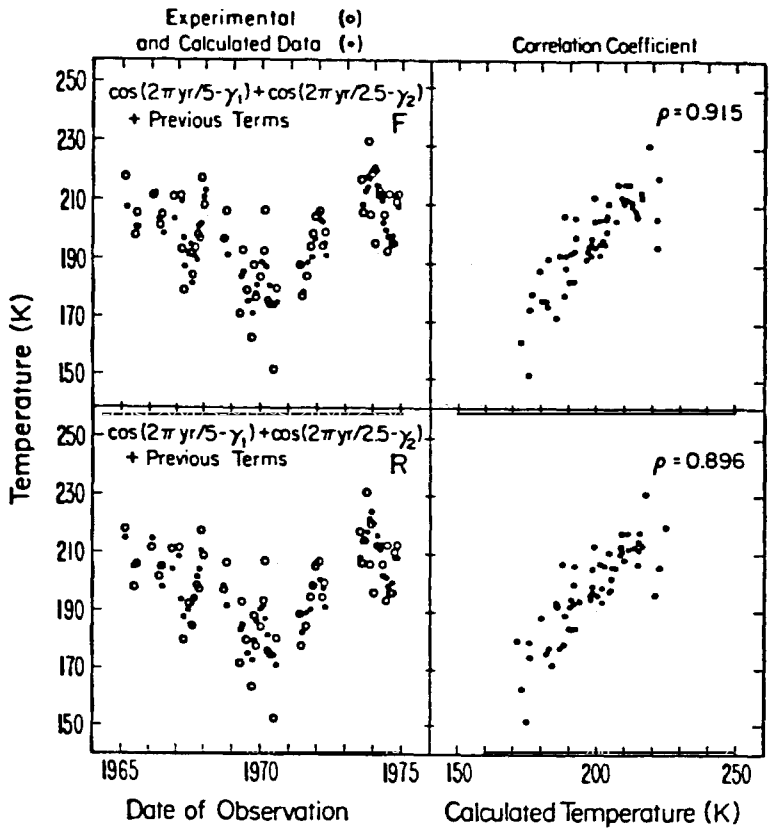

FIGURE 47. Least squares fit of the observed temperature measurements, including the 2.5- and 5-year oscillations. From reference [165].

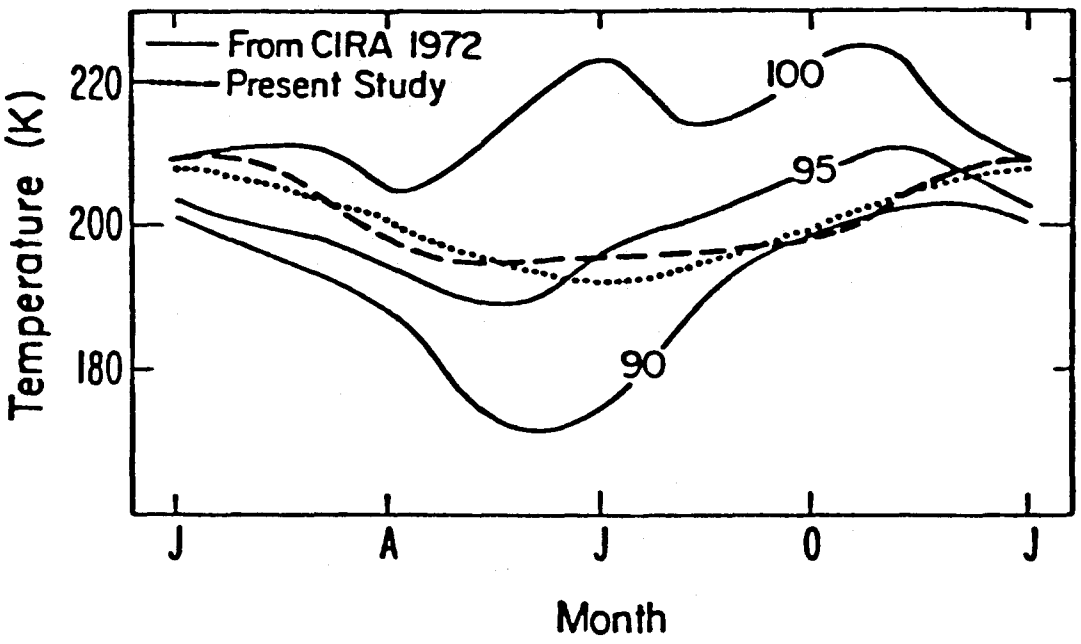

FIGURE 48. Annual (dotted line) and annual and semi-annual (dashed line) variations determined from the optical kinetic temperature compared to the data of [179] weighed by an airglow emission profile. From reference [165].

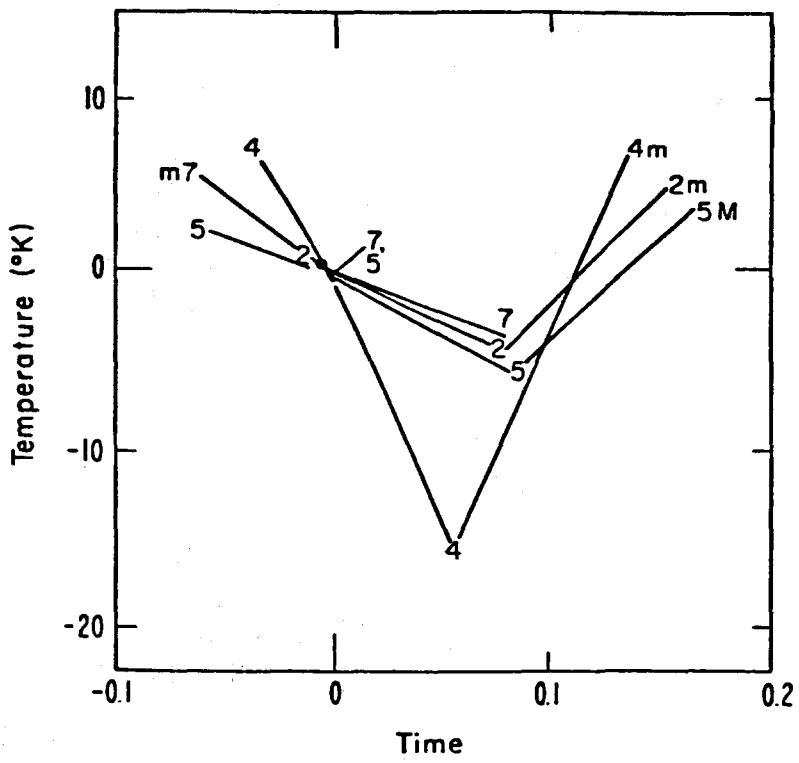

FIGURE 49. Lower thermosphere cooling associated with stratospheric warmings. Zero time and temperature are defined for the date of peak stratospheric warming. The lines indicate warming events occurring during 1967, 1972, 1974 and 1975 and shown in the graph by their last digit. The character of the warming is marked as well; M = major and m = minor. From reference [172].

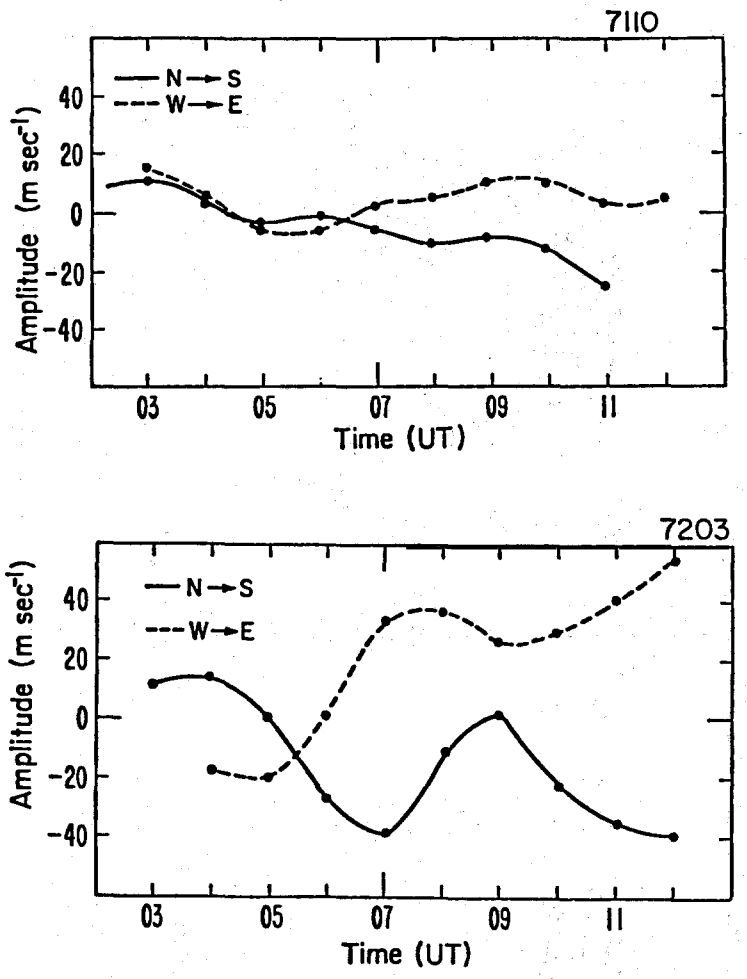

FIGURE 50. Mean daily winds of the lower thermosphere for the months of October 1971 and March 1972, showing the change in the amplitude of the observed winds at midlatitude. From reference [173].

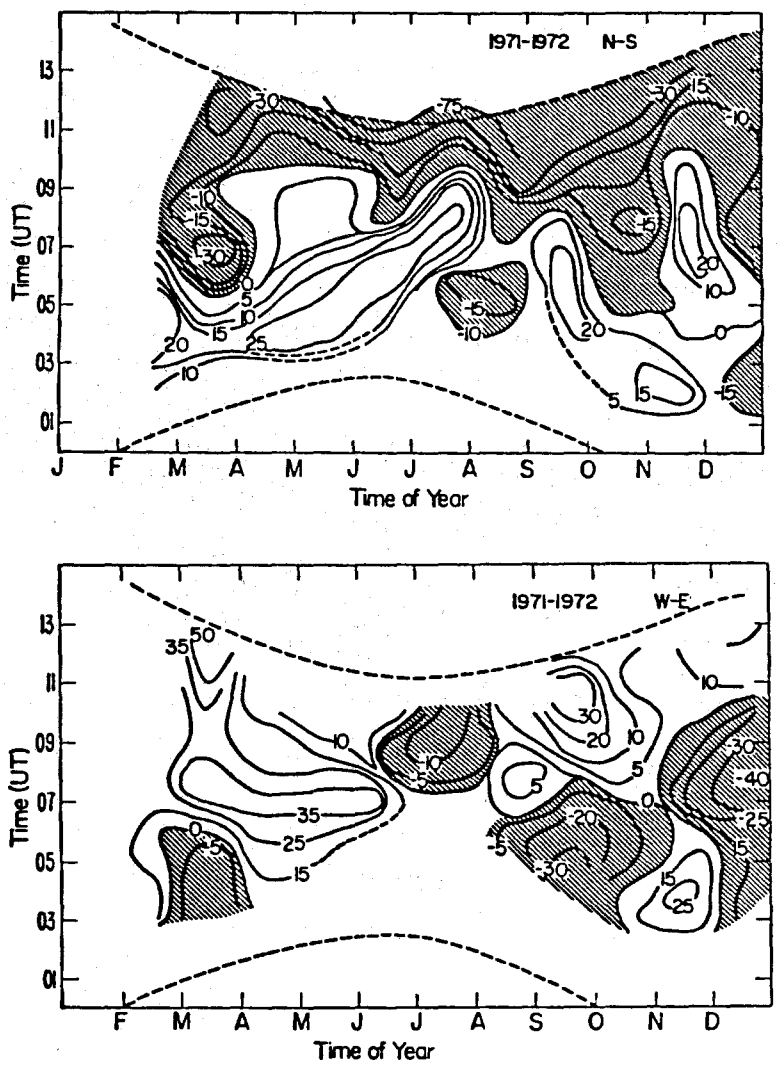

FIGURE 51. Contour maps of the measured wind at 40° N for the 1971-1972 period. The hashed areas indicate westward and northward wind motions, while the dashed lines show the limits of observation, given by twilight. From reference [173].

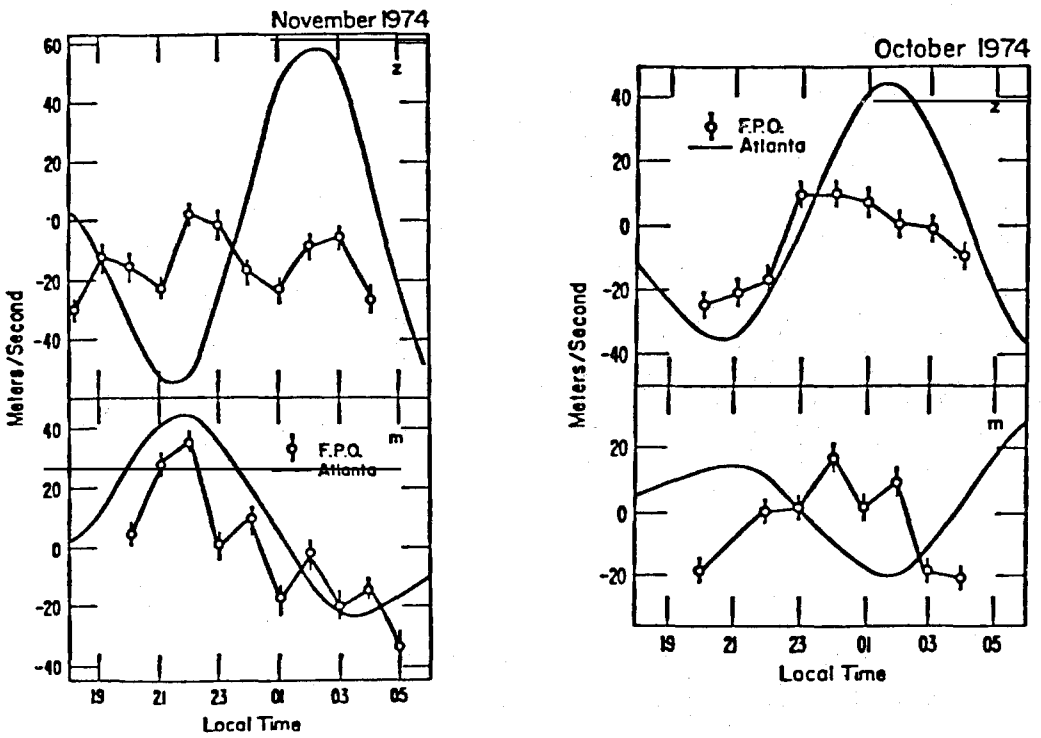

FIGURE 52. Comparison of lower thermosphere winds as measured by optical (solid) and meteor radar (open circles). The meteor radar winds have been weighed by an airglow emission profile to make the comparison meaningful. From reference [175].

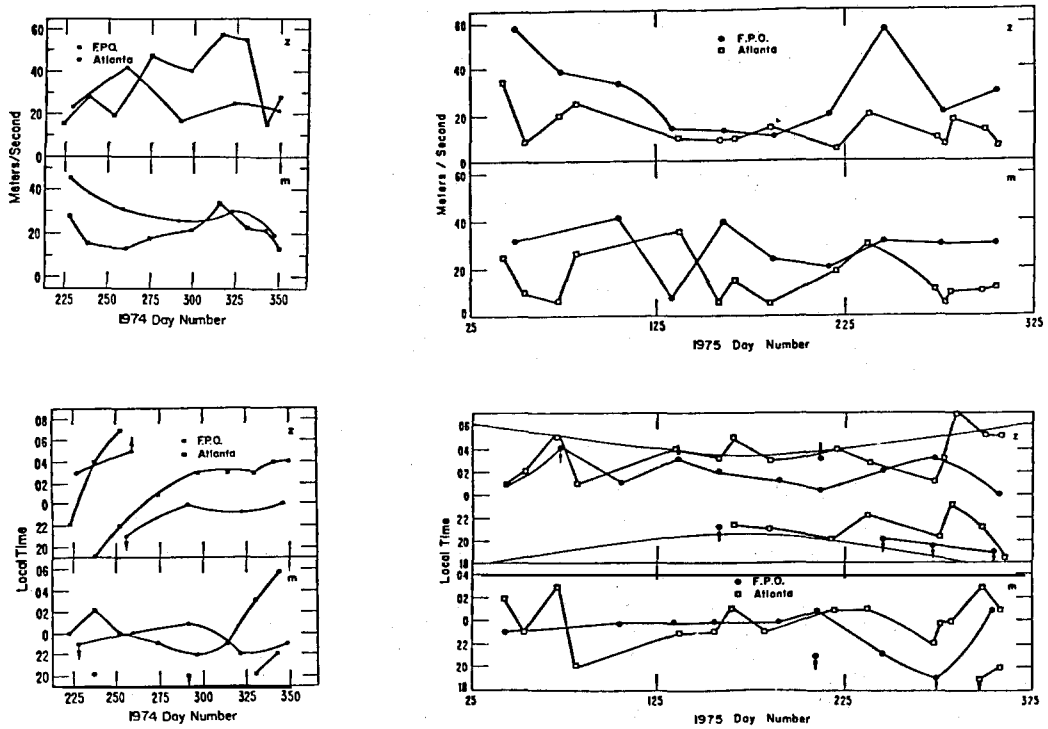

FIGURE 53. 'Amplitudes' and 'phase' of the winds for two midlatitude stations during 1974 and 1975. From reference [175].

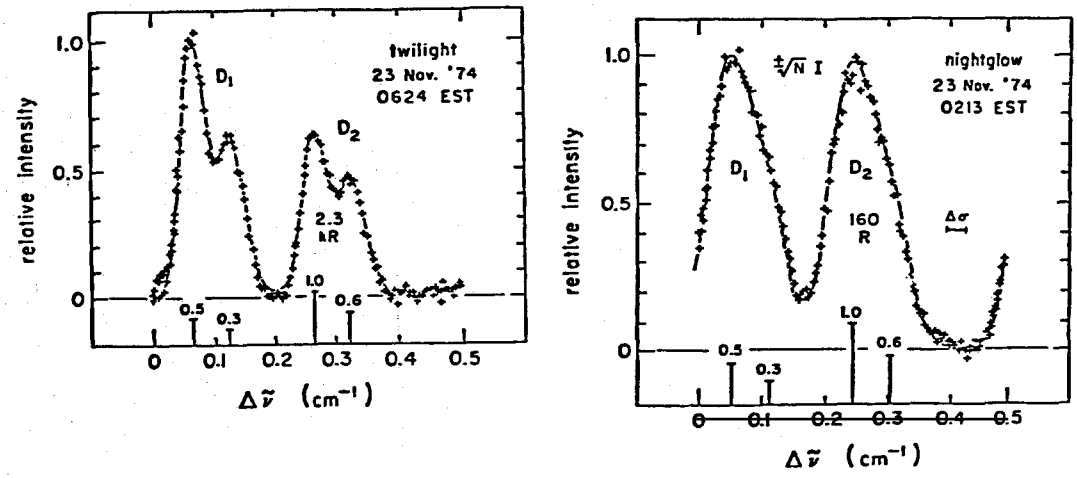

FIGURE 54. Sodium spectra measured at high resolution at twilight (left) and night (right). Note the line broadening in the night measurement with the consequent loss of the hyperfine structure. From reference [187].

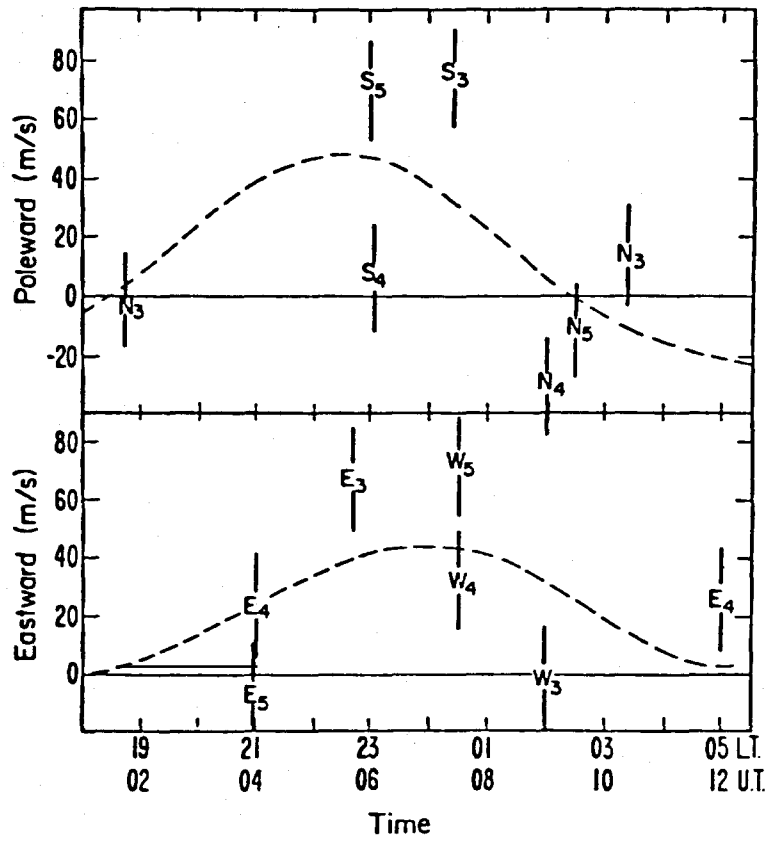

FIGURE 55. Mesospheric winds determined from the optical Doppler shift of the OH molecule, (8-3) band. From reference [189].

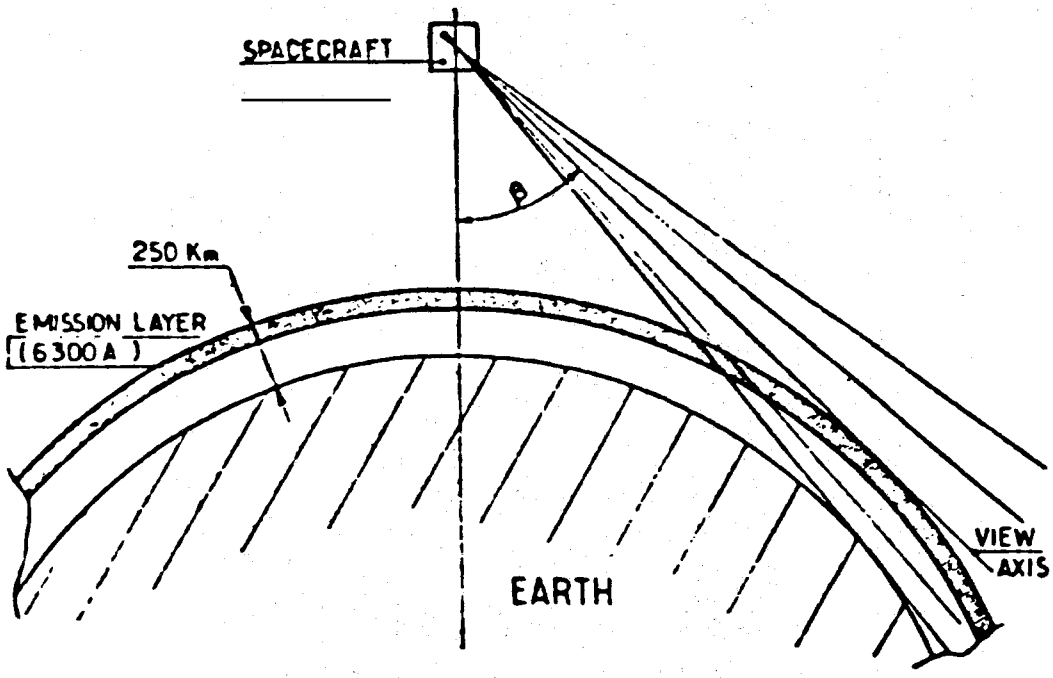

FIGURE 56. 15867K (630. nm) emission layer observation from the FPS on OGO-6. The satellite was in an 82° inclination orbit, with perigee at 400 km, and apogee at 1100 km. From reference [65].

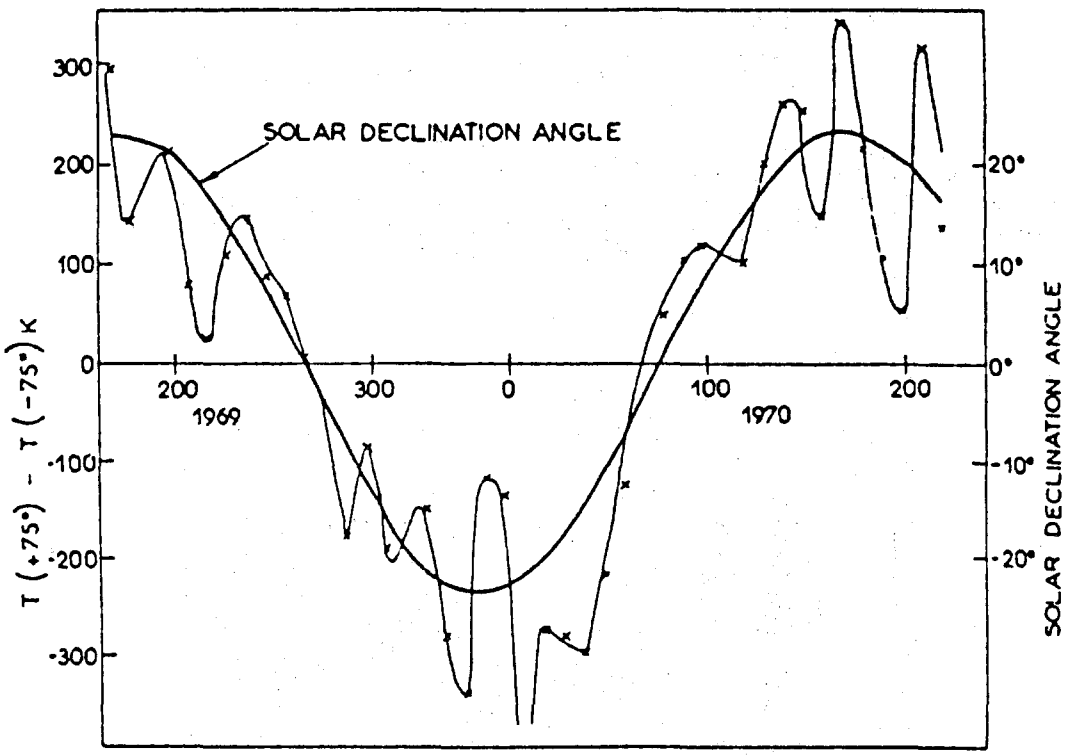

FIGURE 57. Difference between measured temperature at +75° and -75° latitude from the FPS instrument on OGO-6 plotted as a function of season. Note the rapid change in sign near the equinoxes. From reference [191].

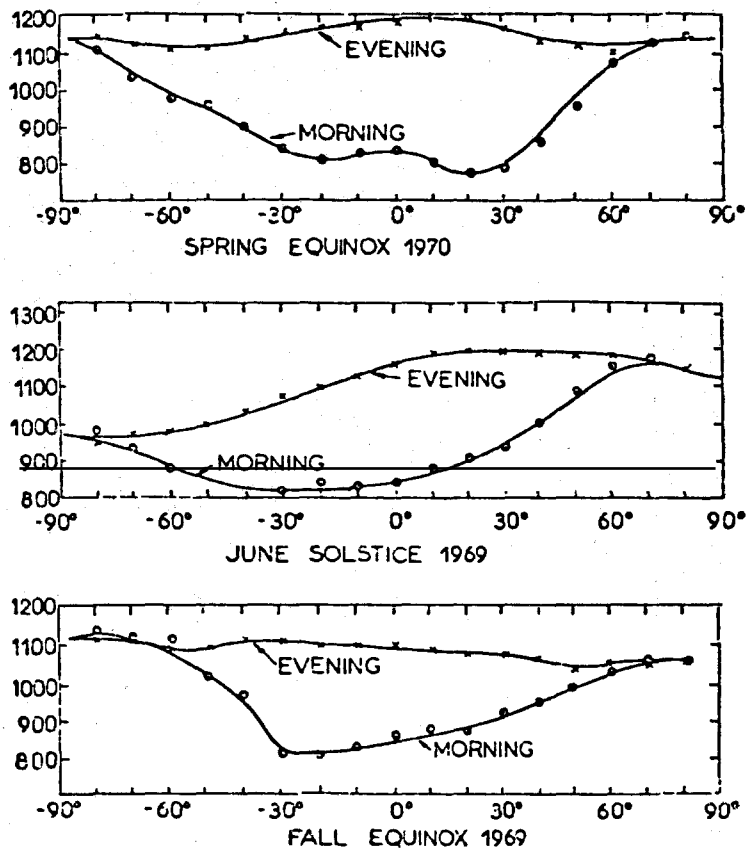

FIGURE 58. Temperatures measured at dawn and dusk plotted as a function of latitude for different seasons. The measurements are from the FPS on OGO-6. From reference [191].

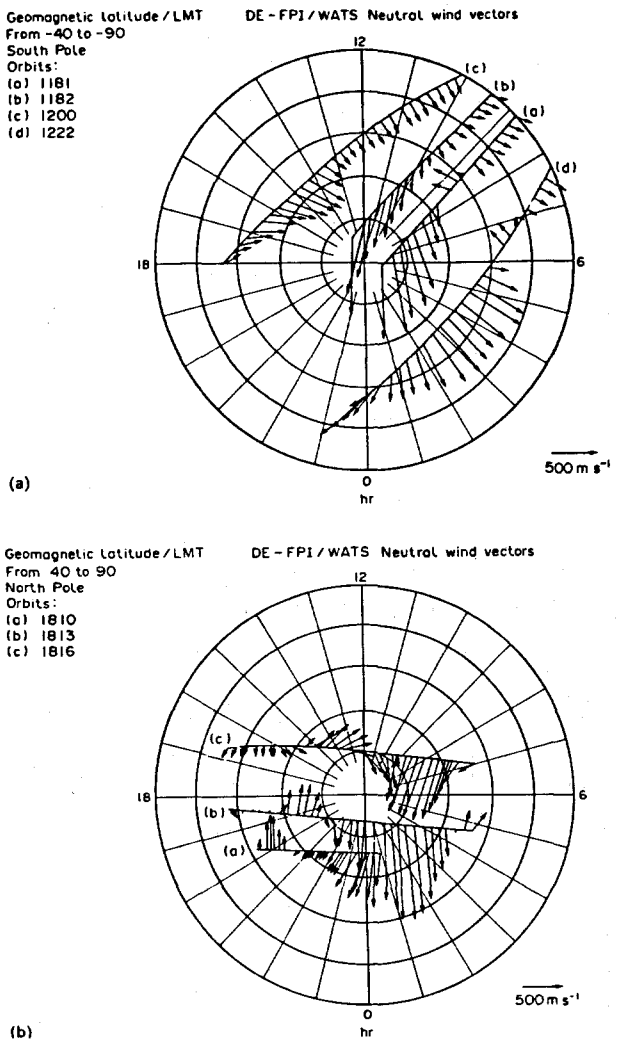

FIGURE 59. Thermospheric neutral wind vectors as measured from Dynamics Explorer 2 using the FPI and WATS instruments. The vector winds are plotted in geomagnetic polar coordinates (magnetic latitude and magnetic local time) according to scale at lower right. (a) Southern hemisphere (summer) orbits. (b) Northern hemisphere (winter) orbits. From reference [203].

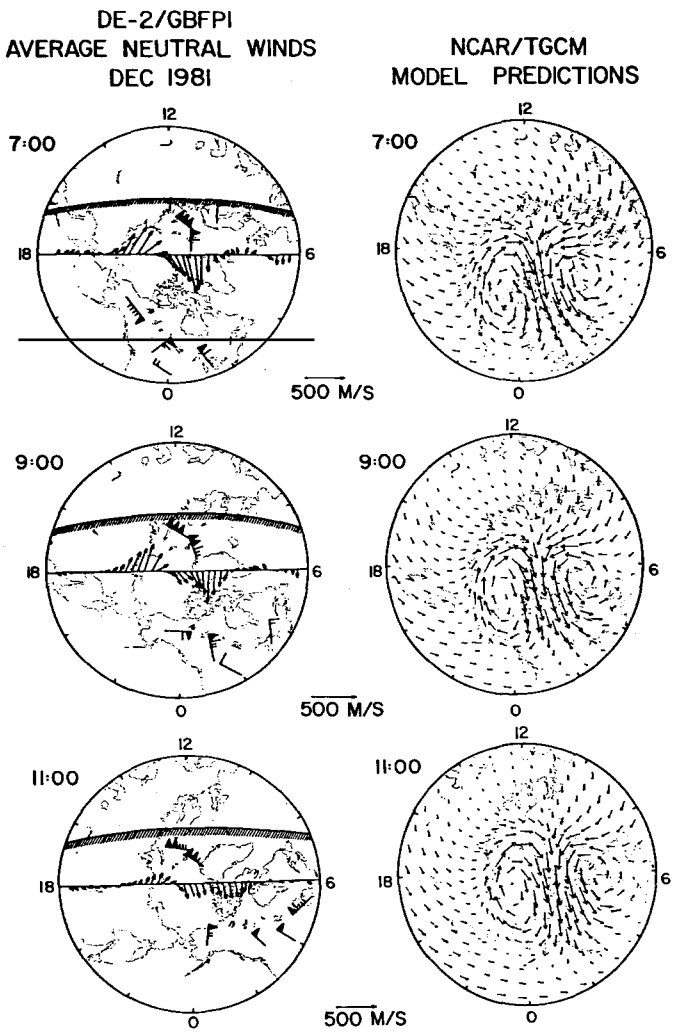

FIGURE 60. Thermospheric climatological maps. Averaged neutral wind data from Dynamics Explorer and several ground-based Fabry-Perot stations are plotted (left) for data taken in December, 1981 for the indicated Universal Times. The averaged data are compared with the predictions of the NCAR-TGCM calculations (right). From reference [206].

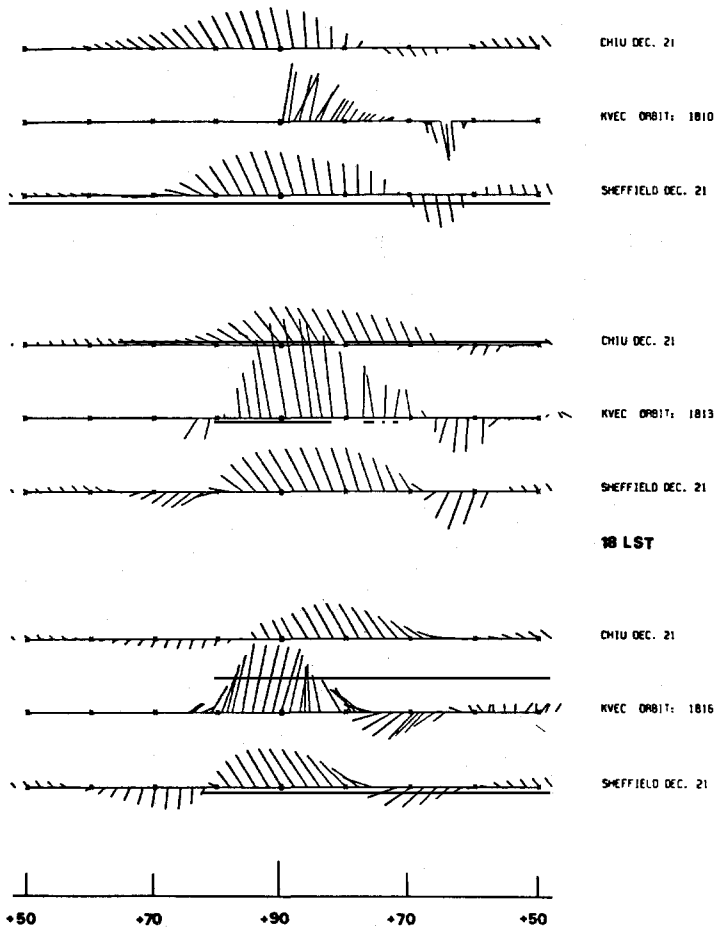

FIGURE 61. Comparison of neutral winds over the Northern hemisphere polar region with the calculations of the UCL-TGCM. Data from three orbits are compared with predictions from two runs of the model for differing input conditions. From reference [207].

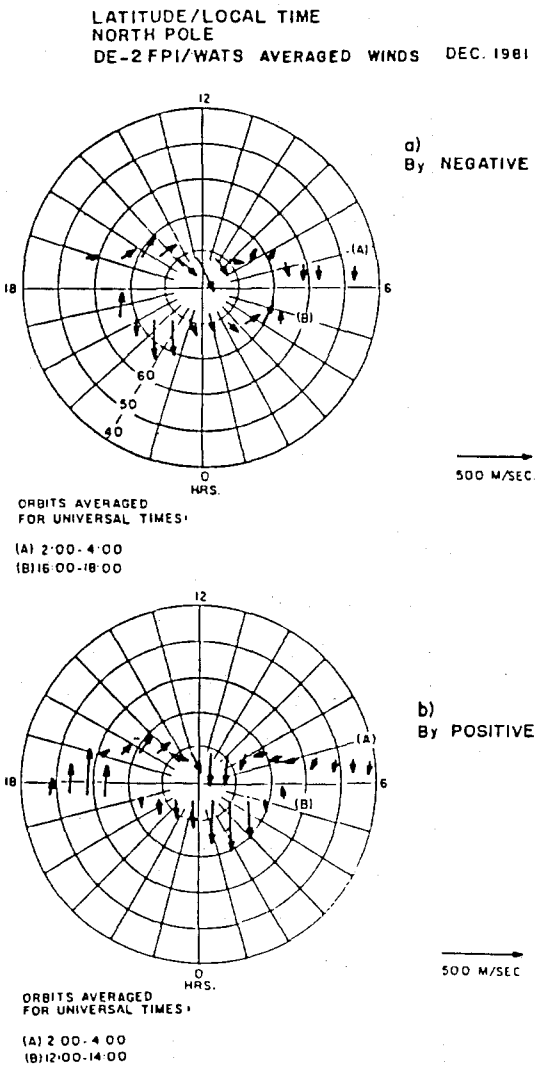

FIGURE 62. Averaged vector neutral winds from Dynamics Explorer are plotted in geomagnetic polar coordinates for (a) IMF B_y negative conditions and (b) IMF B_Y positive conditions. The data is from the northern hemisphere polar region. From reference [88].